CHAPTER 3

Synthesis, Characterisation and Application of Lab Bench Scale Prepared Chemically Modified Low–Cost Adsorbents for Removal of Fluoride from Groundwater by Batch Operation Technology

3.1. Introduction

Metal oxides Nanocomposites (NC), owing to their diversified structural, geometrical configuration and electronic modification are prominently dominate in the field of nanotechnology. Inimitable physical and chemical properties of oxide nanoparticles are mainly based on their little size and a high density of corner or edge surface sites. Particle size of any metal oxides plays a crucial role in determining their chemical and physical exigencies. Single metal oxide possesses various oxygen-containing and hydrophilic groups and, henceforth exhibits strong adsorption efficiency rather than traditional adsorbents. Such adsorption efficacy can be enhanced more exclusively by calculative incorporation of metal nanoparticles such as aluminium (Biswas *et al*., 2010), cerium (Tang and Zhang, 2016), zirconium (Ghosh *et al*., 2014), silver (Azari *et al*., 2015), tin (Biswas *et al*., 2009), lanthanum (P. Chen *et al*., 2016), magnesium (Gao *et al*., 2014), manganese (Deng *et al*., 2011) etc. into the lattice structure of each other. Utilising these unique properties of mixed metal oxides NCs and their pollutant scavenging properties, various forms of metal oxides and their composites are being increasingly explored by scientists to upgrade their adsorption efficiency. In last few decades, strong emphasis has been given to various bimetallic or polymetallic NCs, as cost effective adsorbent and extensively prepared and examined in a wide array at lab based conditions to establish their efficacy to act as a fluoride scavenging media. It is experimentally established that multivalent cations in different form of bi-metallic (Azari *et al*., 2015; Barathi *et al*., 2013; Biswas *et al*., 2009; L. Chen *et al*., 2016a, 2016b; Deng *et al*., 2011; Ghosh *et al*., 2014; Mukhopadhyay *et al*., 2017; Tang and Zhang, 2016; Tomar *et al*., 2013; Zhao *et al*., 2012) or polymetallic oxides (Biswas *et al.*, 2010; Zhao *et al.*, 2012) are used as water purification media by utilising their adsorption potentiality. Adsorption performance of metal oxide nanoaggregates is highly dependable on the porous structure and presence of hydroxyl groups in their structure (Ghosh *et al.*, 2014). To make the composite more cost effective, in most of the reported nanoaggregates iron is selected as base material (Biswas *et al.*, 2010, 2009; Zhao *et al.*, 2012). Natural abundance on earth crust and natural pollution scavenging property of iron raises its acceptance as base element. Metals such as zirconium, cerium, aluminium, tin, lanthanum, magnesium, manganese are experimentally proven to possess strong affinity to form chemical linkage with fluoride (P. Chen *et al.*, 2016; Deng *et al.*, 2011; Ghosh *et al.*, 2014; Liu *et al.*, 2010). Integration of these metals into iron accentuates the adsorption efficiency and makes these NCs a promising medium for defluoridation. Characterisation of NCs is an important aspect and plays significant role in determining the mode of application of NCs in defluoridation.

Again, improvement of adsorption capacity of these mixed metal oxides by surface modification has also brought about promising output and now most of the global research is swinging towards the deploying surface amended materials and their diversified application, particularly in water purification. In this context, Carbon, a versatile adsorbent and its various forms and their composites, is being increasingly explored by scientists worldwide to upgrade them as surface modifier to enhance adsorption efficiency. As well as if recycling and scope of reuse of these adsorbents can be possible then cost of water treatment declined significantly. In this research work, the synthesis and systematic characterization of crystalline nanoaggregates of [Fe(III)–Ce(IV)] oxides named as CIHFO carried to determine the fluoride ions removal behaviour from aqueous solutions and drinking water. Structural modification of CIHFO with graphene oxide (GO-CIHFO) and β–Cyclodextrin (βC-CIHFO) has been done also with a goal to further enhancement of fluoride adsorption capacity of CIHFO.

3.2. Characterisation of Lab Bench Scale Prepared CIHFO, GO-CIHFO and βC-CIHFO

3.2.1. FTIR Analysis

The FTIR spectra of hydrous iron (III) oxide (HFO), hydrous cerium (IV) oxide (HCO) and optimised CIHFO has been shown in Fig. 3.1A for the assessment of structural composition of all three NCs. The stretching and the bending modes of vibrations for the O-H bond has been observed by the band at wavenumber (ν) 3000-3500 cm^{-1} and ~1630 cm^{-1} respectively (Liu *et al*., 2010; Tomar *et al*., 2013). In addition, the bands recognised in the spectra at $\nu = 1300$ to 1400 cm^{-1} are depicted as the stretching modes of M-O bond and those are around 750 cm^{-1} for the bending modes of M-O bond (Sujana and Anand, 2010). The FTIR spectrum for HFO exhibited a band for Fe-O at $\nu = 1318$ cm^{-1} and for HCO at $\nu = 1396$ cm^{-1}, while in case of CIHFO multiple bands structure at $\nu = 1318$ and 1396 cm^{-1} was observed which confirm the presence of Fe-O-Ce bond in the proposed adsorbent. FTIR spectrum of adsorbent CIHFO after fluoride adsorption (Fig. 3.1B) has been signified that peak intensity has been modified after fluoride adsorption over CIHFO ensured that interaction of fluoride ions with surface hydroxyl groups of the CIHFO.

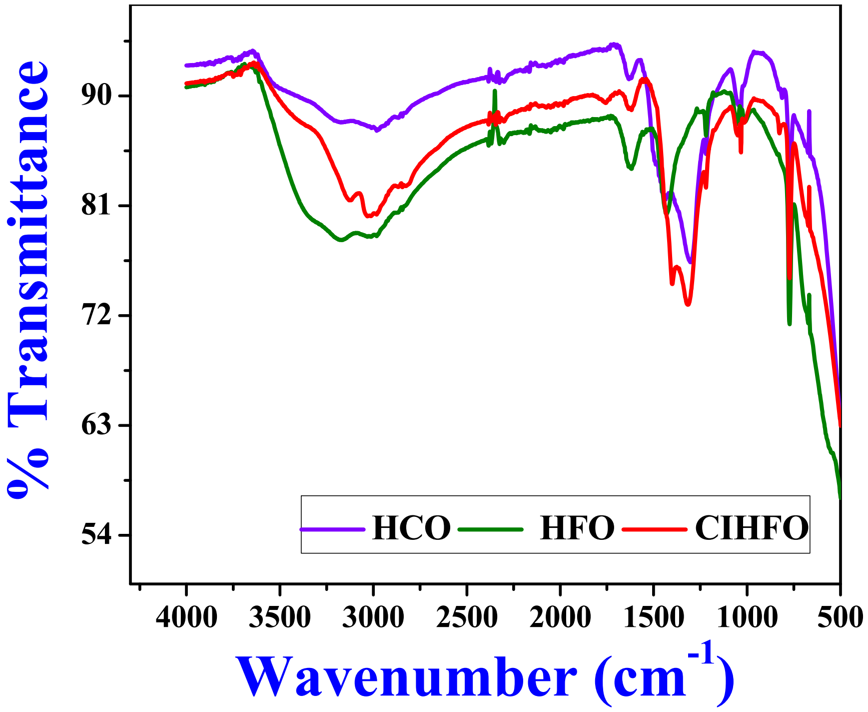

Fig. 3.1(A): Plots of FTIR spectra of pure HCO, HFO and CIHFO.

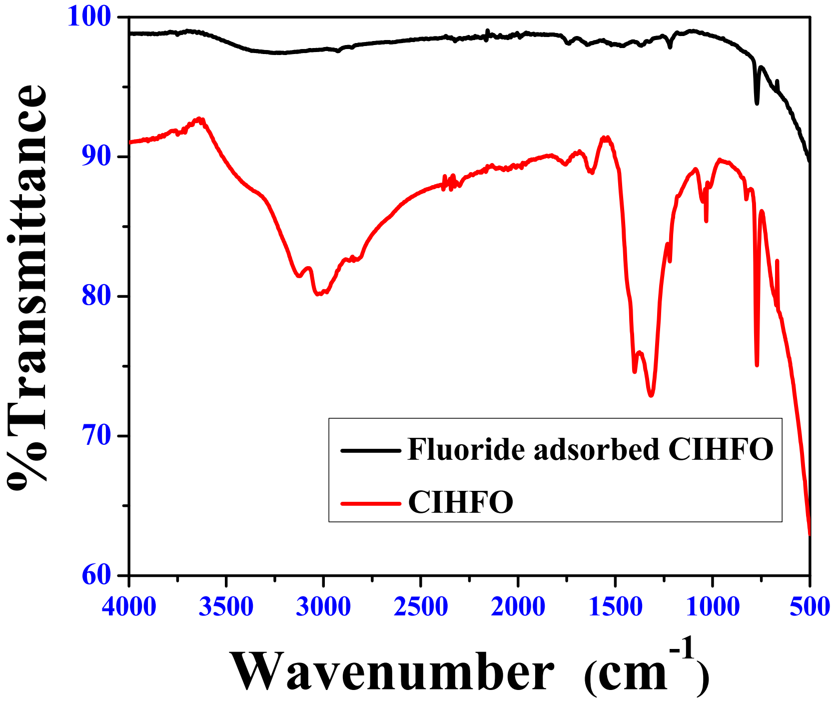

Fig. 3.1(B): Plots of FTIR spectra pure and fluoride adsorbed CIHFO

The FTIR spectra of prepared GO and GO-CIHFO shown in Fig. 3.2A and Fig.3.2B respectively, the spectral details of fluoride adsorbed GO-CIHFO has been recorded in Fig.3.3. The stretching and the bending modes of vibrations for the O-H bond had been designated by the band at wavenumber (ν) 3000-3500 cm^{-1} and ~1600-1650 cm^{-1}, respectively. The peaks observed at 3417.13 cm^{-1} and 1384.79 cm^{-1} described decisive association of C-OH into the matrix of graphite during oxidation. Adsorption bands of 2923.88 cm^{-1} and 2857.03 cm^{-1} symbolises to ν_{sym} and ν_{asym} stretching vibration mode of CH$_2$ (Barathi *et al*., 2014). In FTIR spectrum of GO (Fig.3.2A), the bands at wavenumber 1751 cm^{-1} and 1729 cm^{-1} are the stretching bands for C=O (monomer H bonded) and C=O (dimer H bonded).

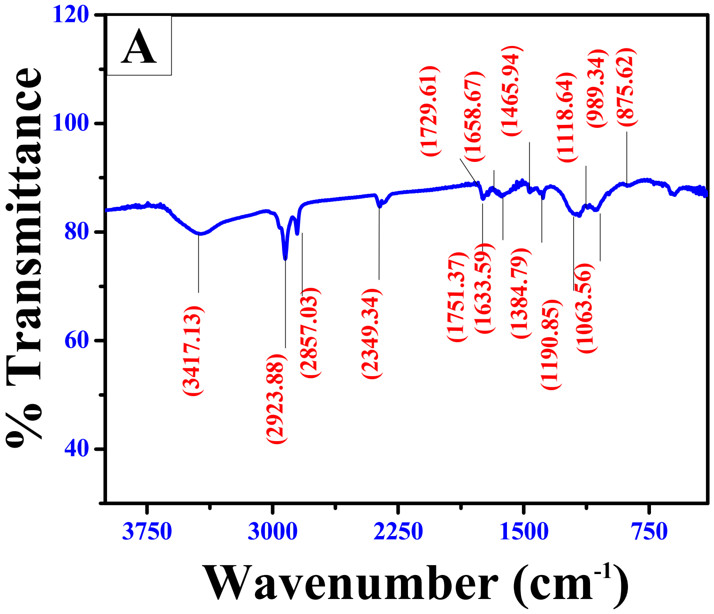

Fig. 3.2(A): Plots of FTIR spectra of Graphene Oxide (GO).

The band peaks at 1190 cm^{-1}, 1063 cm^{-1} are due to presence of epoxy C-O and alkoxy C-O stretching vibration present in prepared GO confirmed the formation of graphene oxide (GO). After incorporation of GO into CIHFO, the band at 3417.13 cm^{-1} shifted to 3380.46 cm^{-1} and broadened up ensuring the interaction of metal ions with hydroxyl group of GO and further surface enhancement of CIHFO. Characteristic band observed at 414.67 cm^{-1} and 983.63 cm^{-1} can be attributed to Fe-O and Ce-O bonds. Significant modification of peak intensity has been observed after fluoride adsorption. Shifting of bands from 3417.13 cm^{-1} to 3243.04 cm^{-1} and from 1633.59 cm^{-1} to 1625.88 cm^{-1} attributed with interaction of fluoride ions with surface hydroxyl groups of the adsorbent.

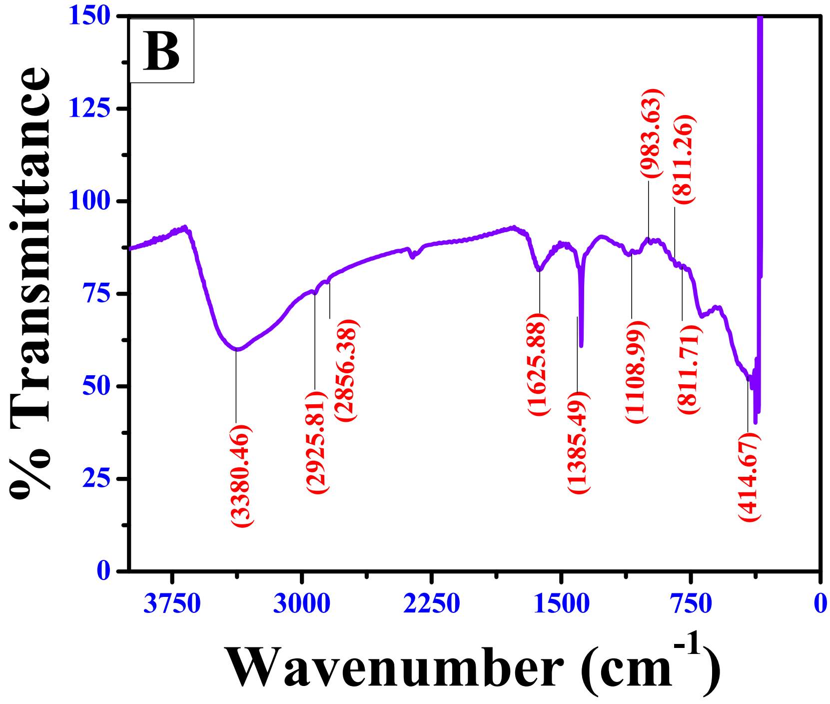

Fig. 3.2(B): Plots of FTIR spectra of GO-CIHFO

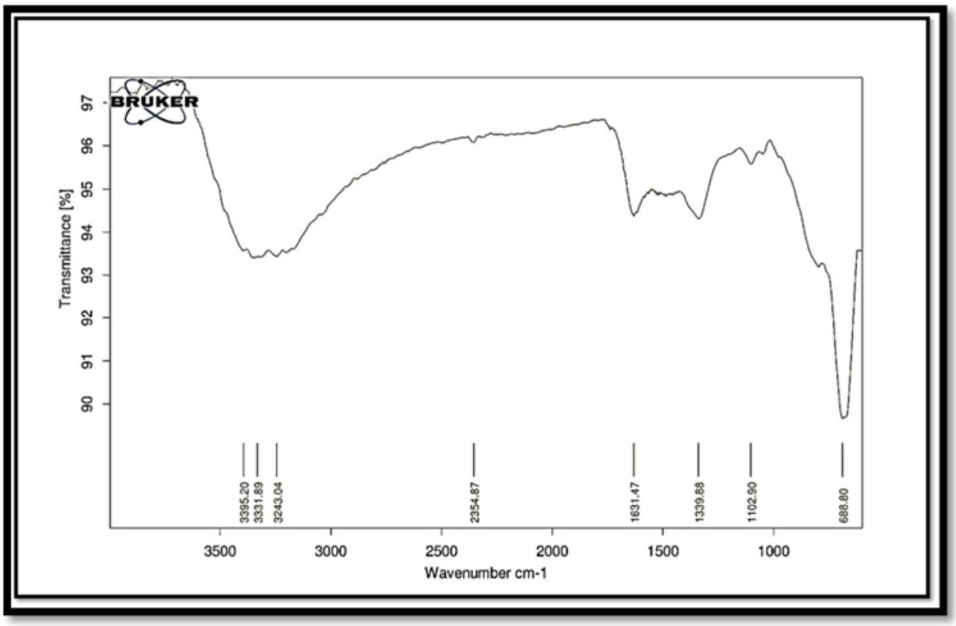

Fig. 3.3: Plots of FTIR spectra of fluoride adsorbed GO-CIHFO

The FTIR spectra of β-CD amended CIHFO (βC-CIHFO) has been shown in Fig.3.4. The FTIR bands at 3300 to 3200 cm^{-1}, and ~1550-1630 cm^{-1}, separately might be assigned for the –OH stretching and bending bond of vibration, respectively. The bands recorded in the spectra at ν = 1300 to 1400 cm^{-1} are the stretching modes of M-O bond and those are around 670 to 830 cm^{-1} for the bending modes of M-O bond. When Fe–Ce binary oxide forms an inclusion complex with β-CD, a different FTIR spectrum is resulted. In this FTIR spectrum–OH stretching and bending mode vibration occurred at 3269.39 cm^{-1} and 1608.90 cm^{-1}. Other characteristic band at 1150.56, 2928.39, 1023.88 cm^{-1} are representing to C–C,–CH_2 and C–OH of β-CD, collectively. Occurrence of multiple band structure at ν = 1323.10 and 1410.01 cm^{-1} which confirm the presence of Fe-O-Ce bond within βC-CIHFO ensure successful encapsulation with β-CD. Significant changes in peak intensity observed after fluoride adsorption confirmed interaction of fluoride ions with surface active sites of βC-CIHFO (Fig.3.5).

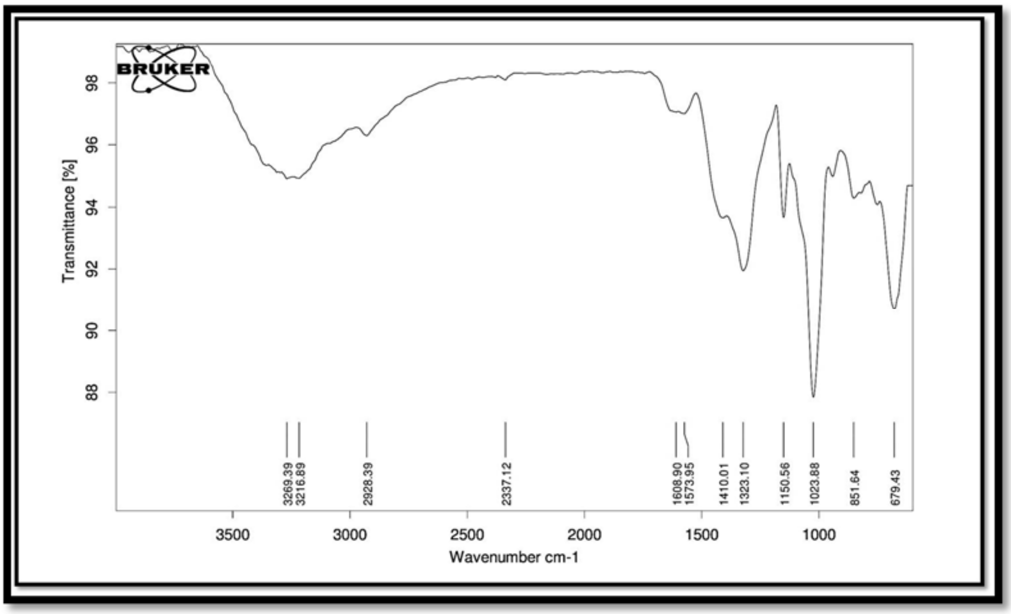

Fig. 3.4: Plots of FTIR spectra of βC-CIHFO before fluoride adsorption

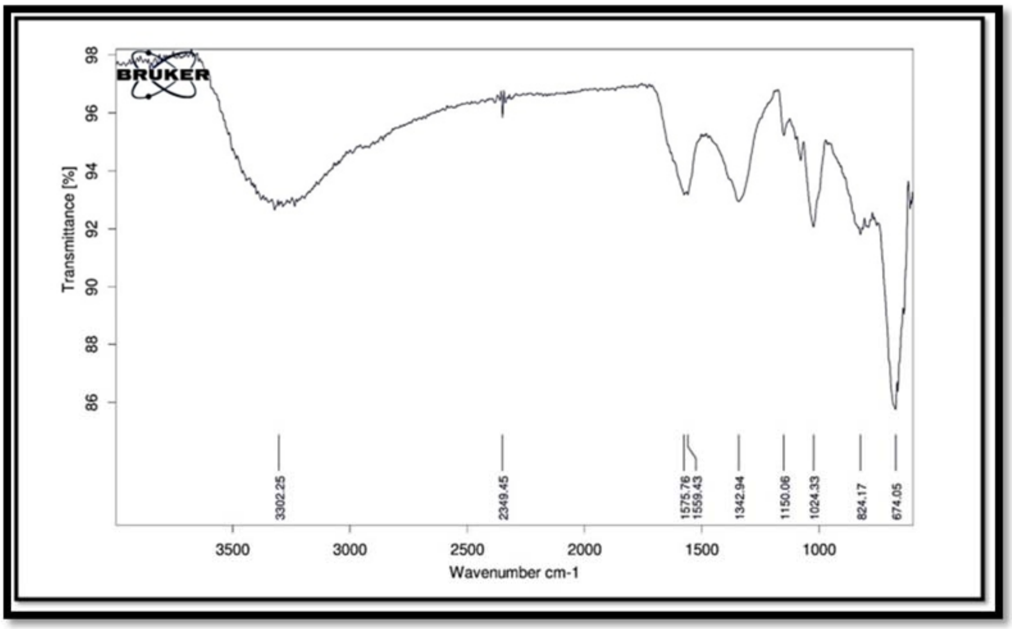

Fig. 3.5: Plots of FTIR of fluoride adsorbed βC-CIHFO

3.2.2. XRD Pattern Analysis

The powder XRD pattern (Fig.3.6) of the CIHFO (Fe: Ce = 1.0: 0.5) sample shows the presence of microcrystalline particles and crystallites ~5 nm in size. The 2θ (°) values for the XRD peak positions of the newly developed CIHFO has been shown similarities with reported(Basu and Ghosh, 2013) results of Fe_2O_3 and CeO_2 [23.03°, 28.91°, 32.78°, 48.29°,57.11° for CIHFO; 24.21°(0 1 2), 33.25° (1 0 4), 35.72°(1 1 0),40.97° (1 1 3), 49.6° (0 2 4), 54.22°(1 1 6), 57.78°(1 2 2/0 1 8), 62.61°(2 1 4), 64.17° (3 0 0), 72.18° (1 1 9), 75.67°(2 2 0) for Fe_2O_3 and 33.0° (2 0 0), 56.3° (3 1 1), 69.43° (4 0 0), 76.69° (3 3 1), 79.04°(4 2 0) for CeO_2]. Two peaks of CIHFO very closely matched those of CeO_2 phase with cubic structures corresponding to (h k l) values of (1 1 1) and (2 2 0), while one peak was common to Ce_2O_3 phase with a hexagonal structure corresponding to the (h k l) value (2 0 1). However, only one XRD peak of CIHFO was found to be close to a-Fe_2O_3; this clearly indicates the incorporation of Fe^{3+} ion into the crystal structure of CeO_2.

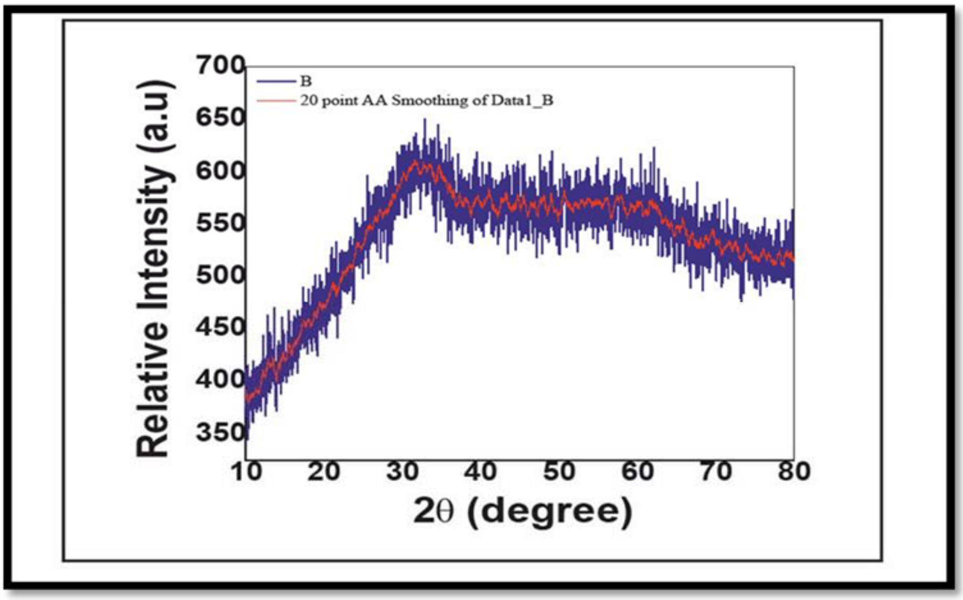

Fig. 3.6: Plots of powder X-ray diffraction patterns of CIHFO

The XRF analysis for composition of the sample was quantified the presence of 55.082 % Fe_2O_3 and 33.626 % CeO_2 with some other minor constituents as impurities namely Al_2O_3 (0.059 %), SiO_2 (0.456 %), CaO (0.014 %), MnO (0.395 %), and Cl^- (6.97 %). The empirical formula of the hybrid oxide established is $Fe_{3.72}CeO_{7.59}$.

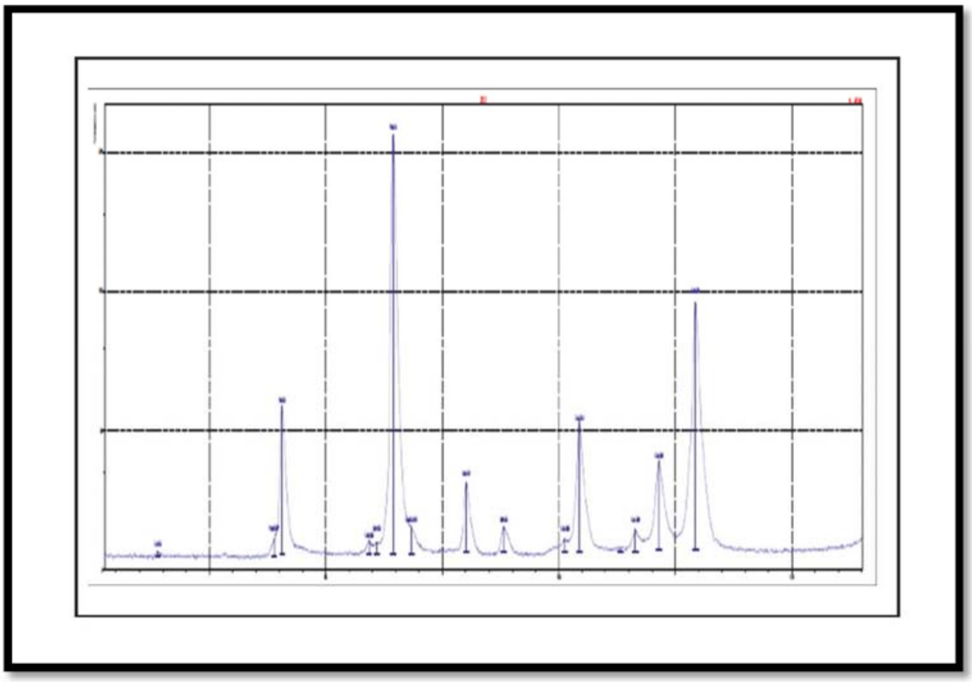

Fig. 3.7: X-ray fluorescence pattern of CIHFO for the composition.

Dramatic changes in crystalline phases and in crystallite size have been observed with incorporation of one material to another material. In present research work, later, surface of pristine CIHFO has been modified with graphene Oxide (GO) and beta-Cyclodextrin (β-CD) with a goal to change amorphous structure of CIHFO to crystalline as well as enhancement in fluoride adsorption capacity was also primly considered. XRD is the most advanced technical tool that helps to identify such changes.

Fig. 3.8A represents the XRD patterns of GO and Fig. 3.8B XRD patterns of GO-CIHFO for comparison. The diffraction peaks for graphite at 2θ=26.38° and 54.54° corresponding to the plane (002) and (004) respectively was totally diminished (Barathi *et al.*, 2014) and the most evident diffraction peak at 2θ=10.82° observed with corresponding d-spacing of 0.424 nm with a full width half maximum (FWHM) at ~ 0.82.

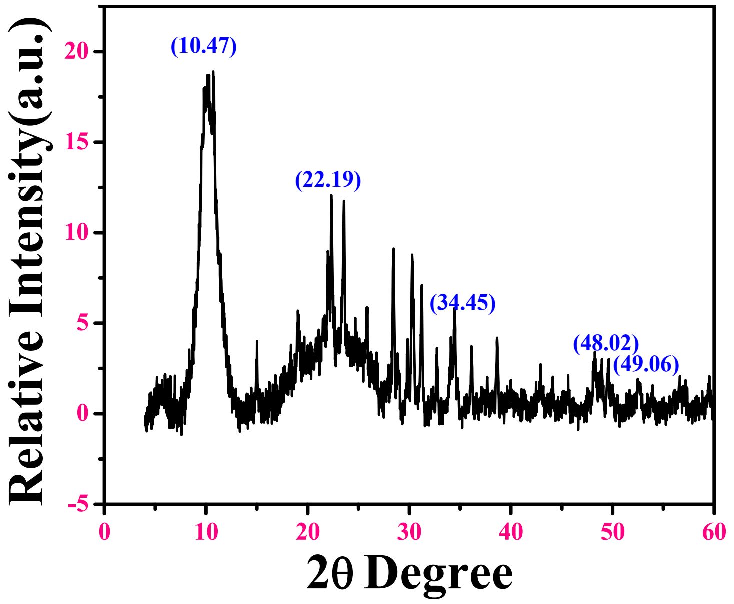

Fig. 3.8 (A): The powder X-ray diffraction patterns of GO

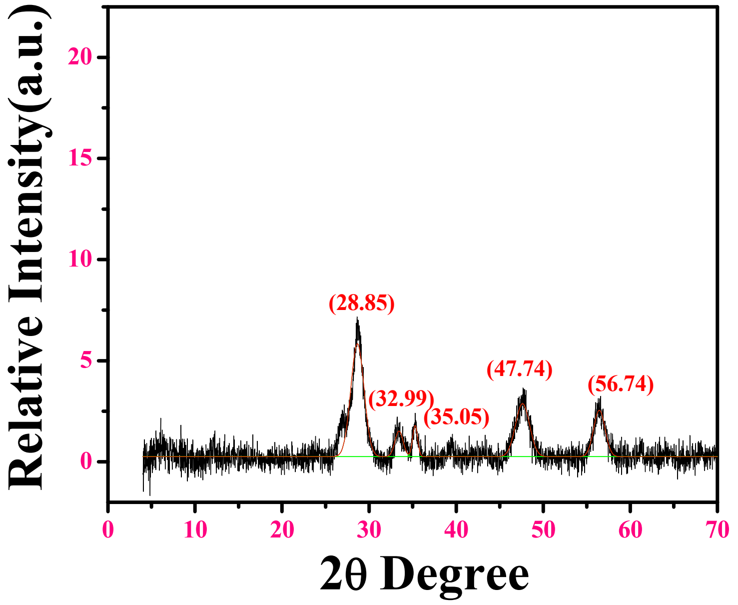

Fig. 3.8(B): The powder X-ray diffraction patterns of GO-CIHFO

The d-spacing is expanded wisely as compared to pristine graphite (0.34 nm) suggesting that graphite is fully oxidized to GO (Mohan *et al*., 2016). Disappearance of characteristic diffraction peaks associated with graphite suggest the presence of carboxyl, hydroxyl functional groups in GO during exfoliation resulted due to oxidation of graphite layers (Barathi *et al*., 2014). In prepared GO-CIHFO, the characteristic peak of GO has not been observed might be due to complete interaction of GO with CIHFO. The XRD pattern of the GO-CIHFO (Fig.3.8B) showed the presence of peaks at °2θ = 28.85, 33.25, 35.05, 47.74 and 56.74 indicating the signature of CIHFO (Mukhopadhyay *et al*., 2017). Full width half maximum (FWHM) at ~ 1.89-0.67 revealed the presence of microcrystalline particles and crystallites of ~5-10 nm in size.

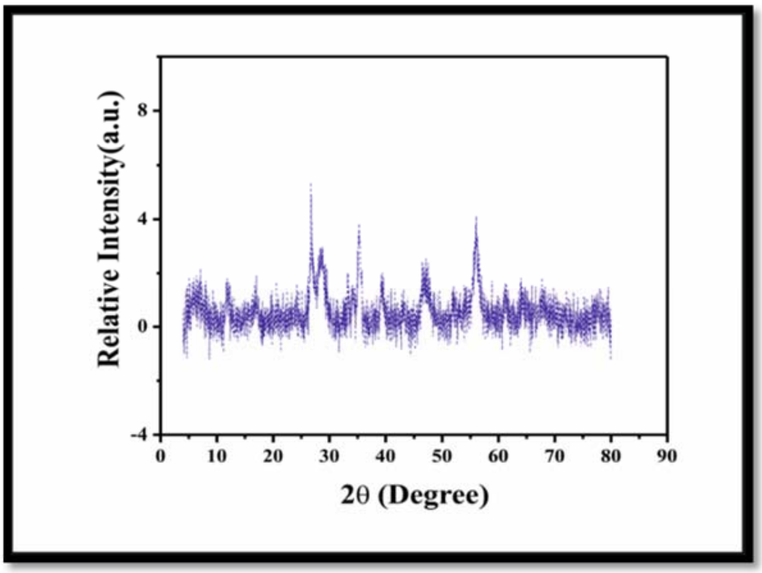

Fig. 3.9: The powder X-ray diffraction patterns of βC-CIHFO

The sharp peaks (with °2θ ~ 28.85, 33.25, 35.05, 47.74 and 56.74) (Mukhopadhyay *et al*., 2017) with relatively narrow FWHM ~ 1.67-0.91 ensure micro crystalline nature of NCs of βC-CIHFO (~5-10 nm), whereas after incorporation of β-CD there is no such change in intensity observed instead of shift of amorphous phase to crystalline phase in compare to pure mixed oxide. Occurrence of more firmly crystallinity in CIHFO can be correlated with the encapsulation of β-CD.

3.2.3. TG/DTA Analysis

TG and DT analyses are most authentic measurement to determine the thermal stability of any proposed material. The TG spectrum of the CIHFO (Fig. 3.10A) recorded a maximum weight loss at around 230ºC and the percentage of this loss is about 25. This result is found to be different from Yang *et al* (Yang *et al.*, 2016). It has also been confirmed from a sharp exothermic band in the DT spectrum (Fig.3.10B). This is presumably owing to the elimination of physically attached water molecules which includes the surface adhered hydrogen bonded and lattice water molecules.

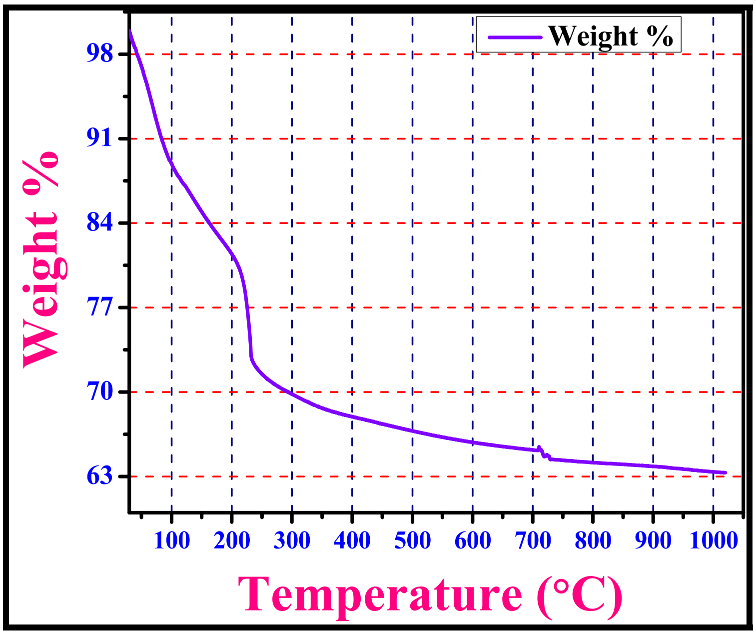

Fig. 3.10(A): Thermogravimetric (TG) analysis of CIHFO.

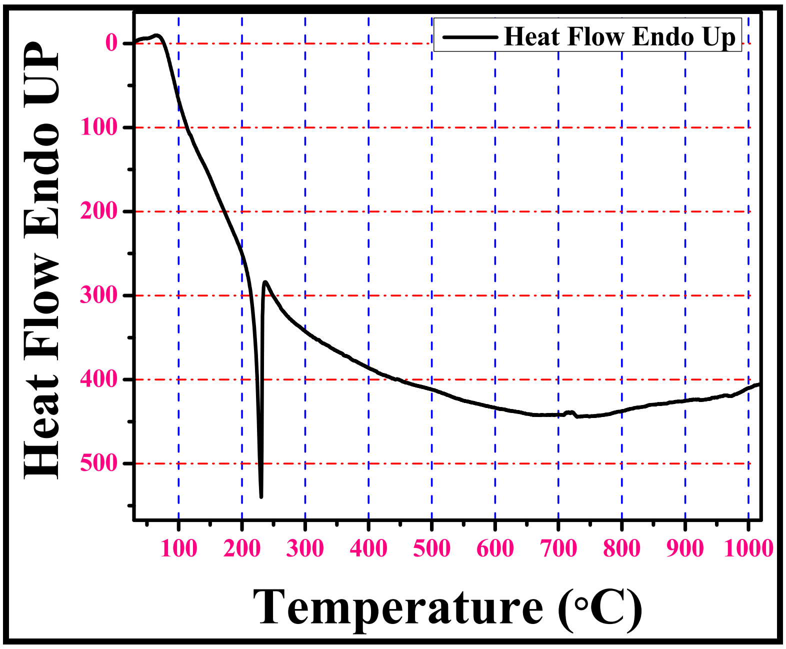

Fig. 3.10(B): Differential Thermal (DT) analysis of CIHFO.

Here the TG and DT analysis of GO-CIHFO also gave the glimpse of temperature dependent stability characteristics of the structurally modified material. The TG spectrum of GO-CIHFO shows rapid but smooth loss of mass (~35% of initial mass) up to a temperature ~ 435°C (Fig.3.11A).

This weight loss assumed to be associated with removal of surface abandoned water molecules and hydroxyl groups by dehydroxylation of GO incorporated hydrous mixed oxide NCs (Kanrar *et al.*, 2016) and removal of carbon and oxygen in form of CO from composite. A sharp endothermic peak of DTA spectrum (Fig.3.11B) is observed at 80°C ensures the loss of physically adsorbed water molecules from surface of hydrous NCs. A sharp but small exothermic peak at 260°C indicates thermal conversion of GO and a broad DTA exothermic peak at above ~350°C to ~435°C is closely associated with phase transition of the material. No occurrence of any other bands above 500°C justifies that residue of NCs is thermally stable within studied temperature range.

In TG spectrum of the βC-CIHFO (Fig. 3.12A), first weight loss recorded at around 200ºC (~30% of initial mass) and again smooth loss of mass (~20% of initial mass) up to a temperature ~ 400°C was observed. A sharp endothermic peak of DT spectrum at 200°C and a broad endothermic peak of DT 350°C (Fig.3.12B) confirms the loss of physically adsorbed water molecules from surface of hydrous NCs. Absence of any peak above 500°C of DT spectrum justify that above this temperature range synthesized NCs is thermally stable.

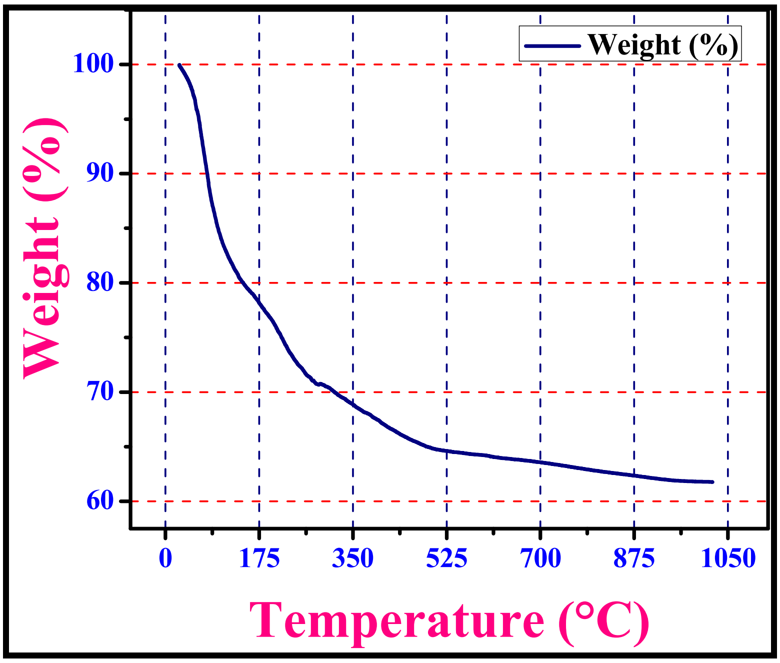

Fig. 3.11(A): Thermogravimetric (TG) analysis of GO-CIHFO

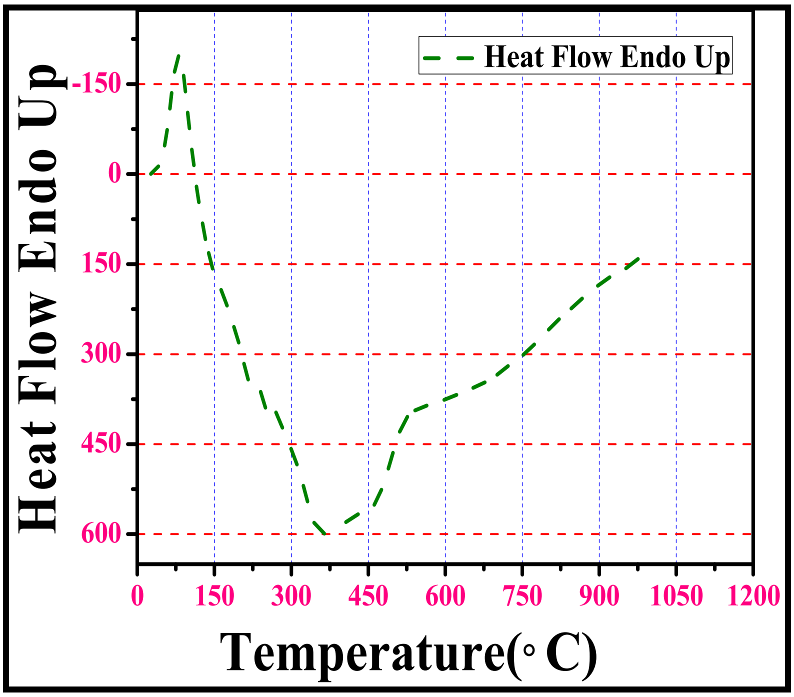

Fig. 3.11(B): Differential Thermal (DT) analysis of GO-CIHFO

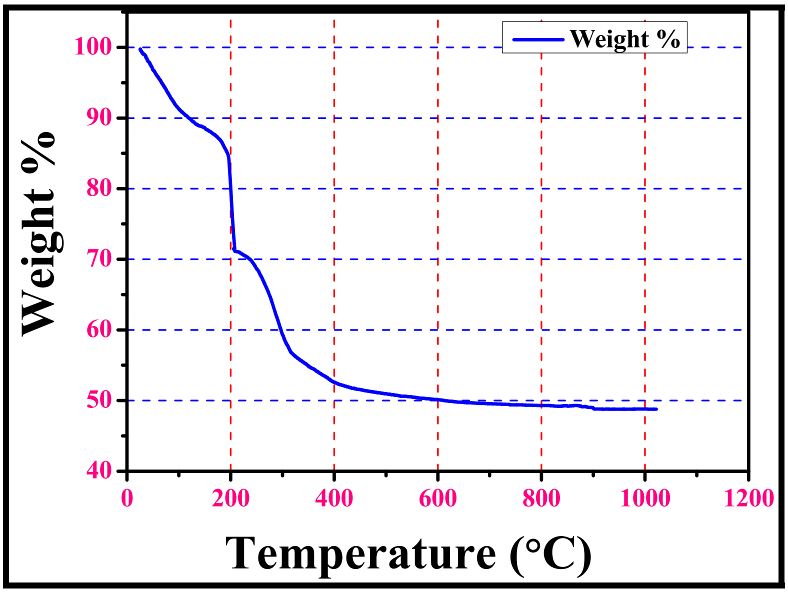

Fig. 3.12(A): Thermogravimetric (TG) analysis of βC-CIHFO

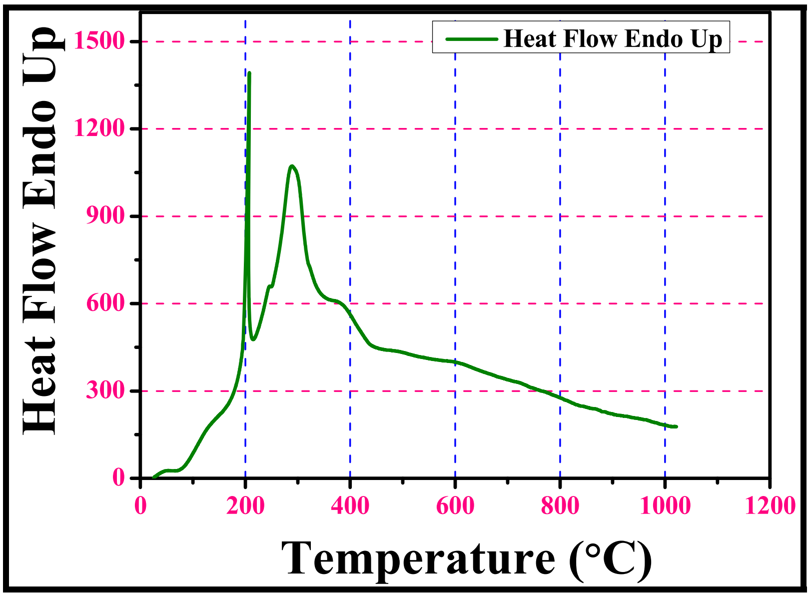

Fig. 3.12(B): Differential Thermal (DT) analysis of βC-CIHFO

3.2.4. Optical Microscope and SEM Imaging with EDX

Optical Microscopic images and SEM images of CIHFO (Fig. 3.13) exhibit the irregular surface morphology of the CIHFO. The SEM-EDX spectrum (Fig. 3.14) also supports the presence of higher iron content than cerium that endorses the preparation condition the CIHFO. From the analytical data, the empirical formula of the hybrid oxide (CIHFO) is established as $Fe_{3.72}CeO_{7.59}$.

The images of GO-CIHFO acquired from optical and scanning electron microscopic analysis (Fig.3.15) also ensure the irregular surface morphology GO-CIHFO. Irregular shaped agglomerated particles are compressed within the layers of GO and act as scaffolding surface for CIHFO.

The SEM-EDX spectrum (Fig.3.16) has also supported the presence of higher carbon and oxygen content in respect of cerium and iron metal oxide. This is fulfil our purpose to use GO as surface modifier to develop a cheaper adsorbent rather than CIHFO, the pure mixed metal oxide. From the analytical data, the empirical formula of GO incorporated mixed hybrid oxide is established as $Fe_{0.279}\,Ce_{0.198}\,C_{0.222}\,O_{3.36}$.

Fig.3.17 represents the images captured from optical and scanning electron microscopic analysis of βC-CIHFO. All these images guarantee the uneven surface morphology of βC-CIHFO. Irregular shaped agglomerated particles are encapsulated within the cavity of β-cyclodextrin by acting as an anchoring framework for CIHFO. The SEM-EDX spectrum (Fig.3.18) also established the presence of higher carbon and oxygen content in respect of cerium and iron metal oxide. This result ensures application β-CD as surface modifier to develop an inexpensive adsorbent rather than CIHFO, the pure mixed metal oxide. From the analytical data, the empirical formula of βC-CIHFO is recognised as $Fe_{0.117}\,Ce_{0.170}\,C_{0.433}\,O_{4.641}$.

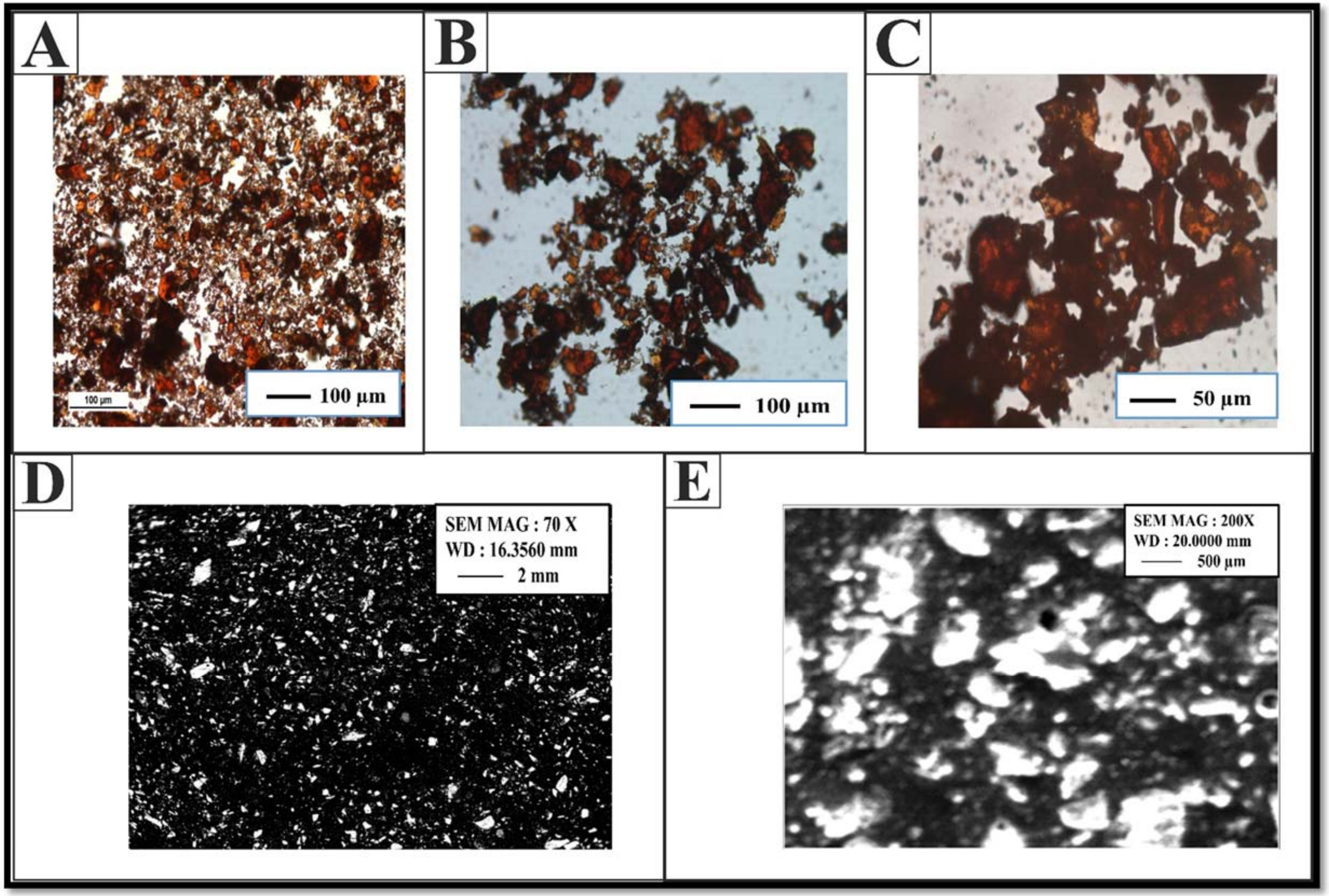

Fig. 3.13: (A-C) Optical microscopic images and **(D-E)** Scanning electron microscopic imagesof CIHFO in different magnifications.

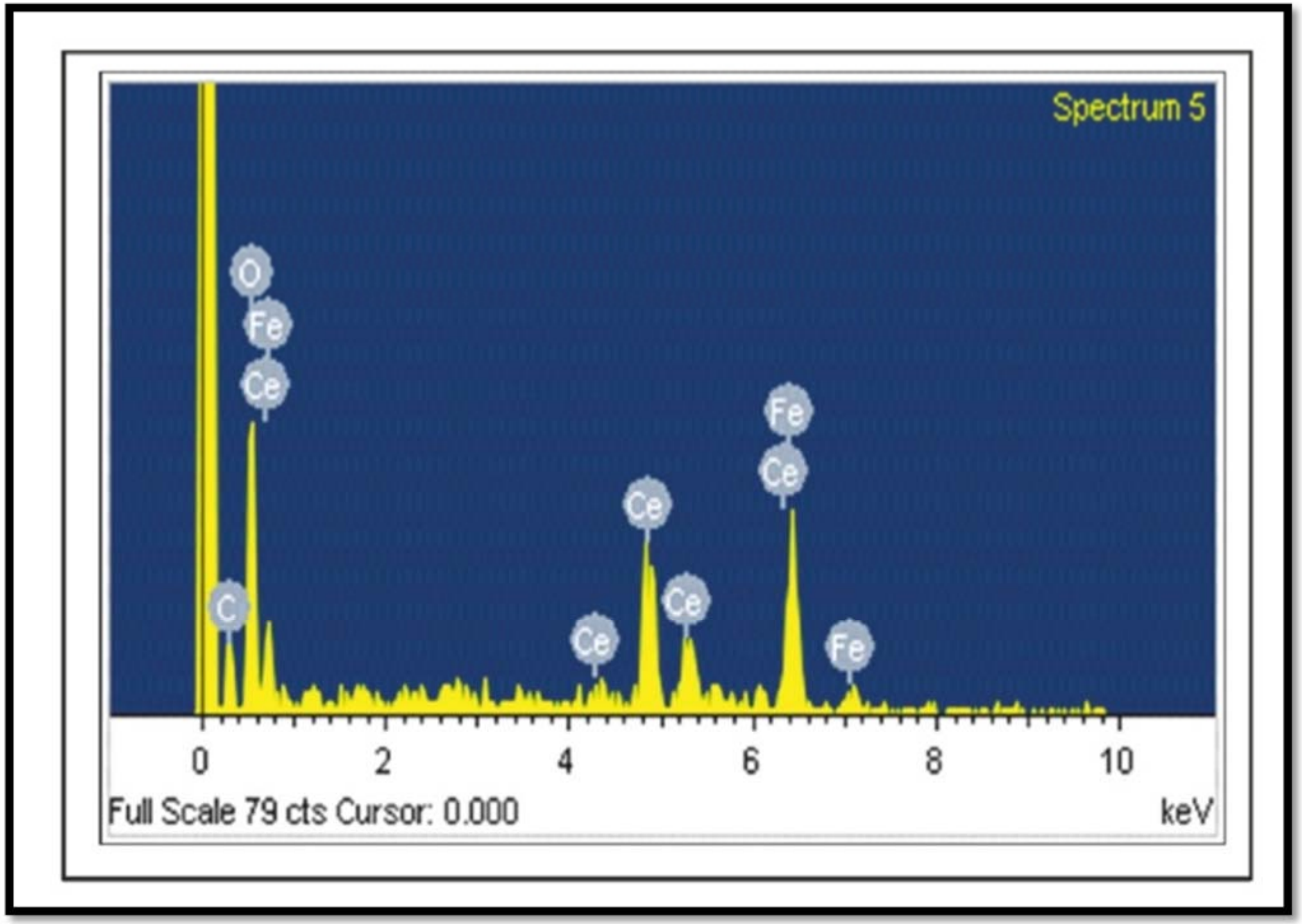

Fig. 3.14: SEM- EDX spectrum of CIHFO NCs

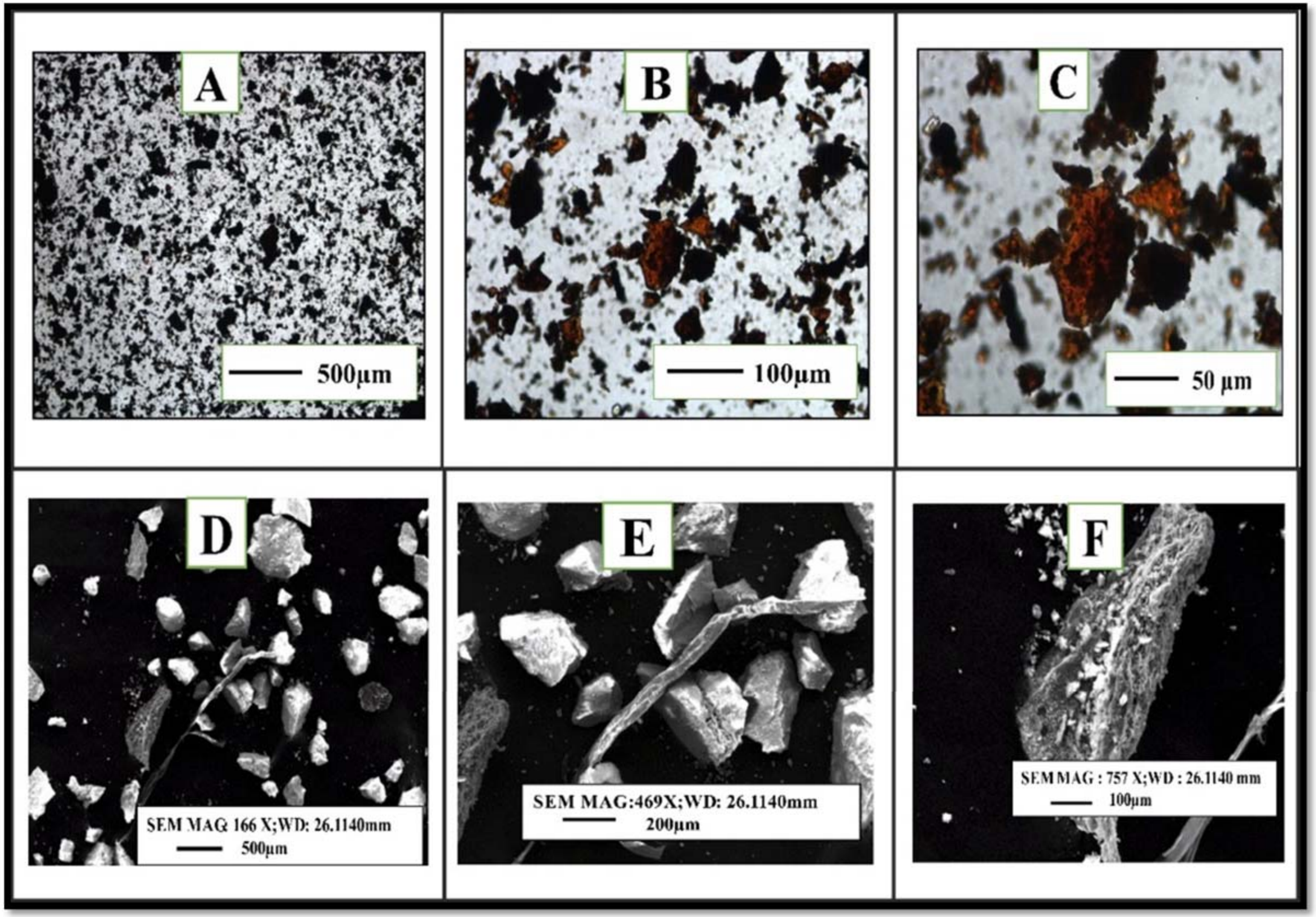

Fig. 3.15: (A-C) Optical microscopic images and **(D-F)** Scanning electron microscopic images of GO-CIHFO in different magnification

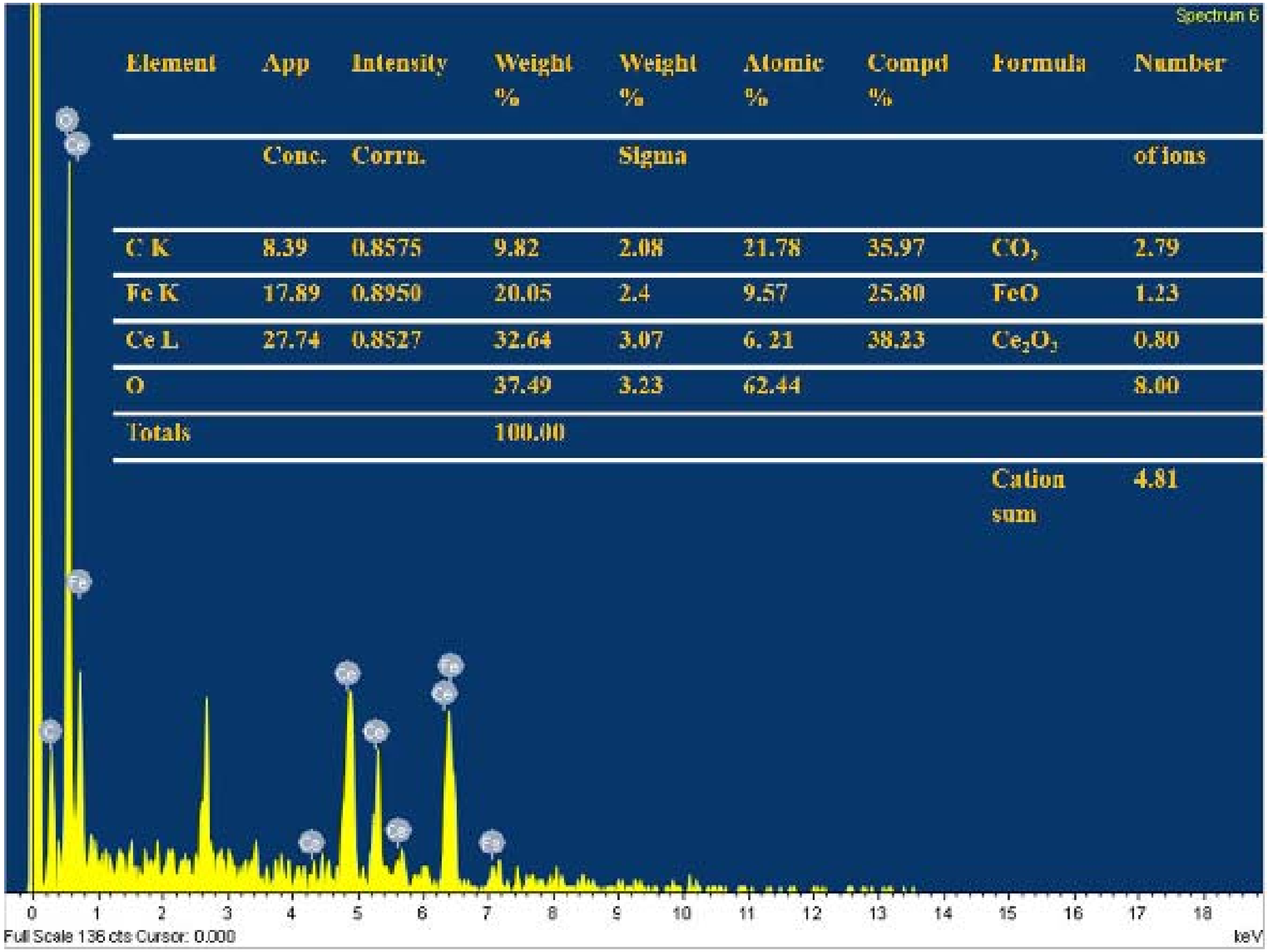

Element	App Conc.	Intensity Corrn.	Weight %	Weight % Sigma	Atomic %	Compd %	Formula	Number of ions
C K	8.39	0.8575	9.82	2.08	21.78	35.97	CO_2	2.79
Fe K	17.89	0.8950	20.05	2.4	9.57	25.80	FeO	1.23
Ce L	27.74	0.8527	32.64	3.07	6. 21	38.23	Ce_2O_3	0.80
O			37.49	3.23	62.44			8.00
Totals			100.00					
							Cation sum	4.81

Fig. 3.16: SEM-EDX spectrum of GO-CIHFO nanocomposite

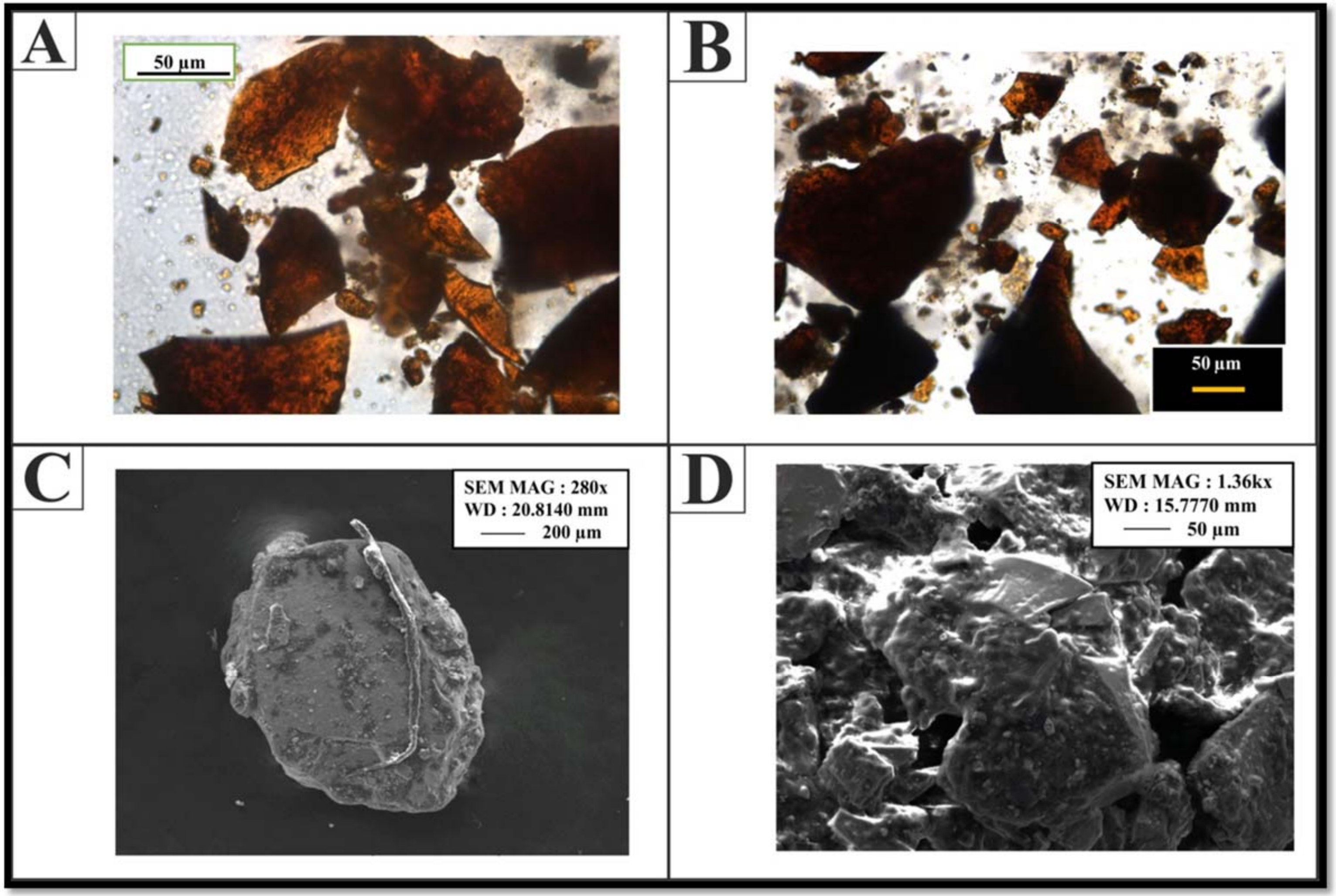

Fig.3.17: **(A-B)** Optical microscopic images and **(C-D)** Scanning electron microscopic images of βC-CIHFO in different magnification

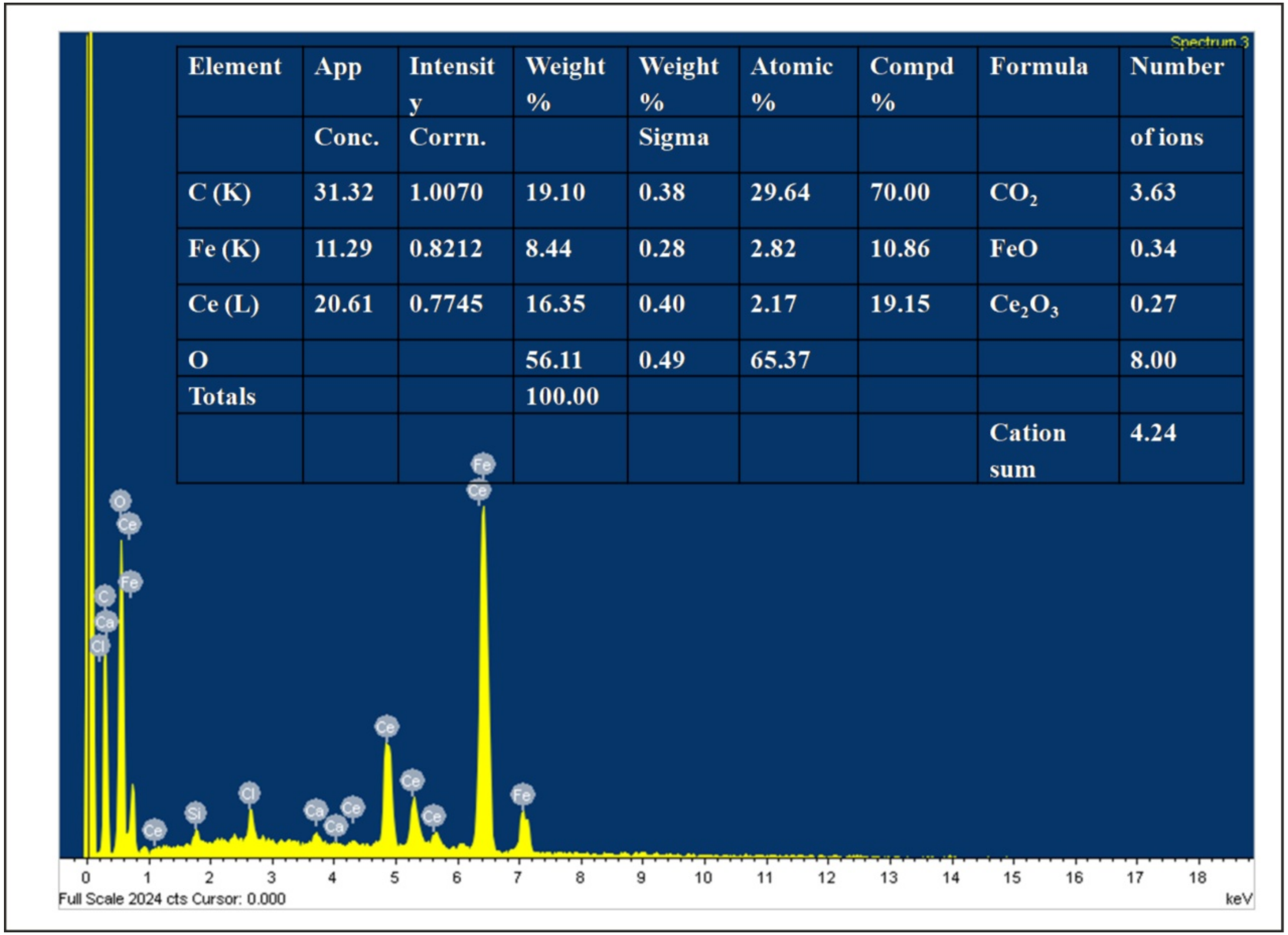

Element	App	Intensity	Weight %	Weight %	Atomic %	Compd %	Formula	Number
	Conc.	Corrn.		Sigma				of ions
C (K)	31.32	1.0070	19.10	0.38	29.64	70.00	CO_2	3.63
Fe (K)	11.29	0.8212	8.44	0.28	2.82	10.86	FeO	0.34
Ce (L)	20.61	0.7745	16.35	0.40	2.17	19.15	Ce_2O_3	0.27
O			56.11	0.49	65.37			8.00
Totals			100.00					
							Cation sum	4.24

Fig. 3.18: EDX spectrum of βC-CIHFO nanocomposite

3.2.5. TEM Imaging

The Transmission Electron Microscopy (TEM) is used to visualize the inner structure of particles and their size of any prepared NCs. Fig.3.19 shows TEM images at low and high resolution, respectively. Fig. 3.19A shows the presence of agglomerated particles, and Fig. 3.19B shows particles 5 nm in size which is microcrystalline in nature. The fingerprint-like appearance in the high resolution TEM image in Fig. 3.19C indicates the presence of internal crystalline nature within the particles. Such presence of the associated crystallite particles was also prominently observed in the optical microscopic images.

Fig.3.20-3.22 describe the TEM images of GO-CIHFO with EDX spectrum and elemental mapping. Fig.3.20 shows agglomerated fine particles of GO-CIHFO in addition with broken sheet of GO. Overlapping of figure print like structures (Fig.3.20B) in high resolution strengthen the degree of agglomeration of GO-CIHFO and anchoring of metal oxides in GO layers. Fig.3.20B revealed the microcrystalline nature of proposed material with average particle size ~ 2-3 nm. High agglomeration might be due to incorporation of metal oxides into the GO layers.

TEM-EDX spectrum (Fig.3.21) also supports the presence of higher carbon and oxygen content rather than iron and cerium that support the data acquired from SEM-EDX analysis. Signals for C and O along with iron and cerium suggested the incorporation of CIHFO on GO surface.Fig.3.22 represents the elemental mapping analysis for C, O, Fe and Ce also revealed that CIHFO mixed oxide particles evenly distributed on the surface of GO layer.

Fig.3.23-3.25 represents the overall impression of TEM analysis of βC-CIHFO including images, EDX spectrum and elemental mapping. Agglomerated fine particles of βC-CIHFO were pictorially presented in Fig. 3.23(A-B).In addition overlapping of figure print like structures Fig.3.23(C-E) in high resolution reinforce the degree of agglomeration of βC-CIHFO and anchoring of metal oxides within the cavity of β-cyclodextrin. Fig.3.23(C-E) revealed the microcrystalline nature of NCs with average particle size ~ 2-5 nm that almost support the particle size range obtained from AFM analysis. TEM-EDX spectrum (Fig.3.24) also expose higher carbon and oxygen content in proposed NCs rather than iron and cerium that also exhibit resemblance with the data assimilated from SEM-EDX analysis. Iron and cerium percentage also support the claimed CIHFO composite's elemental percentage. Signals for C and O along with iron and cerium suggested the affixing of CIHFO within the cavity of β-cyclodextrin.Fig.3.25 represents the chosen section for elemental mapping analysis and outcomes of such analysis for C, O, Fe and Ce. Presence of large quantity of carbon and oxygen along with proposed atomic ratio of Fe and Ce established that β-CD successfully modified CIHFO mixed oxide surface and CIHFO particles evenly unified with the cavity of β-CD.

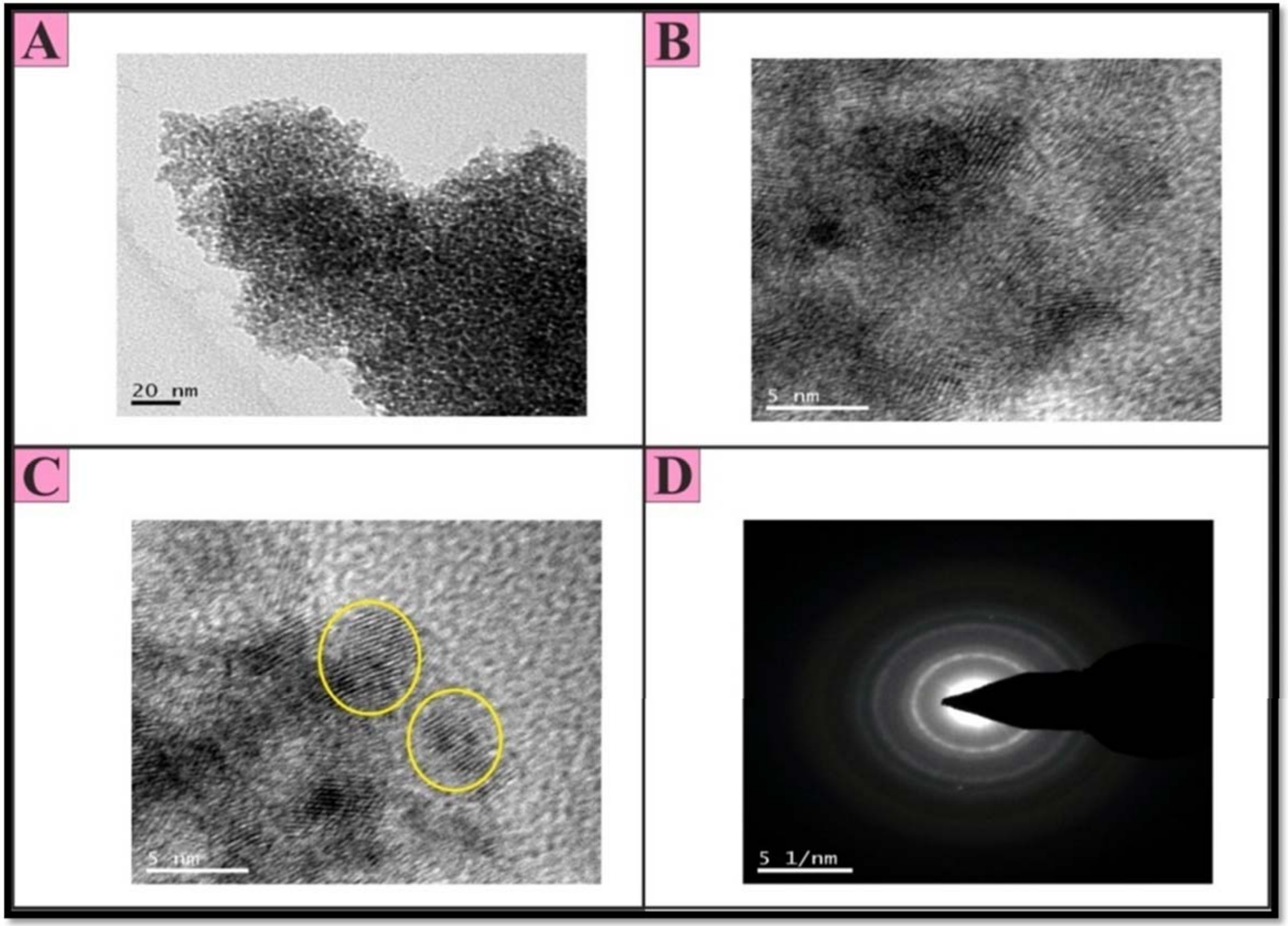

Fig. 3.19: (A) TEM images of CIHFO (20 nm scale); (B) TEM images of CIHFO (5 nm scale); (C) TEM images of CIHFO (5 nm scale with prominent figure print like structure; (D) SAED image obtained from TEM analysis of CIHFO (50 nm scale).

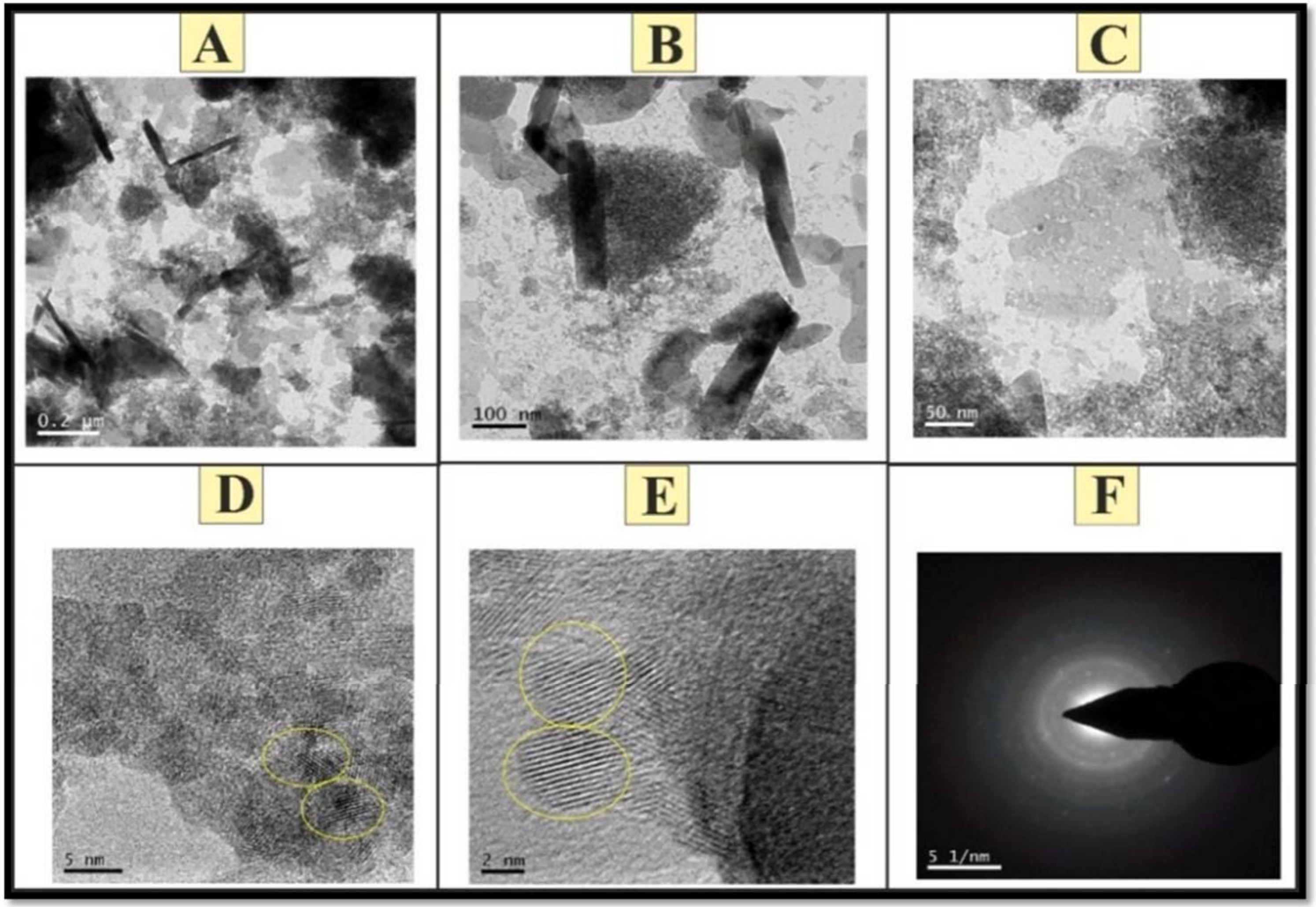

Fig. 3.20: (A) TEM images of GO-CIHFO (0.2µm scale); (B) TEM images of GO-CIHFO (100 nm scale); (C) TEM images of GO-CIHFO (50 nm scale); (D) and (E) TEM images of GO-CIHFO with prominent figure print like structure; (F) with SAED image of TEM images of GO-CIHFO (50 nm scale).

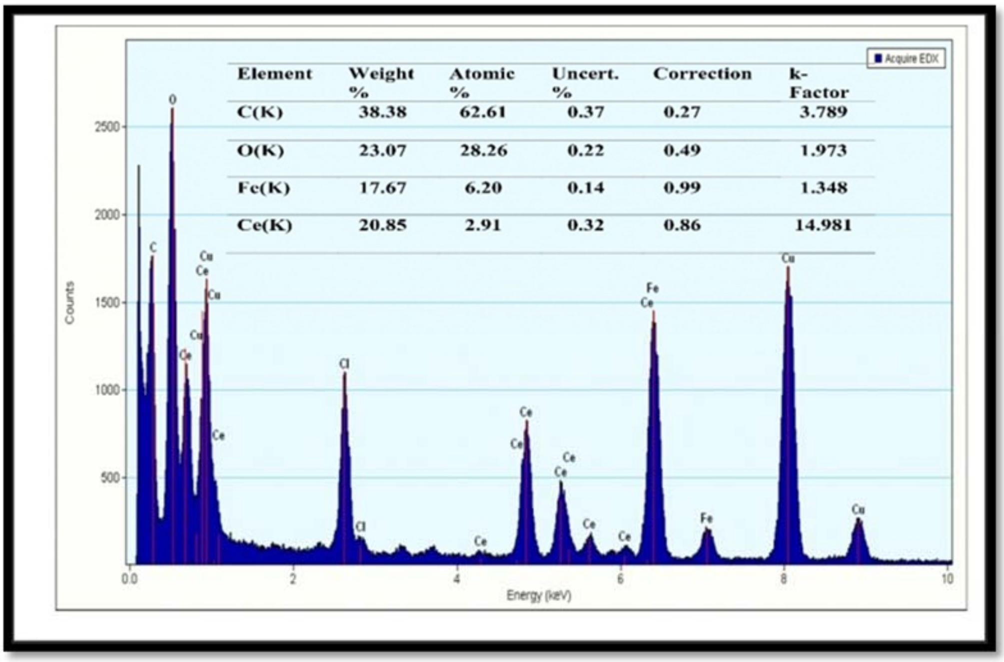

Element	Weight %	Atomic %	Uncert. %	Correction	k-Factor
C(K)	38.38	62.61	0.37	0.27	3.789
O(K)	23.07	28.26	0.22	0.49	1.973
Fe(K)	17.67	6.20	0.14	0.99	1.348
Ce(K)	20.85	2.91	0.32	0.86	14.981

Fig. 3.21: EDX spectrum of GO-CIHFO Nano-composite including quantification results.

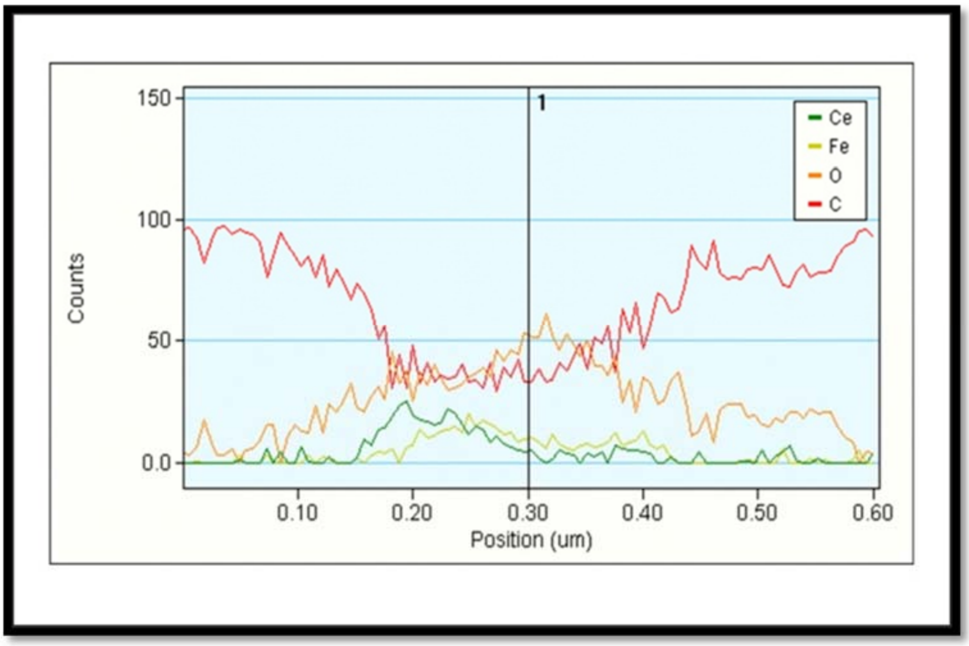

Fig. 3.22: Elemental mapping of C, O, Fe, and Ce respectively obtained from TEM analysis of GO-CIHFO.

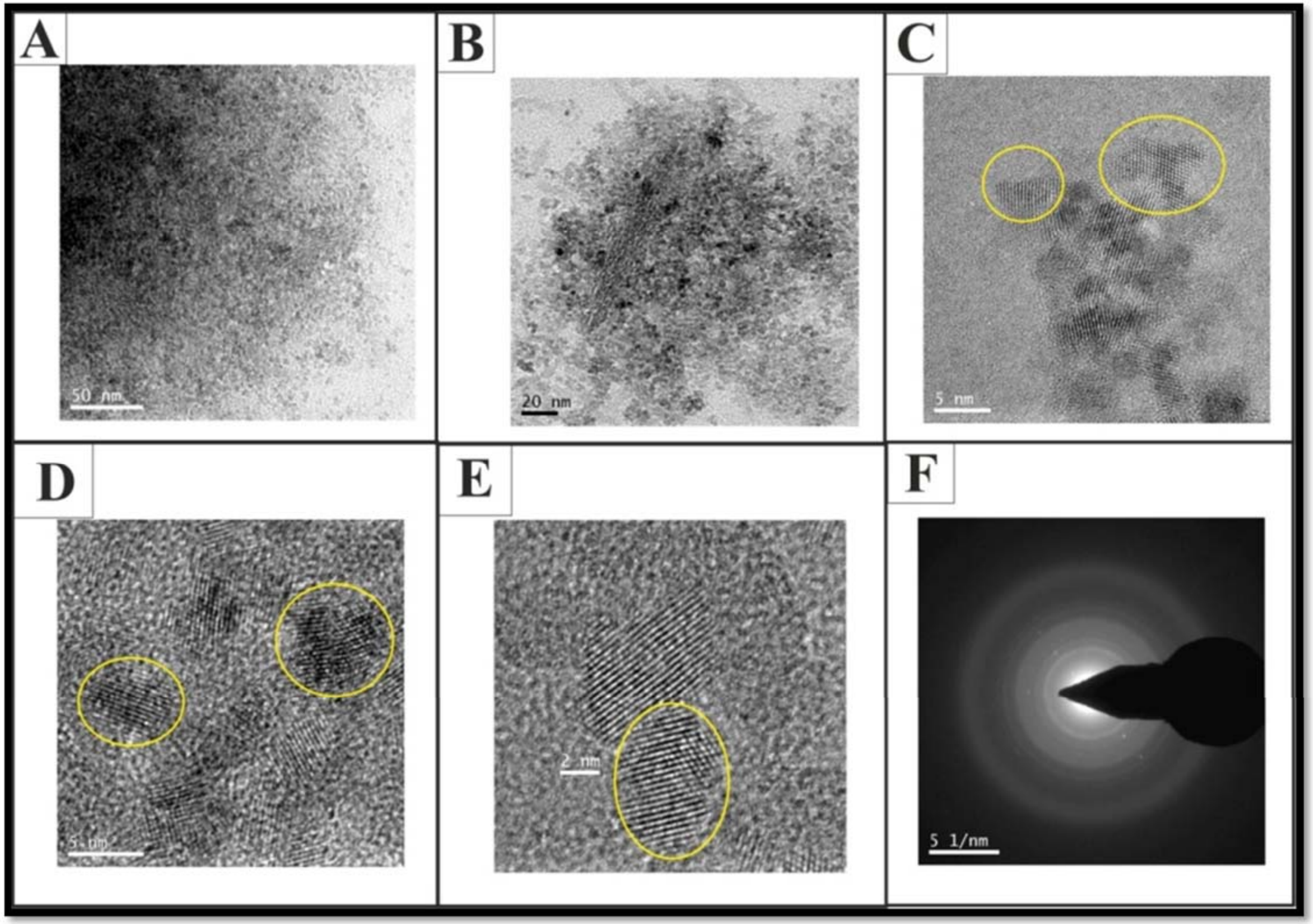

Fig. 3.23: (A) TEM image of βC-ClHFO (50 nm scale); (B) TEM image of βC-ClHFO (20 nm scale); (C-D) TEM images of βC-ClHFO (5nm scale);

(E) TEM images of βC-ClHFO (2 nm scale) with prominent figure print like structure; (F) with SAED image of TEM analysis of βC-ClHFO (50 nm scale).

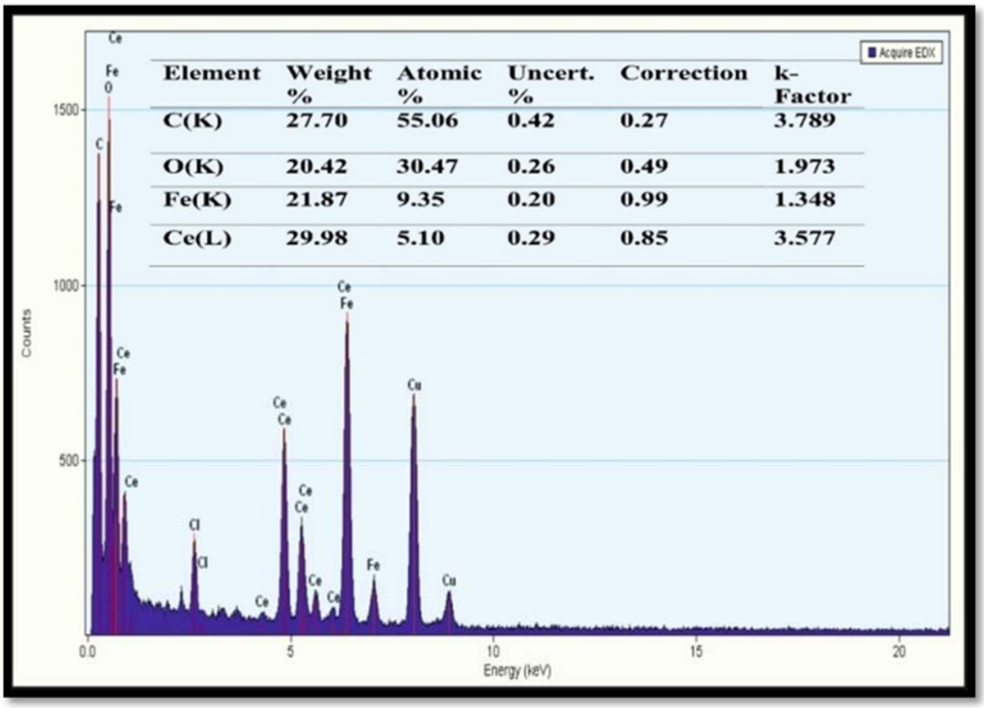

Element	Weight %	Atomic %	Uncert. %	Correction	k-Factor
C(K)	27.70	55.06	0.42	0.27	3.789
O(K)	20.42	30.47	0.26	0.49	1.973
Fe(K)	21.87	9.35	0.20	0.99	1.348
Ce(L)	29.98	5.10	0.29	0.85	3.577

Fig. 3.24: EDX spectrum of βC-CIHFO NCs including quantification results.

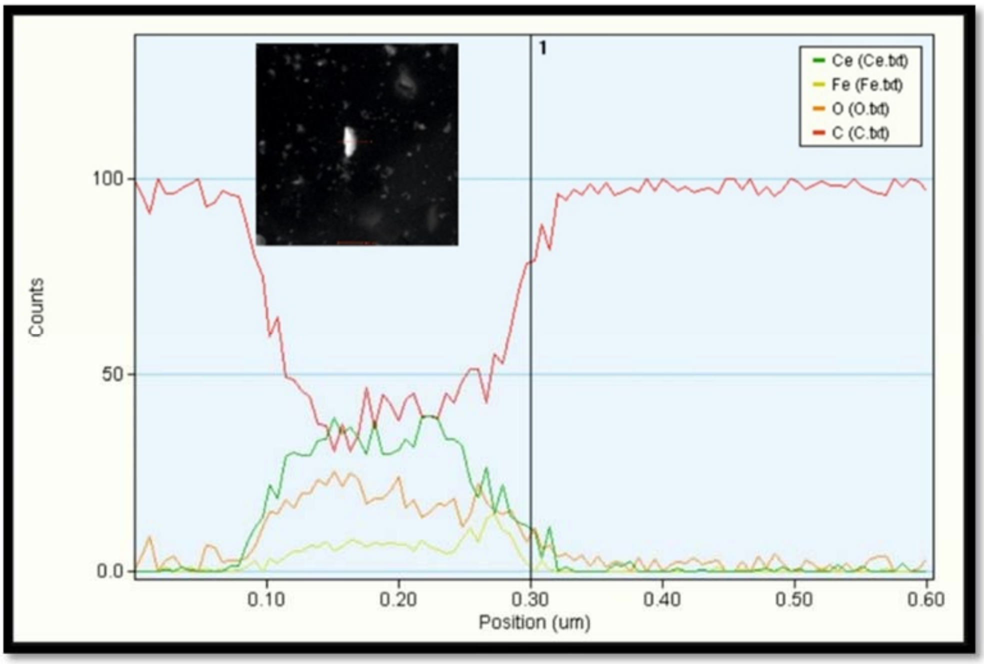

Fig. 3.25: Selected area (inset) of βC-CIHFO NCs for elemental mapping of C, O, Fe and Ce throughout the selected area.

3.2.6. AFM Analysis

Atomic force micrograph (AFM) image of any NCs provide information surface morphology of prepared composite. In present research work, all three proposed NCs namely CIHFO, GO-CIHFO and βC-CIHFO have been analysed with AFM and obtained results were presented in Fig.3.26, Fig.3.27 and Fig.3.28 respectively. It was observed for both 2D and 3D images of each proposed NCs exhibit rough and undulating nature of surface morphology. To acquire the surface profile, particle size approximation and their distribution pattern, a small portion of the 2D image was further extracted for each proposed NCs separately and obtained results were presented in mentioned figure. In case of GO-CIHFO NCs, Height distribution curve and extracted profile firmly recognised that more or less size of particles was ranged in 2-6 nm while indicating particle size distribution range established that average particle size is ~2.112 nm whereas for βC-CIHFO average particle size is ~6.022 nm. Both results support the particle size obtained from TEM images.

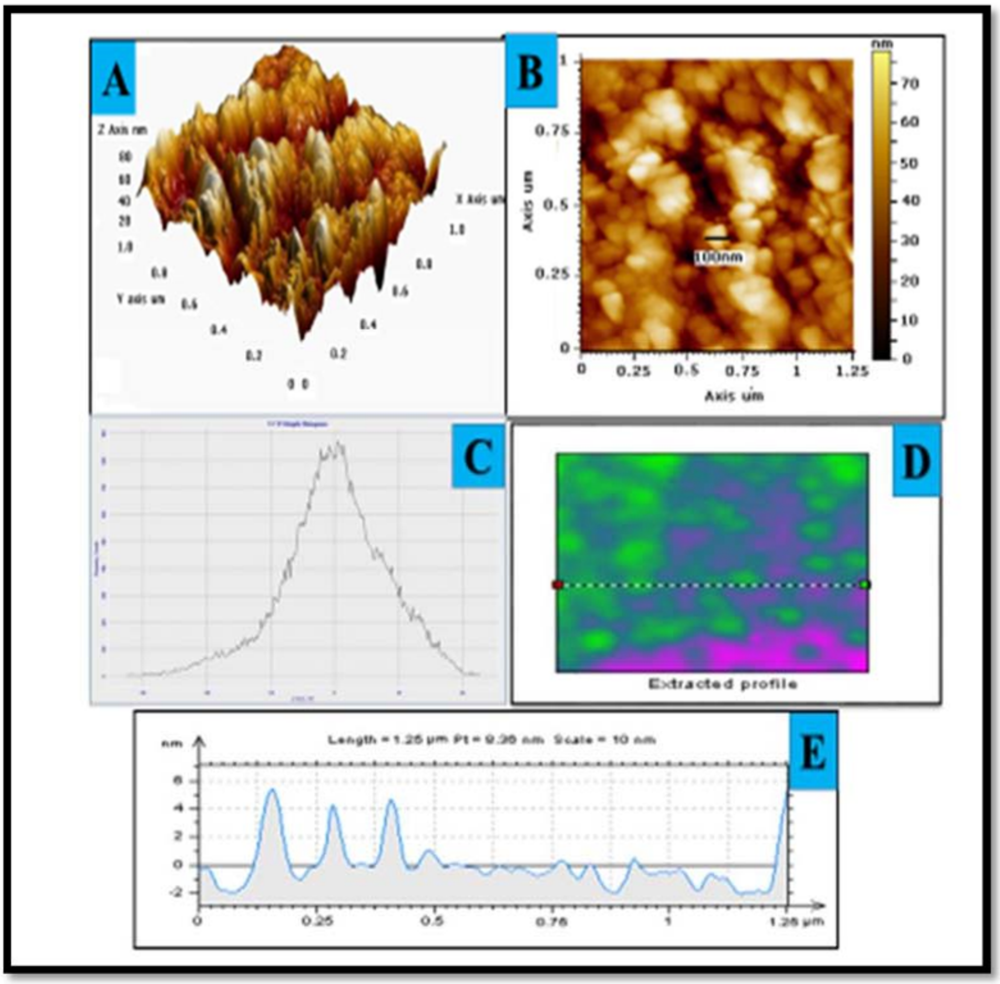

Fig. 3.26: (A) Atomic Force Microscopic image of CIHFO 3D view; (B) 2D view; (C) Height Distribution profile from the 2D image; (D) an extracted profile from the 2D image; (E) Length measurement.

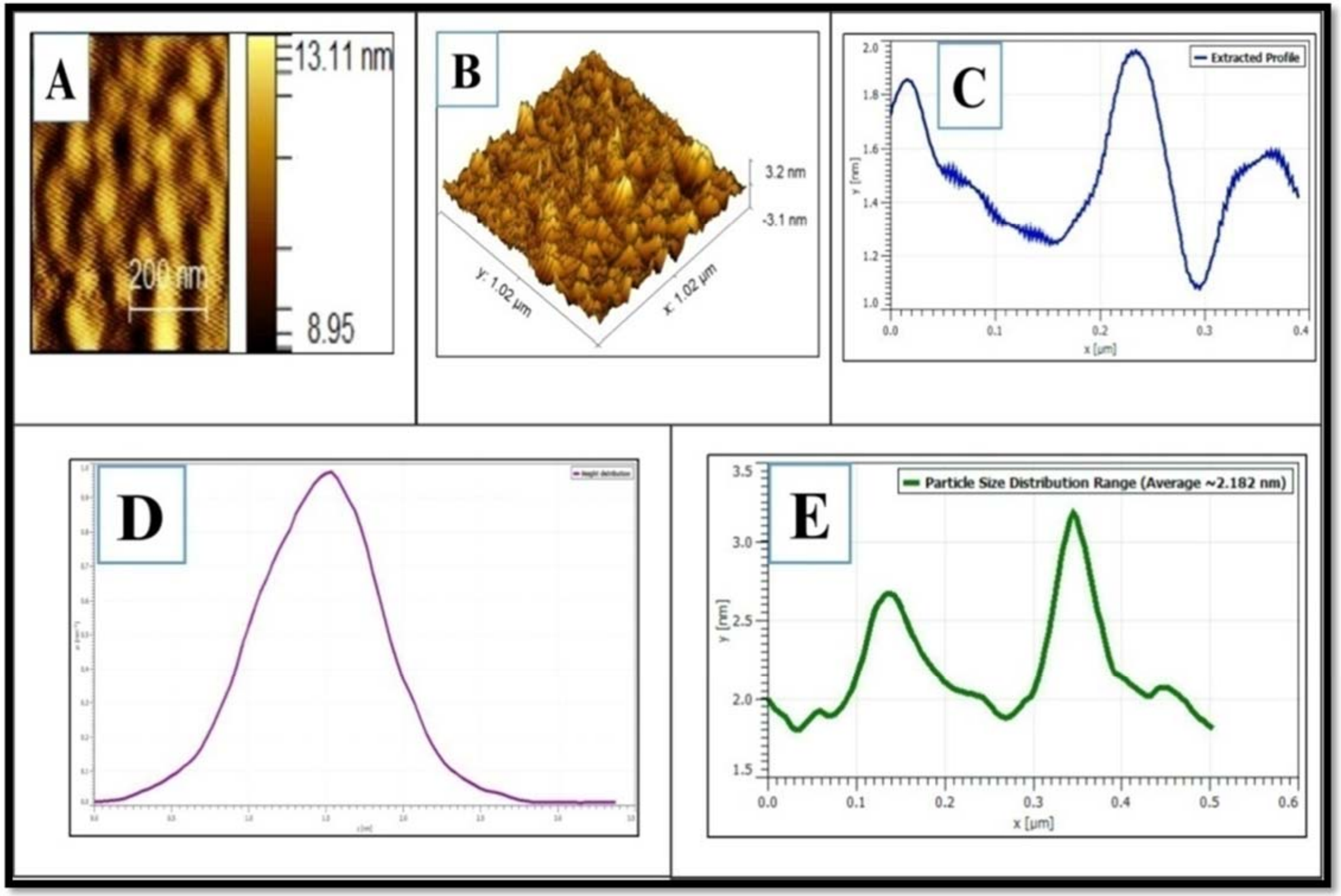

Fig. 3.27: (A) Atomic force microscopic images of surface of GO-CIHFO in 2D view; (B) in 3D view; (C) an extracted profile from the 2D image and (D) Height Distribution profile from the 2D image; (E) the particle size distribution range of GO-CIHFO.

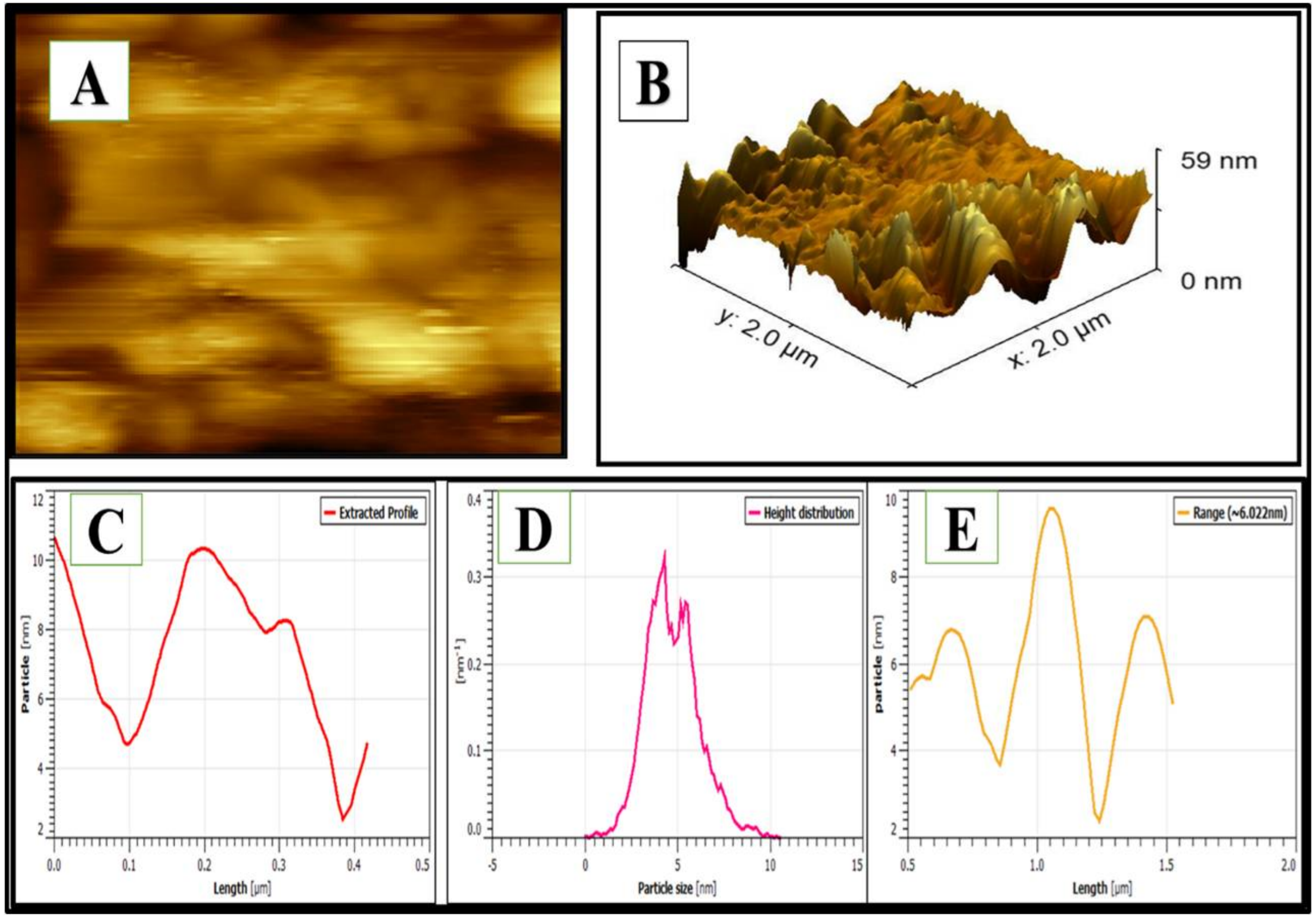

Fig. 3.28: (A) Atomic force microscopic images of surface of βC-CIHFO in 2D view; (B) in 3D view; (C) an extracted profile from the 2D image and (D) Height Distribution profile from the 2D image; (E) the particle size distribution range of βC-CIHFO.

3.2.7. Raman Analysis of GO-CIHFO

Raman spectroscopy is another useful tool that can provide authentic structural information for carbonaceous materials such as graphene. Raman spectra exhibited two distinctive D band and G band particularly for graphitic origin materials. For, pristine graphite D band obtained at 1351 cm^{-1} and G band at 1582 cm^{-1}. Sp^3 domains of carbon layers quietly associated D band while G band assigned with sp^2 in plane vibrations pattern. Fig.3.29A demonstrated the Raman spectra of GO, showing a prominent G band at 1592.13 cm^{-1} and blunt D band 1324.97 cm^{-1}. Any change of intensity of D band of G band often considered as indicator to quantify the extent of disorder associated with sp^2 and sp^3 domains of carbonaceous materials. It was observed that intensity ration (ID/IG) decreases from 1.02 to 0.99 when GO in incorporated with CIHFO lattice structure. Shifting of D band from 1324.97 cm^{-1} to 1305.59 cm^{-1} (lower frequency range) and G band from 1592.13 cm^{-1} to 1601.91 cm^{-1} (higher frequency range) ensure significant alteration of both sp^2 and sp^3 domains of GO after due to chemical doping with CIHFO and successful formation of composite (Fig.3.29B).

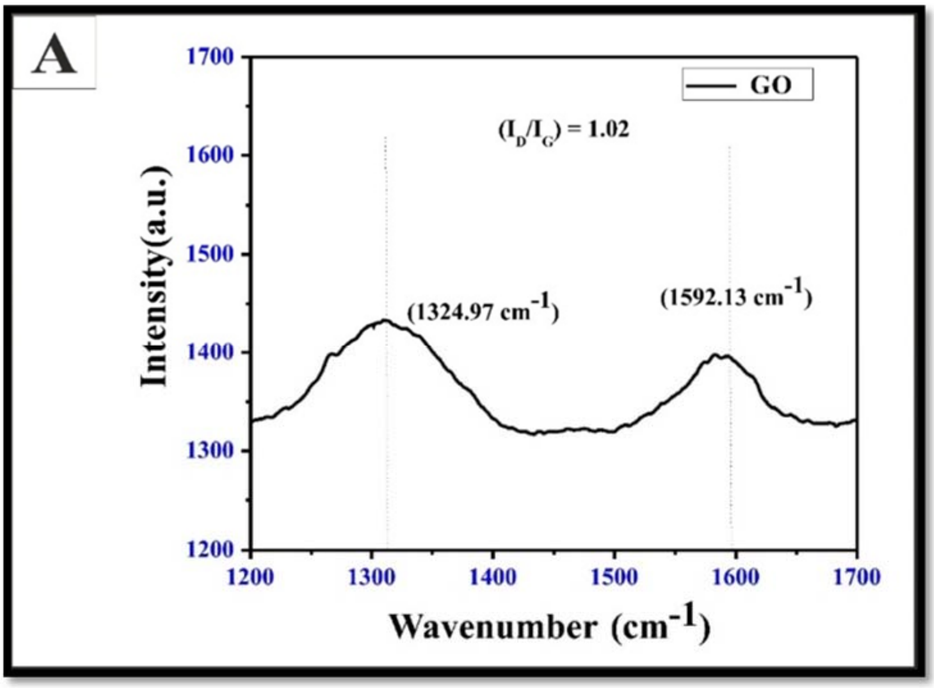

Fig. 3.29(A): Raman Spectra of GO

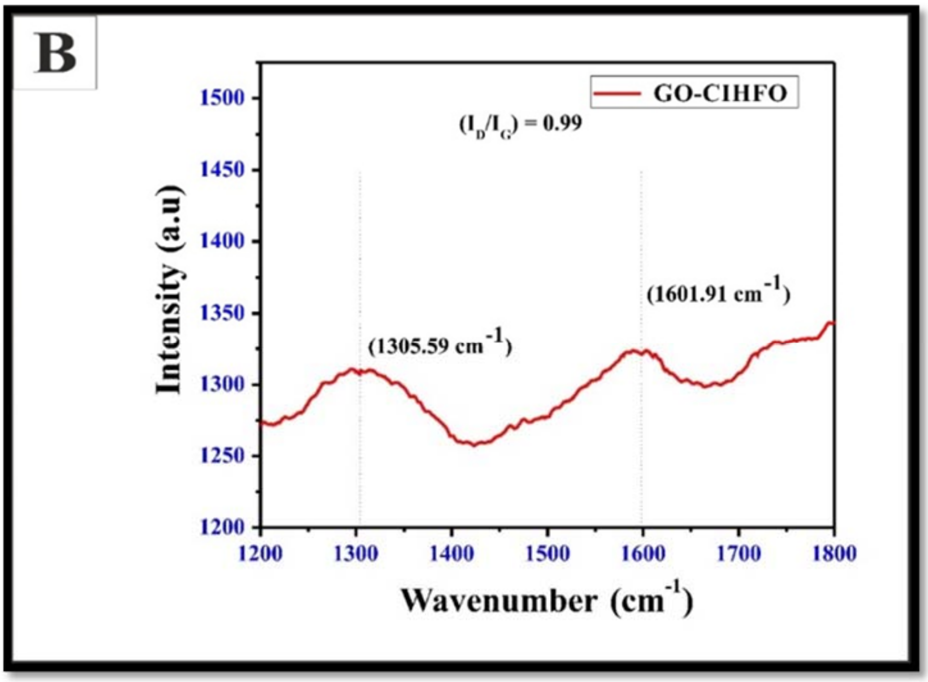

Fig. 3.29 (B): Raman Spectra of GO-CIHFO

3.2.8. Surface Area Analysis

BET analysis has been performed to determine specific surface area, pore size and pore volume of CIHFO, GO-CIHFO and βC-CIHFO before and after fluoride ions adsorption. For GO-CIHFO the N_2 adsorption/desorption isotherm curves for both before and after fluoride ions adsorption can be acknowledged as mixed isotherm, i.e. combination of type II and IV isotherms. Such pattern of BET isotherm occurs presumably due to the presence of different types of pores in the adsorbent. Round knee like appearance in lower relative pressure zone resemble to monolayer adsorption and low slope in middle of isotherm indicates first few multilayers adsorption layers strongly emphasized the presence of the type I isotherm. Development of Hysteresis loop in the desorption curve ensures the presence of type IV isotherm developed due to capillary condensation in mesoporous structures present in adsorbent. Specific surface area of GO-CIHFO before and after fluoride ions adsorption is 189.57 m^2 g^{-1} and 219.52 m^2 g^{-1} respectively. Surface area of CIHFO was 140.711 m^2 g^{-1} (Fig.3.30). Notable surface area enhancement observed after incorporation of GO in to CIHFO (GO-CIHFO) (Fig. 3.31). Increase in the surface area with decreasing trend in pore size support strongly the accumulation of fluoride ions within the pores of GO-CIHFO. Ionic radii of fluoride ions are much smaller than ionic radii of hydroxyl ions. Ionic exchange in between of F^- and OH^- supposed to be responsible for an enormous change in the structure of adsorbent which in turn enhance the surface area after fluoride adsorption. Pore volume before and after fluoride ions adsorption were found to be 0.147993 $cm^3.g^{-1}$ and 0.127207 $cm^3.g^{-1}$ respectively (Fig. 3.31C). The decrease in pores volume also supports the adsorption of fluoride ions inside the pores of the adsorbent materials which in turn increases the surface area of the adsorbent.

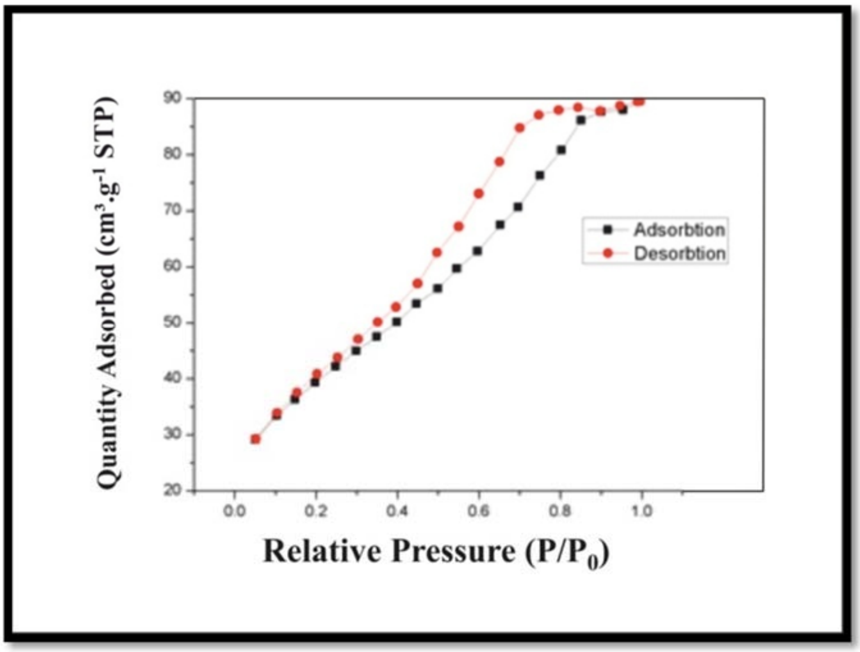

Fig. 3.30: Plots of N_2 (vapour) (cm^3. g^{-1}) adsorbed and desorbed against relative pressure for the BET isotherm plots of CIHFO for fluoride adsorption.

The N_2 adsorption/desorption isotherm curves for βC-CIHFO before fluoride adsorption in lower relative pressure zone with intermediate flat region in the isotherm resemble to monolayer adsorption and indicates the presence of the type II isotherm. Whereas, Occurrence of mixed isotherm pattern i.e. combination of type II and IV isotherms acknowledged with fluoride adsorbed βC-CIHFO. At lower pressure region, the graph is followed Type II adsorption pattern that indicates formation of monolayer followed by multilayers. Again appearance of hysteresis loop in the desorption curve ensures the presence of type IV isotherm. Presence of mesoporous structures within βC-CIHFO responsible for such loop formation. Fluoride adsorption capacity observed noticeably higher in βC-CIHFO than in CIHFO (140.711 m^2 g^{-1}) (Mukhopadhyay *et al*., 2017) although remarkable reduction in specific surface area after modification observed. Such reduction in specific surface area of βC-CIHFO might be resulted because of internal hindrance upon N_2 molecules to access the binding sites due to adherence of β-CD on the inorganic surface.

Specific surface area of adsorbent before and after fluoride ions adsorption is 1.0877 $m^2.g^{-1}$ and 104.8597 $m^2.g^{-1}$ respectively (Fig.3.32).The enhancement of the surface area with decrease in pore size after fluoride adsorption is closely associated with ionic exchange in between fluoride and hydroxyl ions. Relatively smaller fluoride ions can easily accumulated within the pores of βC-CIHFO supposed to be responsible for an enormous change in the structure of adsorbent which in turn enhance the surface area after fluoride adsorption.

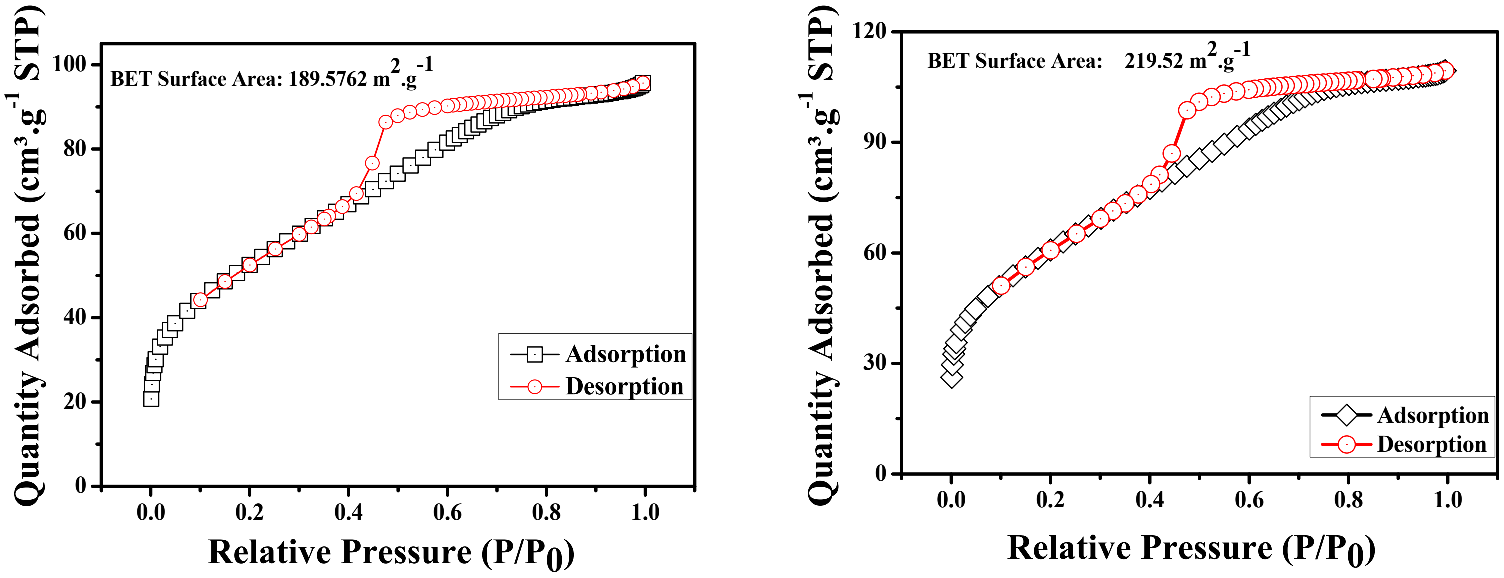

GO-CIHFO Adsorbent	Surface Area ($m^2.g^{-1}$)	Pore Size (nm)	Pore Volume ($cm^2.g^{-1}$)
Before fluoride adsorption	189.57	3.5486	0.147993
After fluoride adsorption	219.52	3.3958	0.127207

Fig. 3.31: Plots of N_2 (vapour) ($cm^3.g^{-1}$) adsorbed and desorbed against relative pressure for the BET isotherm plots of GO-CIHFO before fluoride adsorption and after fluoride adsorption upon GO-CIHFO and included table represents details of surface area change, pore size, pore volume before and after fluoride adsorption upon GO-CIHFO.

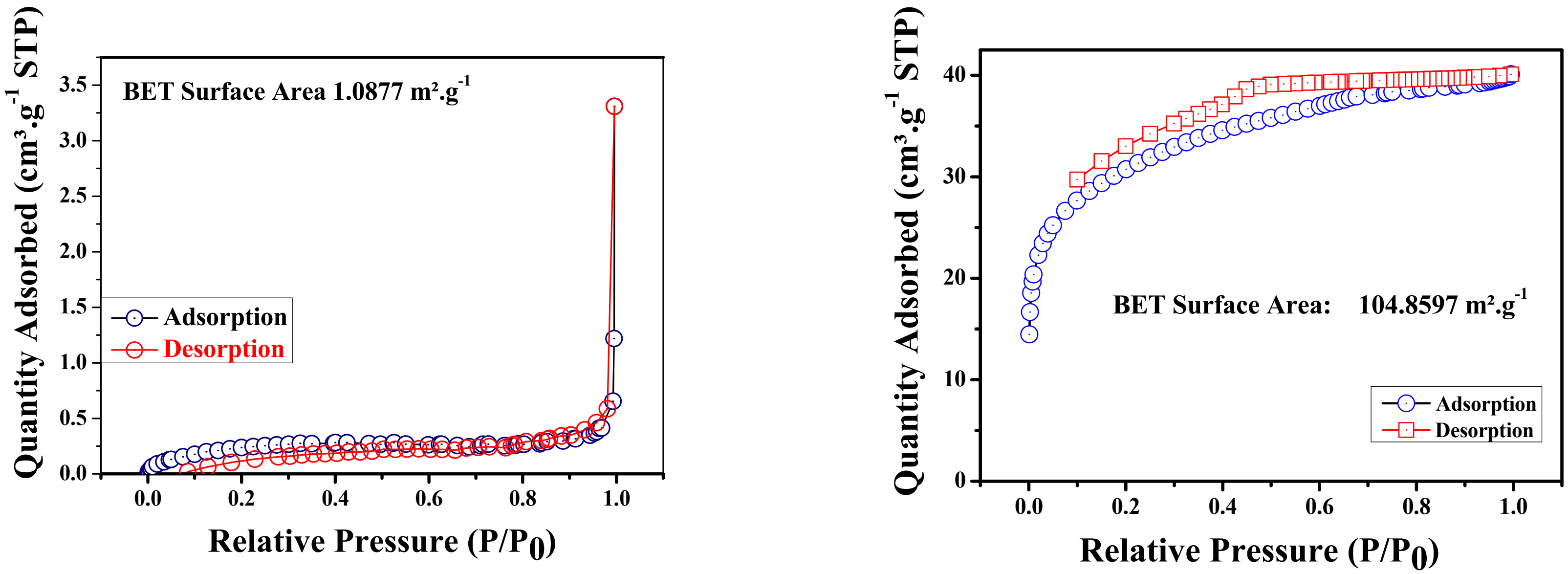

βC-CIHFO Adsorbent	Surface Area ($m^2.g^{-1}$)	Pore Size (nm)	Pore Volume ($cm^2.g^{-1}$)
Before fluoride adsorption	1.0877	10.6040	0.000682
After fluoride adsorption	104.8597	3.0585	0.027089

Fig. 3.32: Plots of N_2 (vapour) (cm^3. g^{-1}) adsorbed and desorbed against relative pressure for the BET isotherm plots of βC-CIHFO before fluoride adsorption and after fluoride adsorption upon βC-CIHFO and included table represents details of surface area change, pore size, pore volume before and after fluoride adsorption upon βC-CIHFO.

3.2.9. XPS Analysis of GO-CIHFO

Elemental or chemical state determination of prepared composite was also established further using XPS technique. In this technique irradiating sample with X-ray photon and analyse the emitted core-level electron. The emitted electron has a peculiar kinetic- and binding energy of the atomic orbital of certain atom dependent on the incident X-ray. The binding energy of the emitted photoelectrons are analysed to identify the elements present (Briggs, 1981). XPS of GO incorporated CIHFO has been recorded for identify the carbon, oxygen, iron and cerium and shown in Fig.3.33. The full spectrum of composite material has been shown in Fig. 3.33A. The observed C 1s spectrum (Fig. 3.33B) clearly indicates the presence of GO in the composite. The peaks at 284 and 288.3 eV are corresponding to C-C and C=O respectively (Drewniak *et al.*, 2016). The O 1s peak obtained between 529 (Ce^{4+}-O) to 530.5 eV ($Fe^{2+/3+}$-O) corresponds to metal oxides, the spectrum further broadens up to ~533 eV (C=O) corresponds to carbonyl moiety from GO shown in Fig. 3.33C (Baltrusaitis *et al.*, 2007).Further the peaks at 710 (Fe $2p_{3/2}$), (Hu *et al.*, 2014) (Langevoort *et al.*, 1987; Wan and Wang, 2016) 718.4 (Fe satellite), 723.6 (Fe $2p_{1/2}$) (Wan and Wang, 2016) and 732.4 (Fe satellite) (Baltrusaitis *et al.*, 2007) confirms the presence of Fe-O component of the material (Fig.3.33D). The Ce 3d XPS spectrum exhibited Gaussian-like appearance (Tang and Zhang, 2016) that resemblance of presence Ce^{4+} that Finally, were established from the spectrum of Fig. 3.33E, which shows peaks at 881.7, 888.9, 897.4, 900.2, 906 and 915.9 eV, corresponds to Ce^{4+}-O (Yu *et al.*, 2017).

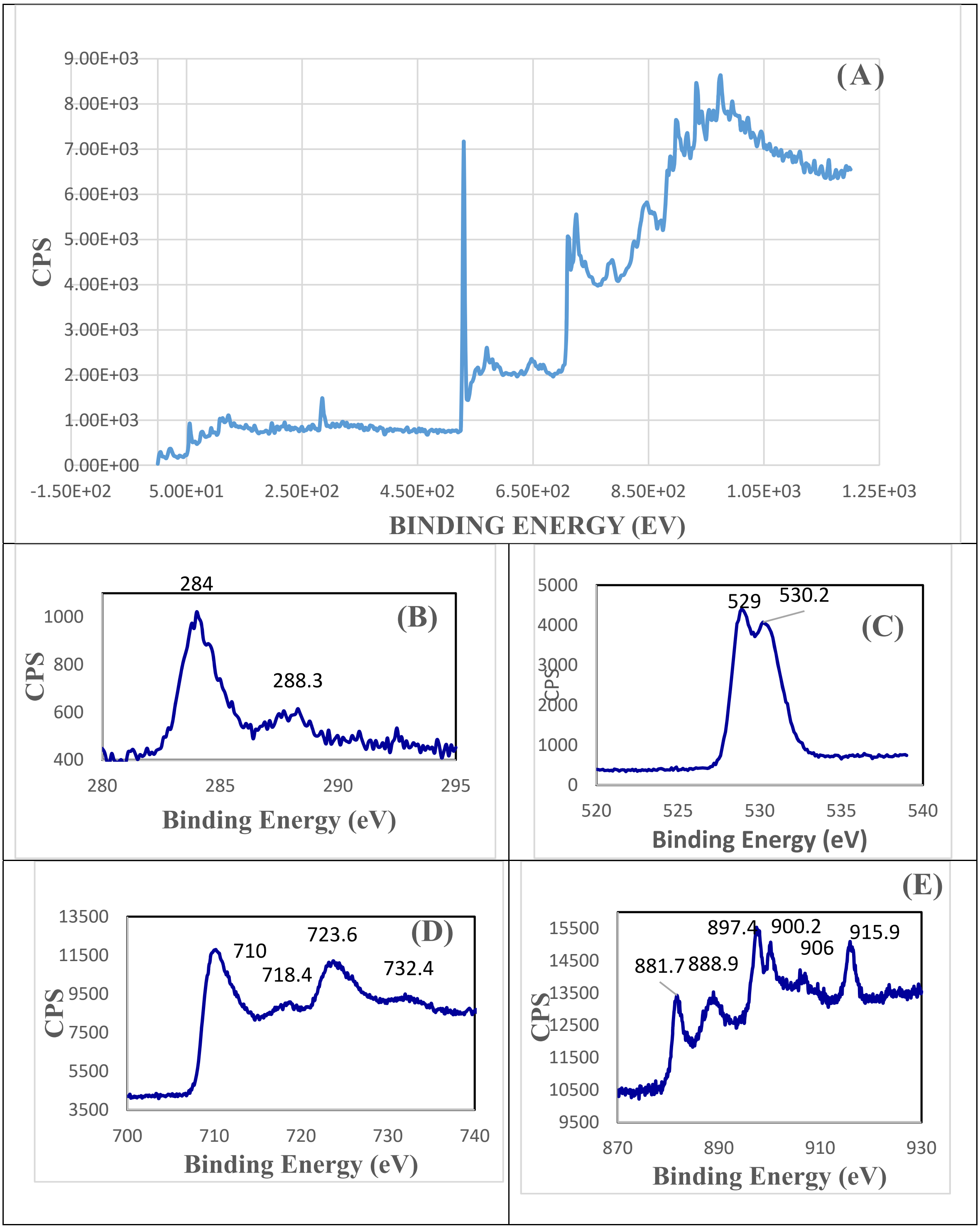

Fig. 3.33: XPS spectrum of the CIHFO shows (A) Full spectrum,(B) C 1s spectrum, (C) O 1s spectrum, (D) Fe 2p spectrum and (E) Ce 3d spectrum.

3.3. Batch Adsorption Study

3.3.1. Influence of Cerium Content in CIHFO on Fluoride Adsorption

Significant change in fluoride adsorption capacity has been noticed with changing of the Fe (III) to Ce (IV) mole ratio in CIHFO from 1.0: 0.0 to 0.0:1.0. Fluoride adsorption increased with enhancement of cerium content from 1.0:0.0 to 1.0:0.5, and declined there after till the Fe: Ce mole proportion changed to 1:1 (Fig.3.34). In this particular study, fluoride adsorption is highest for pure hydrous cerium oxide (HCO) (25.3 mg.g^{-1}). But fluoride adsorption capacity is appreciably high compared to pure hydrous iron oxide (HFO) (8.4 mg.g^{-1}) when Fe: Ce = 1.0: 0.5. This might be beneficial when cost of proposed adsorbent is major concern.

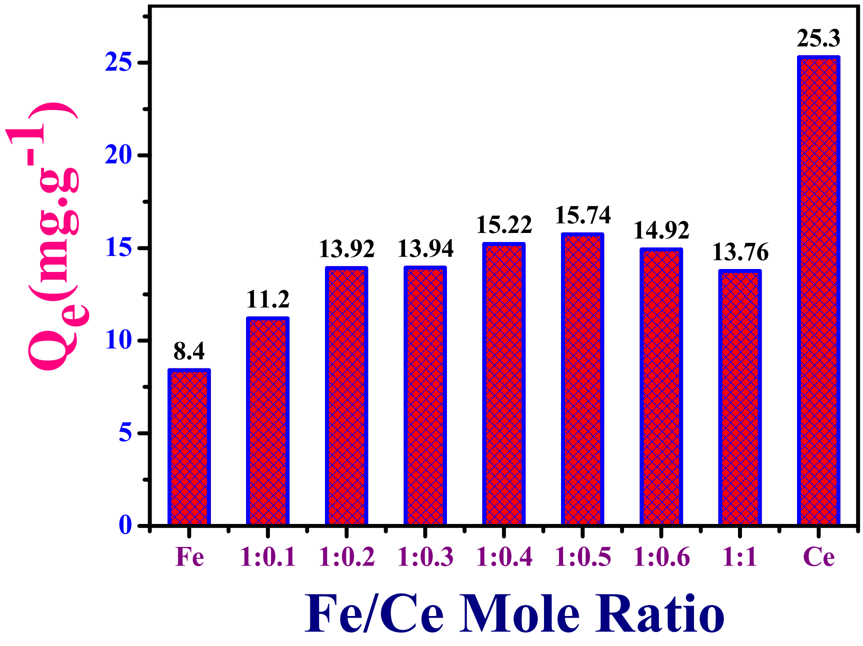

Fig. 3.34: Effect of Fe**:**Ce mole ratio variation on fluoride adsorption capacity of when adsorbent dose: 0.05 g per 100 mL of 15.0 mg.L^{-1} fluoride solution in pH: 7.0 (± 0.2), agitation time: 60 min.

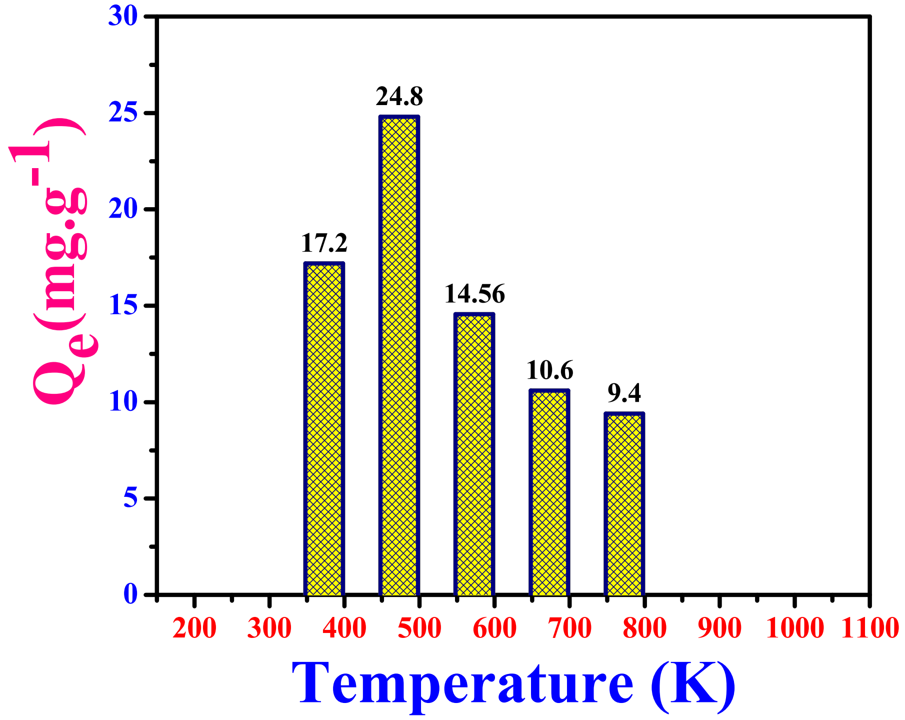

Fig. 3.35: Effect of calcined temperature on fluoride adsorption capacity of CIHFO (Fe/Ce -1.0:0.5) when adsorbent dose: 0.05 g per 100 mL of 15.0 mg.L^{-1} fluoride solution in pH: 7.0 (± 0.2), agitation time: 60 min.

Fig.3.35 depicts the effect of calcination temperature upon the fluoride adsorption capacity (mg.g^{-1}) of CIHFO. It was observed that fluoride adsorption capacity decreased consecutively with the increase of temperature at and above 300°C (573K). Adsorbent, when calcined at 200°C (473K) exhibited a maximum fluoride adsorption capacity (24.8 mg.g^{-1}) with initial fluoride concentration 15.0 mg.L^{-1}. CIHFO was prepared by simple co-precipitation method ensure formation of hydrous oxides of iron and cerium. Such surface active hydroxyl groups of metal oxides were presumably acted as adsorption sites for fluoride adsorption. At calcination temperature 473K, hydrogen bonds the surface water molecules were breaking down which in turn exposed the surface hydroxyl groups to the solute for adsorption reaction, indicating higher adsorption value. With increase of calcined temperature (>473K), such hydroxyl groups are easily removed from the surface of metal oxides, resulting in lower adsorption capacity of proposed adsorbent.

3.3.2. Influence of Percentage of Graphene Oxide Content in CIHFO on Fluoride Adsorption

To evaluate the effect on fluoride adsorption capacity after doping of GO into the surface of CIHFO, a series of batch experiments have been conducted (Fig.3.36).

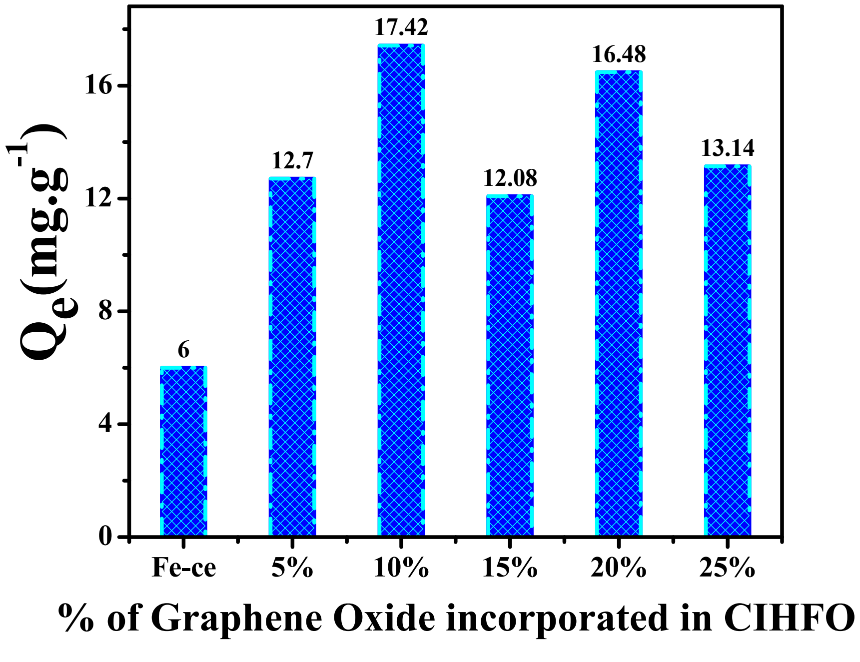

Fig. 3.36: Study of Percentage variation of Graphene Oxide in association within CIHFO and its effect upon fluoride adsorption efficacy (Adsorbent dose: 0.05 g per 50 mL of 10.0 mg.L^{-1} fluoride solution in pH: 7.0 (± 0.2), agitation time: 120 min.

It was observed that with increase of weight percentage of GO up to 10%, fluoride adsorption capacity of GO-CIHFO has been increased in contrast to pure mixed metal oxide. After such percentage level of GO incorporation, no such noticeable increment in fluoride adsorption capacity observed.

3.3.3. Influence of Molar Concentration Variation of Beta Cyclodextrin (β-CD) Solution for Synthesis of βC-CIHFO and Its Impact on Fluoride Adsorption

Increase in molar concentration of **β-CD** during synthesis of NCs βC-CIHFO in both solution pH 3.0 and pH 7.0, have been shown that fluoride adsorption capacity of βC-CIHFO improved up to 0.04M solution concentration of **β-CD** then declined (Fig.3.37). Hence, 0.04M **β-CD** optimised for the formation of βC-CIHFO NCs.

The main aim of this study is to develop a cost effective material as water purifier that can be applied in any fluoride affected region in and around India, particularly in effected region of West Bengal (India) in affordable price. To achieve this goal, 10% **GO** incorporated within CIHFO (GO-CIHFO) and 0.04M **β-CD** solution optimised for synthesis of βC-CIHFO are selected for rest of the experimental studies.

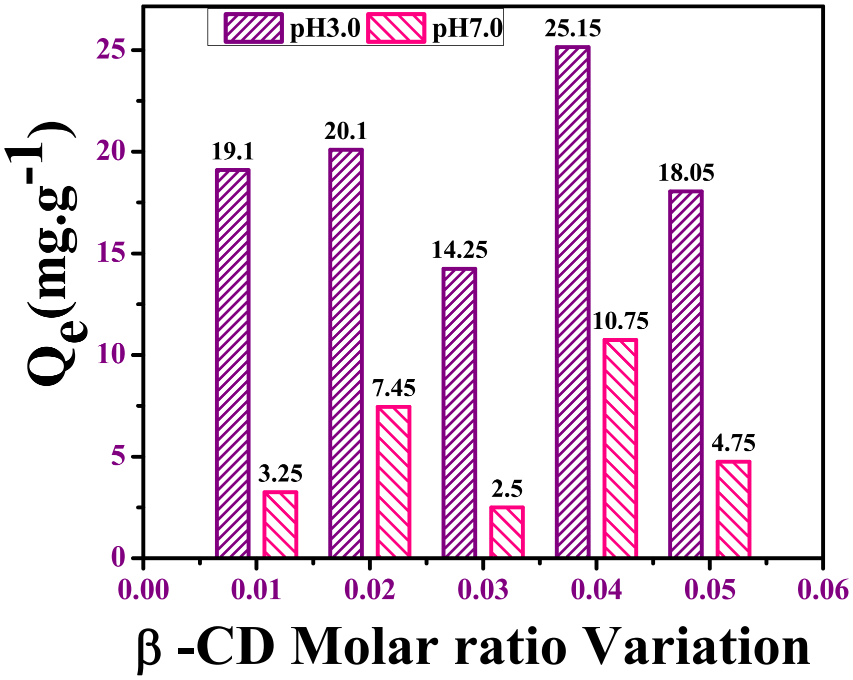

Fig. 3.37: Study of effect of β-CD Molar ratio variation within CIHFO and its effect upon fluoride adsorption efficacy (Adsorbent dose: 0.01 g per 50 mL of 10.0 $mg.L^{-1}$ fluoride solution in both pH: 3.0 (± 0.2), and pH: 7.0 (± 0.2), agitation time: 120 min.)

3.4. Effect of Adsorbent Dose

To determine the effect of adsorbent dose on fluoride removal, adsorbent dose was varied from 0.05 to 2.0 g CIHFO per 100 mL fluoride solution of (C_i = 10.0, 15.0 and 20.0 $mg.L^{-1}$); 0.01 g to 1.0 g GO-CIHFO NCs in 50 ml of fluoride solution (C_i =10 and 15 $mg.L^{-1}$) and 0.01 g to 1.0 g βC-CIHFO NCs in 50 ml of fluoride solution (C_i = 20 $mg.L^{-1}$) for adsorption reaction at 30°C (303 K) and at pH_i~ 7.0 and 3.0 respectively.

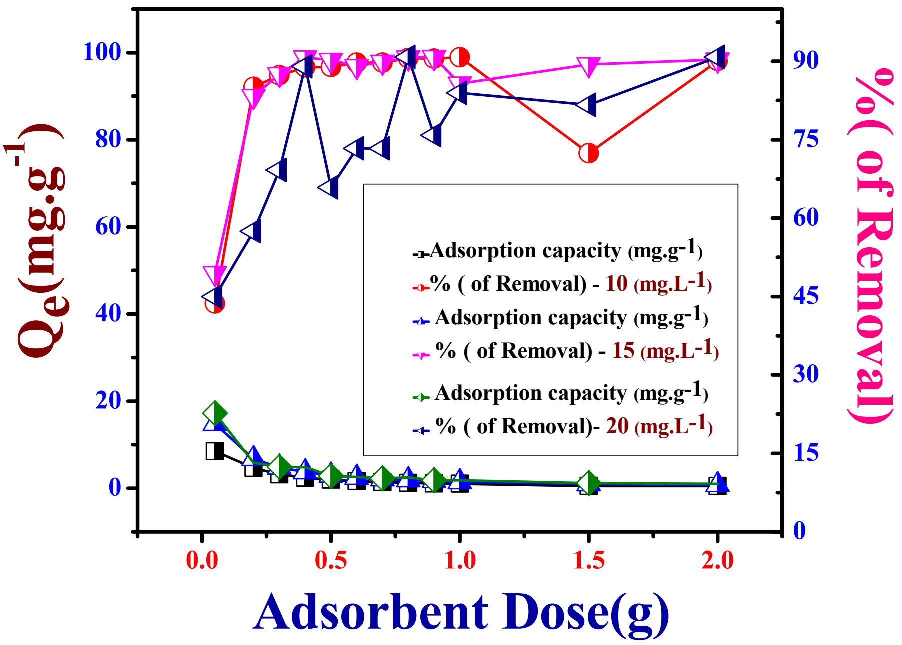

Fig. 3.38: Effect of CIHFO dose variation on the fluoride adsorption capacity and percentage of fluoride removal in three different concentrations at pH 7.0 (±2).

It has been noticed that the fluoride adsorption capacity (Q_e, $mg.g^{-1}$) declined for a given C_i value with the increase of adsorbent dose (Fig.3.38, Fig.3.39 and Fig.3.40). This phenomenon can be well elucidated by the surface sites heterogeneity model. As per this model, any surface sites are composed of a series of spectrum of binding energies. When dose applied in minute quantity, then availability of exposed surface sites enhanced the adsorption capacity (Q_e) value. Reversible condition will set on with rise of adsorbent dose, which is similar with other researchers(Biswas et al., 2009; Ghosh et al., 2014; Saha et al., 2016).

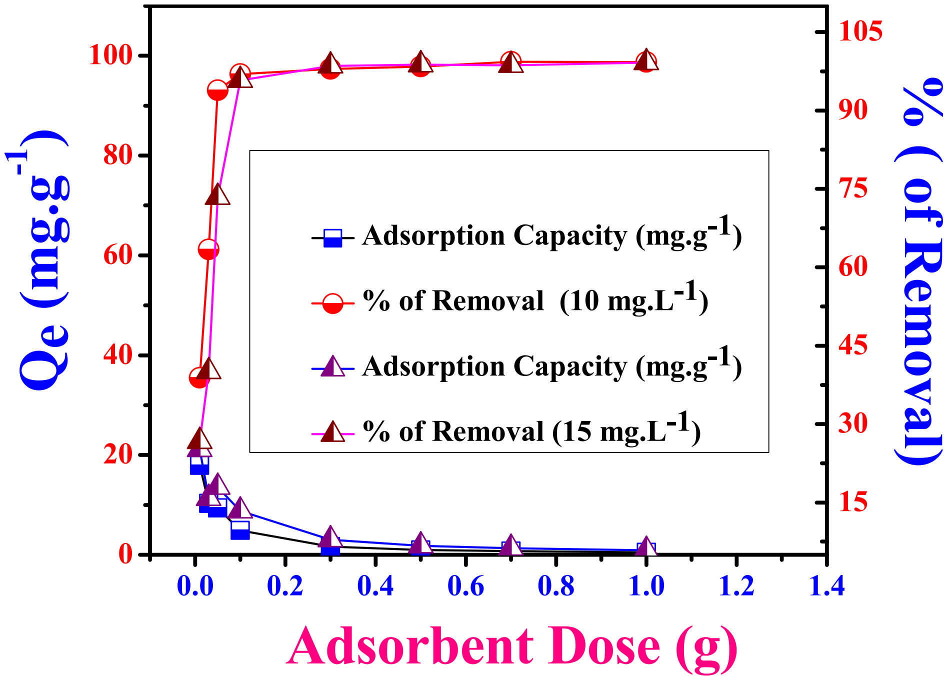

Fig. 3.39: Effect of GO-CIHFO dose variation on the fluoride adsorption capacity and percentage of fluoride removal in two different concentrations at pH 7.0 (±2).

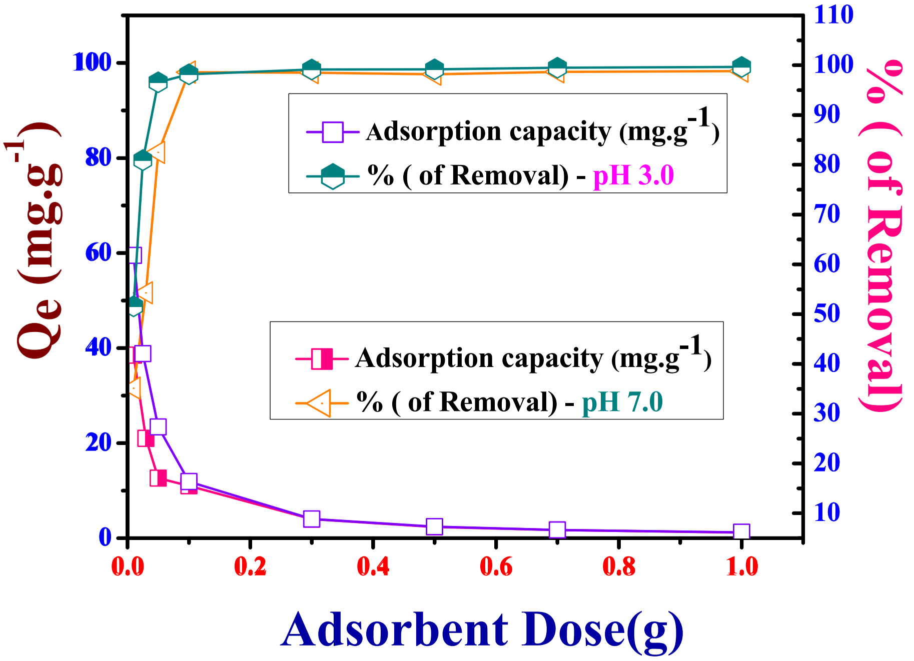

Fig. 3.40: Effect of βC-CIHFO dose variation on the fluoride adsorption capacity and percentage of fluoride removal at pH 3.0(±2) and pH 7.0 (±2) respectively.

3.5. Effect of pH upon Fluoride Adsorption Capacity of CIHFO, GO-CIHFO and βC-CIHFO

Initial solution pH and pH_{ZPC} of any adsorbent are considered as two important factors that play a crucial role in any adsorption mechanism of adsorbate over adsorbent. Adsorption of any anion is influenced by the presence of hydroxyl ions in solution. To apprehend fluoride adsorption over all these three adsorbent, a set of experiments were carried out in the pH range 3-10, in room temperature. The pH_{ZPC} of CIHFO, GO-CIHFO and βC-CIHFO was found to be (5.2, ±0.2), (6.2, ±2) and (6.4, ±0.2) respectively, depicting that the adsorbent surface is positive below pH_{ZPC} and negative above pH_{ZPC}. Fig.3.41 (A-C) and Fig.3.42 (A-C) represents pictorial explanation of the effect of pH on fluoride adsorption capacity of three adsorbents and pH_{ZPC} of three adsorbents as well.

It was observed from experimental results that maximum equilibrium adsorption capacity obtained at pH 3.0 for all fluoride concentrations. Moreover, the fluoride adsorption capacity of all adsorbents reduced drastically at $pH > 7$. Such declining trend of fluoride uptake capacity can be justified by the fact that with increasing pH the adsorbent retains a negative surface charge ($pH > pH_{zpc}$), that lean towards columbic repulsion for negatively charged fluoride ions. Concentration of hydroxyl ions (OH^{-1}) also increase at basic pH range that also competed with the fluoride for the active binding sites of the adsorbent (Barathi *et al*., 2014; Mohan *et al*., 2016; Mukhopadhyay *et al*., 2017).

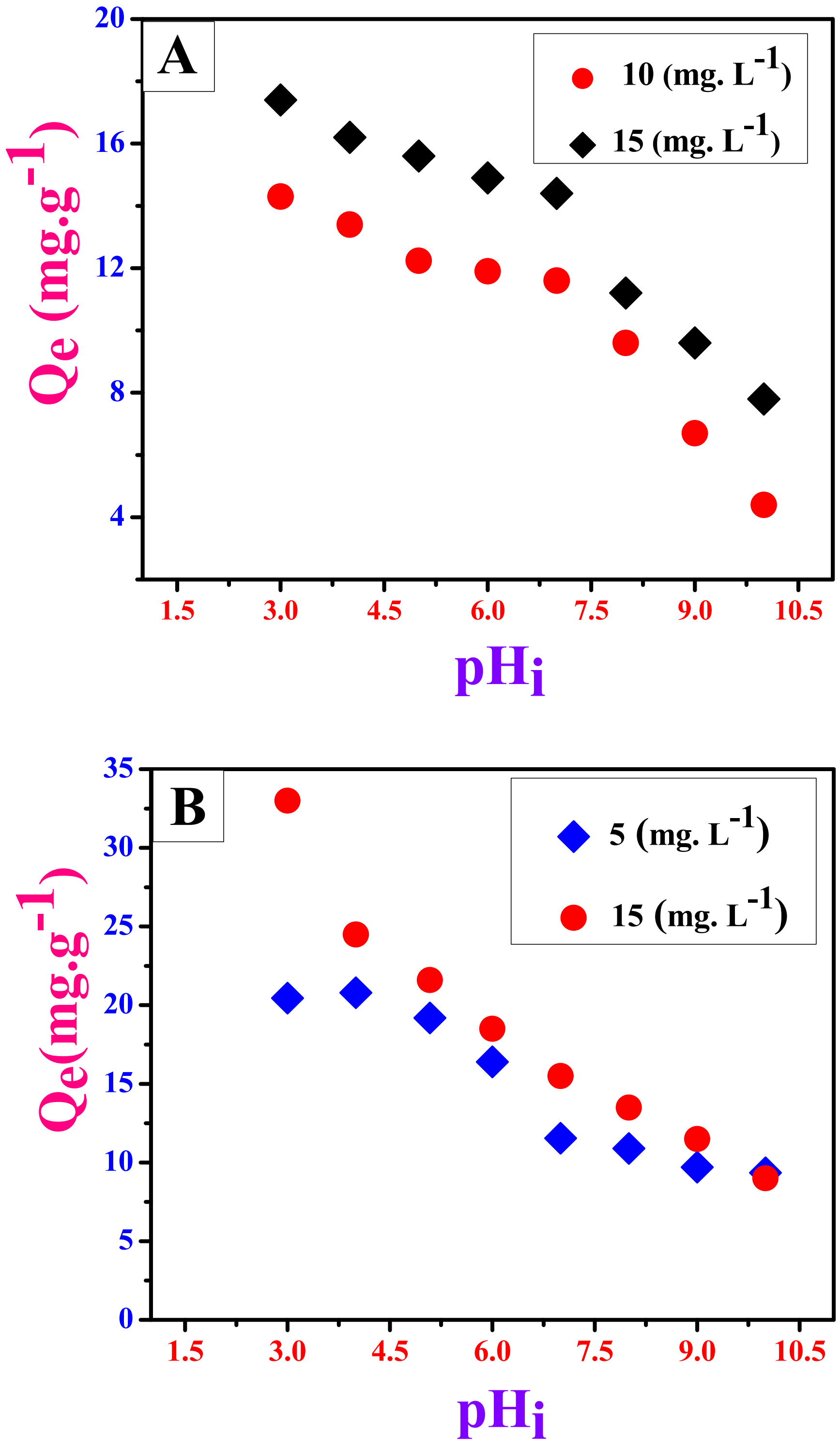A
10 (mg. L^{-1})
15 (mg. L^{-1})
Qe (mg.g^{-1})
20
16
12
8
4
1.5
3.0
4.5
6.0
7.5
9.0
10.5
pH$_i$
B
5 (mg. L^{-1})
15 (mg. L^{-1})
Qe(mg.g^{-1})
35
30
25
20
15
10
5
0
1.5
3.0
4.5
6.0
7.5
9.0
10.5
pH$_i$

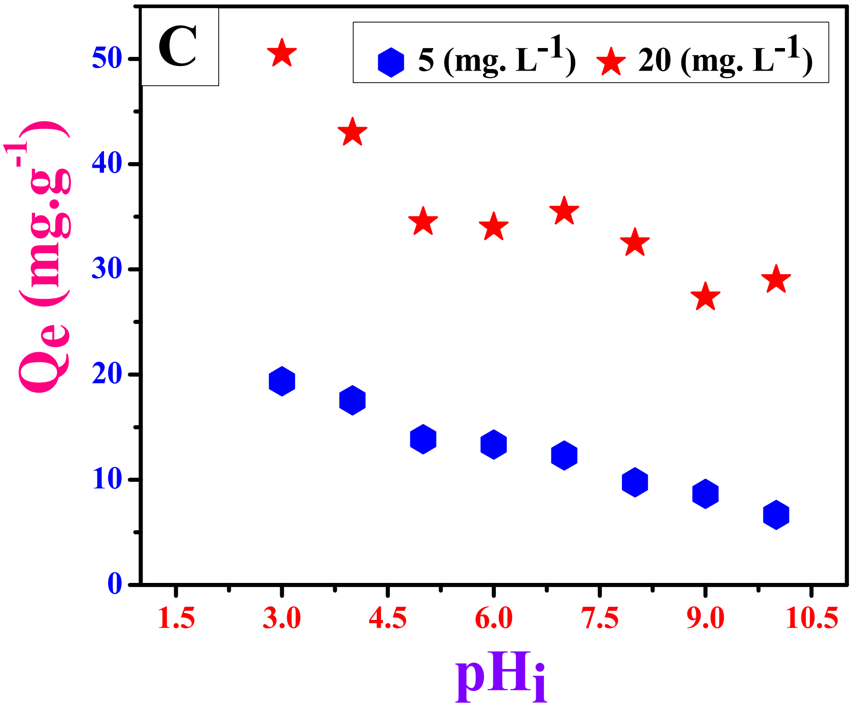

Fig. 3.41: (A)-(C) Plots of Initial solution pH versus fluoride adsorption capacity to evaluate effect of initial pH upon fluoride adsorption of three synthesized adsorbents CIHFO, GO-CIHFO and βC-CIHFO respectively.

As per HSAB principle, Fe^{3+} and Ce^{4+} are act as hard acid. Hard acids prefer binding to the hard bases to give ionic complexes. In aqueous medium, Fe^{3+} and Ce^{4+} could be present as cationic hydroxide forms and could easily interact with fluoride ions by electrostatic attraction and replace the OH^- from hydrous metal oxides via ion exchange (R_1). When solution pH is in acidic range, protonation of surface take place and adsorption occurs by electrostatic interaction (R_2 and R_3);

$M\text{-}OH + F^- \rightarrow M\text{-}F + OH^-$ (M- Fe^{3+}, Ce^{4+}) ($pH < pH_{ZPC}$) [R_1]

$M\text{-}OH_2^+ + F^- \rightarrow M\text{-}F + H_2O$ (M- Fe^{3+}, Ce^{4+}) [R_2]

$O\text{-}H + F^- \rightarrow O\text{-}H\cdots F^-$ [R_3]

At basic solution pH range, deprotonation of surface occurs. In such condition, adsorbent surface is to be negative and imparts columbic repulsion on fluoride ion. This can be demonstrated by (R_4).

$\text{M-OH} + F^- + OH^- \rightarrow \text{M-O}^- + F^- + OH_2$ (M- Fe^{3+}, Ce^{4+}) (pH> pH_{ZPC}) [R_4]

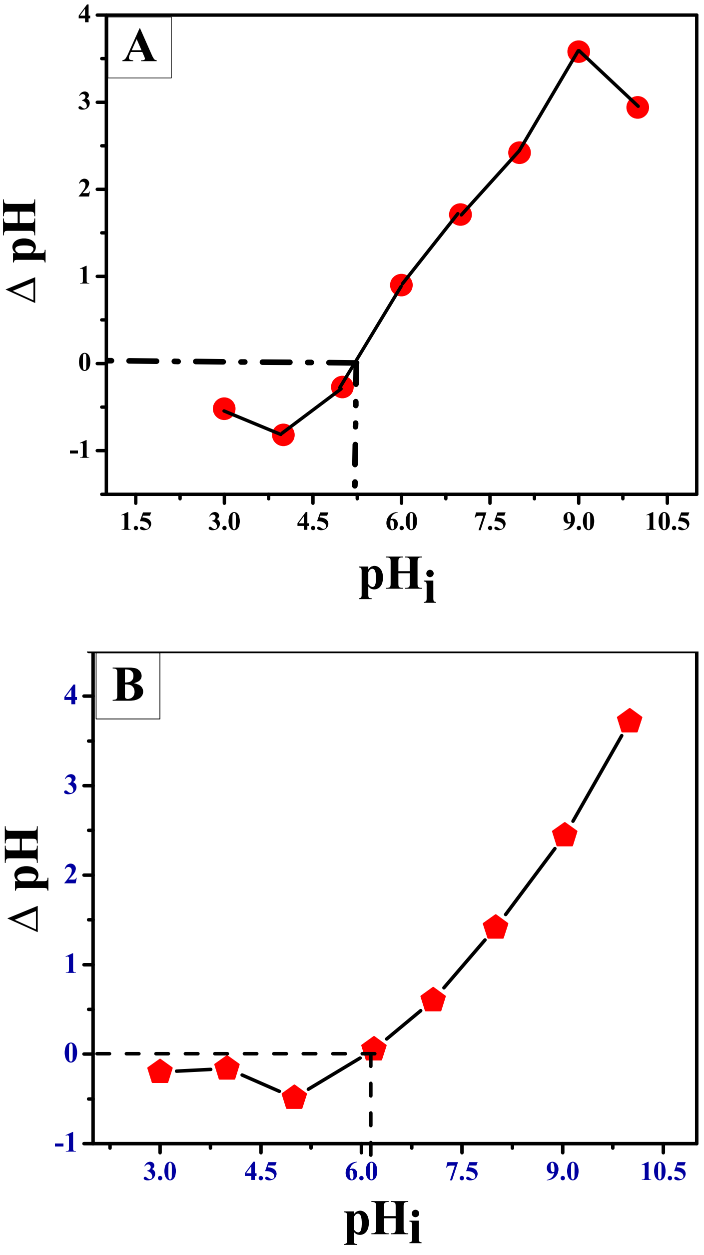

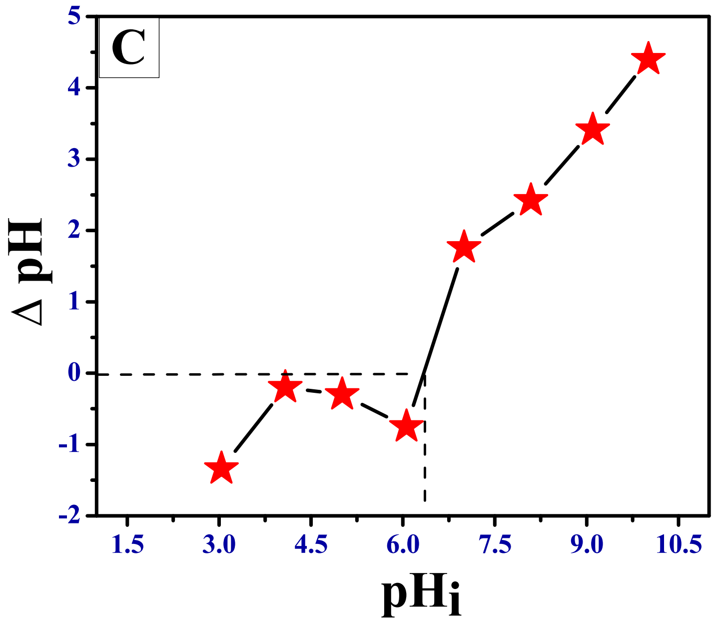

Fig. 3.42: (A)-(C) Plot of Δ pH versus pHᵢ for the estimation of pH_{ZPC} of the adsorbent CIHFO, GO-CIHFO and βC-CIHFO respectively.

Fluoride adsorption over each adsorbent hence can be happened by Ligand/anion exchange or by hydrogen bonding. Finally, it can be concluded that Fluoride adsorption over each adsorbent individually is a combination of hydrogen bonding, electrostatic interaction and also involved ligand exchange in between hydroxyl groups and fluoride ions (Mohan *et al.*, 2016).

3.6. Effect of Contact Time on Adsorption Process and Kinetic Modeling

The effect of contact time with variation of both initial fluoride concentration and temperature upon fluoride uptake capacity of proposed three adsorbents was studied sequentially to comprehend the pattern of adsorption mechanism of ongoing adsorption process. Primarily, rate of adsorption is vastly influenced by the available free active binding sites of proposed adsorbent and high concentration gradient of fluoride. The kinetic data (Q_t vs. t) for the present studied reactions of three adsorbents are shown in **Fig.3.43-3.48** including non-linear fits of data with pseudo-first order (PFO) **(Eq. 2.7)** and pseudo-second order (PSO) **(Eq. 2.10)** models.

For CIHFO, data revealed that more than 80% of the loaded fluoride transferred to the material surface from the solution in time t = 0 to 40 minutes, and rest 15-20% of the fluoride in solution needed longer time to transfer on the solid surface. The later slow solute transfer may be due to the Coulombic repulsion force and physical hindrance of fluoride already hosted over the solid surface from solution as well as decrease of the available solute concentration and adsorption sites of the adsorbent. Time-rate adsorption of CIHFO, on fluoride uptake at different temperature (293K, 303K and 313K) with fixed fluoride solution (10 mg.L^{-1}) also revealed that period of saturation remains unchanged irrespective of the rise of temperature in each adsorption study thus is independent of temperature variation also.

In case of GO-CIHFO and βC-CIHFO, variations of Q_t shown with the increase of contact time (t, min) (Fig.3.45-3.48) suggested a biphasic pattern with a rapid initial uptake up to 60 min, and then gradually ensured equilibrium around 120 min. Thereafter, no significant increase in adsorption capacity (Q_t) was noted. However, variations of Q_t versus t obtained at different temperatures show somewhat lower equilibrium time. The fast fluoride adsorption rate over GO-CIHFO and βC-CIHFO at the initial stage might be elucidated by increased availabilities of active binding sites of the adsorbent.

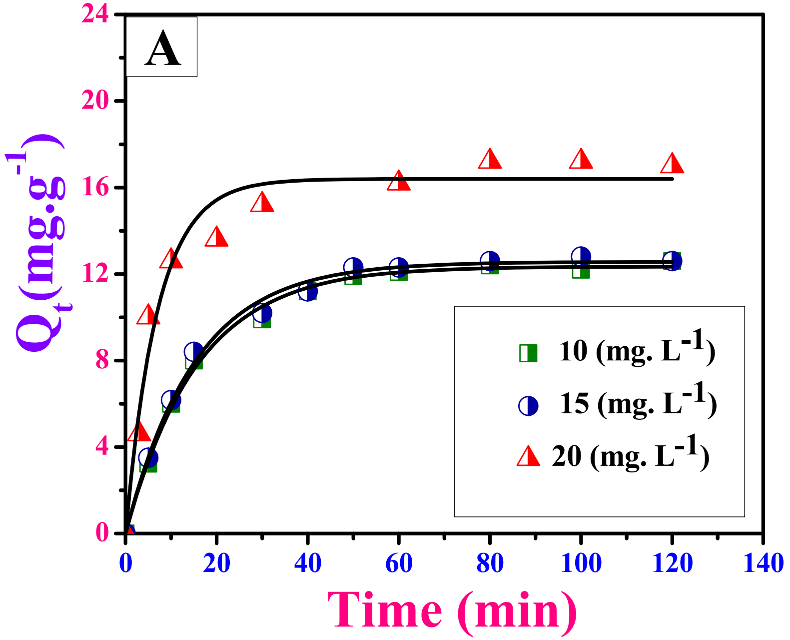

Fig. 3.43 (A): The plots of fluoride adsorption capacity of CIHFO at any time, Q_t (mg. g^{-1}) versus time, t (min) including non-linear pseudo first order (PFO) (—) at three different concentrations (10 mg.L^{-1}, 15 mg.L^{-1} and 20 mg.L^{-1}) at temperature 303K (ionic strength = 1M) at pH 7.0 (±0.2).

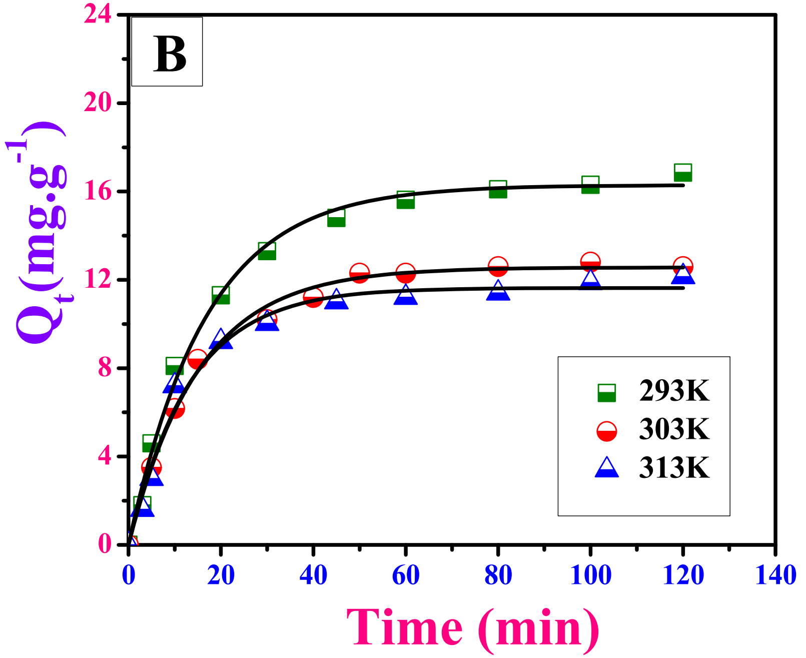

Fig. 3.43 (B): The plots of fluoride adsorption capacity of CIHFO at any time, Q_t (mg. g^{-1}) versus time, t (min) including non-linear pseudo first order (PFO) (—) at three temperature (293K, 303 K and 313 K) respectively with active fluoride concentration 10 mg.L^{-1} (ionic strength = 1M) at pH 7.0 (±0.2).

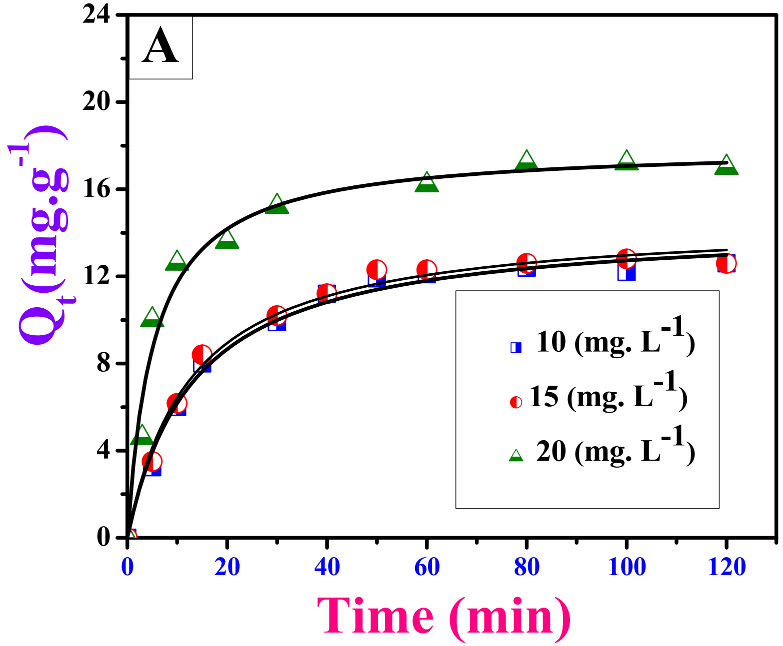

Fig. 3.44 (A): The plots of fluoride adsorption capacity of CIHFO at any time, Q_t (mg.g^{-1}) versus time, t (min) including non-linear pseudo second order (PSO) (—) at three different concentrations (10 mg.L^{-1}, 15 mg.L^{-1} and 20 mg.L^{-1}) at temperature 303K (ionic strength = 1M) at pH 7.0 (±0.2).

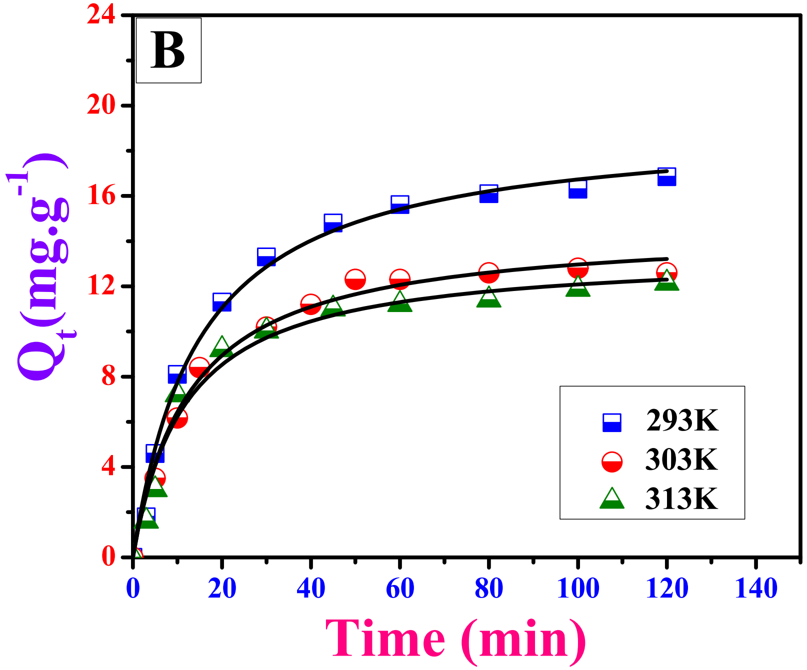

Fig. 3.44 (B): The plots of fluoride adsorption capacity of CIHFO at any time, Q_t (mg. g^{-1}) versus time, t (min) including non-linear pseudo second order (PSO) (—) at three temperature (293K, 303 K and 313 K) respectively with active fluoride concentration 10 mg.L^{-1} (ionic strength = 1M) at pH 7.0 (±0.2).

Often after reaching equilibrium, the remaining vacant active sites are difficult to occupy by fluoride ions because of active repulsive forces between the solute molecules on the solid and bulk phases. It was observed that in all experimental set up for adsorption study, saturation time (equilibrium time) is highly independent of initial concentration (C_i) of fluoride solution. The fluoride uptake capacity was found to be in sequentially rising trend with increase of initial fluoride concentration until the equilibrium time was achieved. (PFO) and (PSO) kinetics models (**Eq. 2.7 & 2.10**) are both ancient kinetic models knowingly applied to comprehend adsorption mechanism intricate in between proposed adsorbent and adsorbate respectively.

Some other kinetic models such as mass transfer (MT) (**Eq. 2.11**), intra-particles diffusion (IPD) **(Eq. 2.12-2.14**), Elovich (**Eq. 2.15-2.16**), Richenberg (**Eq.2.17-2.21)** as described in material and methods potion, are also act as decisive models on their own aspects as they help to evaluate the rate-controlling step (RCS) convoluted in ongoing adsorption mechanism have been applied to determine eventually involved in fluoride adsorption process over the developed three adsorbents.

3.6.1. Pseudo-First Order and Pseudo-Second Order Kinetics Models

The kinetic model fits of time dependent adsorption data are shown in **Fig.3.43-3.48** and different parameters assembled from modeling to the kinetic equations are given in **Table- 3.1A and Table- 3.1B**.Validation **of PFO and PSO** models with experimental data are thought to be curial as these two models express different aspects of adsorption process.

As per PFO model, the whole adsorption rate is directly proportional to the difference exist in-between the saturation concentration and the amount of solute uptake with time whereas PSO model assumes that chemisorption is controlling the adsorption rate by sharing or exchanging of electrons in between adsorbent and adsorbate.

Accentuating on the values of regression coefficient (R^2) **(Table- 3.1A & 3.1B)**, it can be said that the fluoride adsorption over surfaces of all three proposed absorbents has occurred almost in accordance of **PSO** model. There is no much difference observed in between the $Q_{t(exp)}$ and $Q_{t(model)}$ values from **PSO** model at any particular time and temperature and pH. As chemisorption is ubiquitous controlling factor when any adsorption kinetics is expressed by **PSO** model particularly; hence it can be assumed from such results that chemisorption might be involved in fluoride adsorption over these three adsorbents (Biswas *et al*., 2009; Mohan *et al*., 2016; Mukhopadhyay *et al*., 2017).

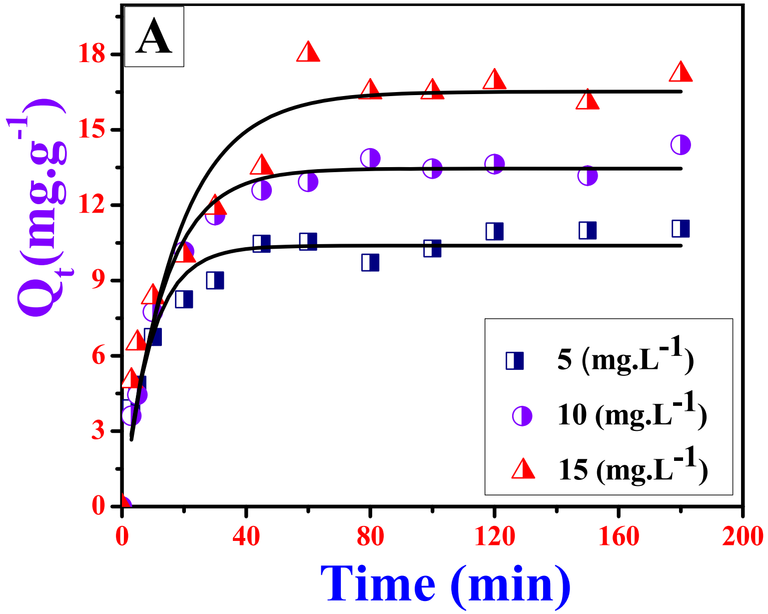

Fig. 3.45(A): The plots of fluoride adsorption capacity of GO-CIHFO at any time, Q_t (mg. g^{-1}) versus time, t (min) including non-linear pseudo first order (PFO) (—) at three different concentrations (5 mg.L^{-1}, 10 mg.L^{-1} and 15 mg.L^{-1}) at temperature 303K (ionic strength = 1M) at pH 7.0 (±0.2).

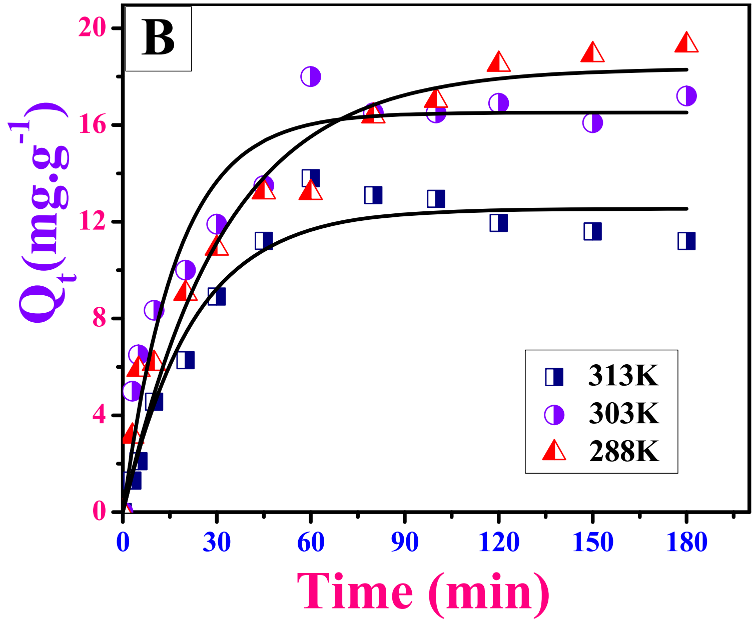

Fig. 3.45 (B): The plots of fluoride adsorption capacity of GO-CIHFO at any time, Q_t (mg. g^{-1}) versus time, t (min) including non-linear pseudo first order (PFO) (—) at three temperature (288K, 303 K and 313 K) respectively with active fluoride concentration 15 mg.L^{-1} (ionic strength = 1M) at pH 7.0 (±0.2).

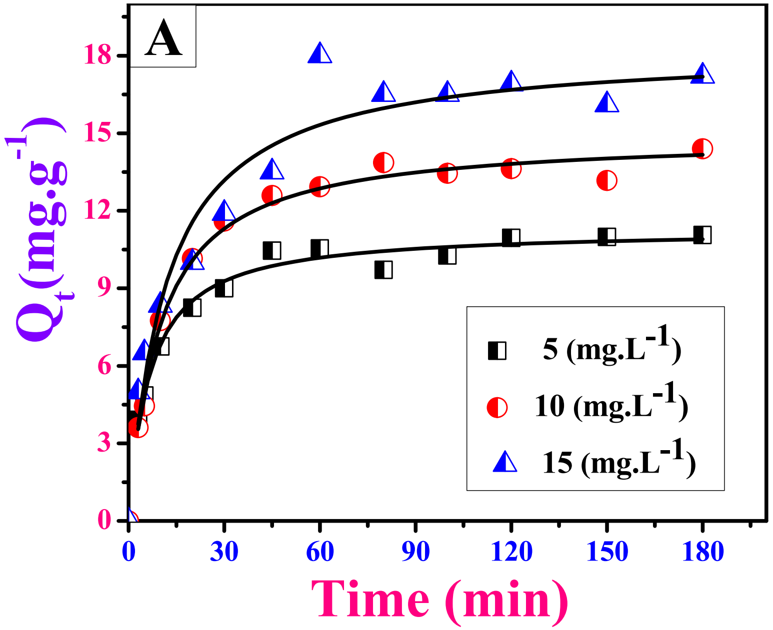

Fig. 3.46 (A): The plots of fluoride adsorption capacity of GO-CIHFO at any time, Q_t (mg.g^{-1}) versus time, t (min) including non-linear pseudo second order (PSO) (—) at three different concentrations (5 mg.L^{-1},10 mg.L^{-1} and 15 mg.L^{-1}) at temperature 303K (ionic strength = 1M) at pH 7.0 (±0.2).

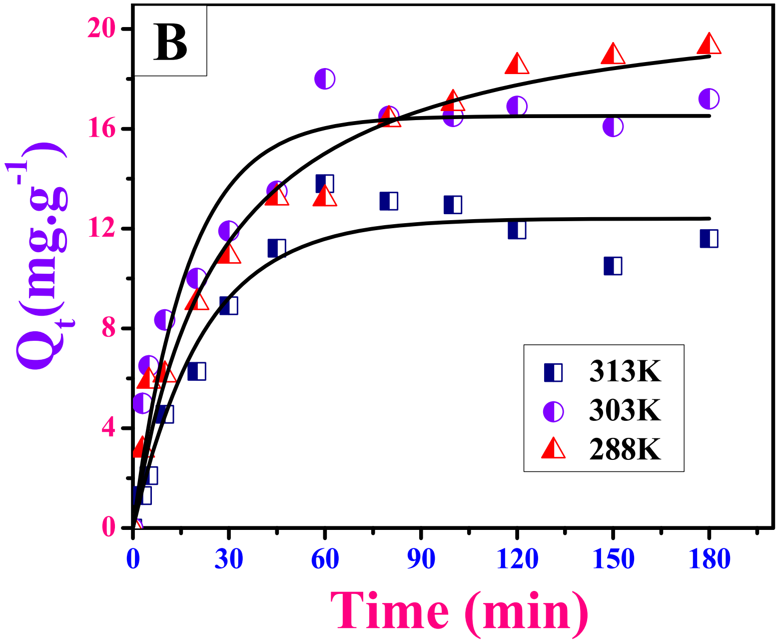

Fig. 3.46 (B): The plots of fluoride adsorption capacity of GO-CIHFO at any time, Q_t (mg. g^{-1}) versus time, t (min) including non-linear pseudo second order (PSO) (—) at three temperature (288K, 303K and 313 K) respectively with active fluoride concentration 15 mg.L^{-1} (ionic strength = 1M) at pH 7.0 (±0.2).

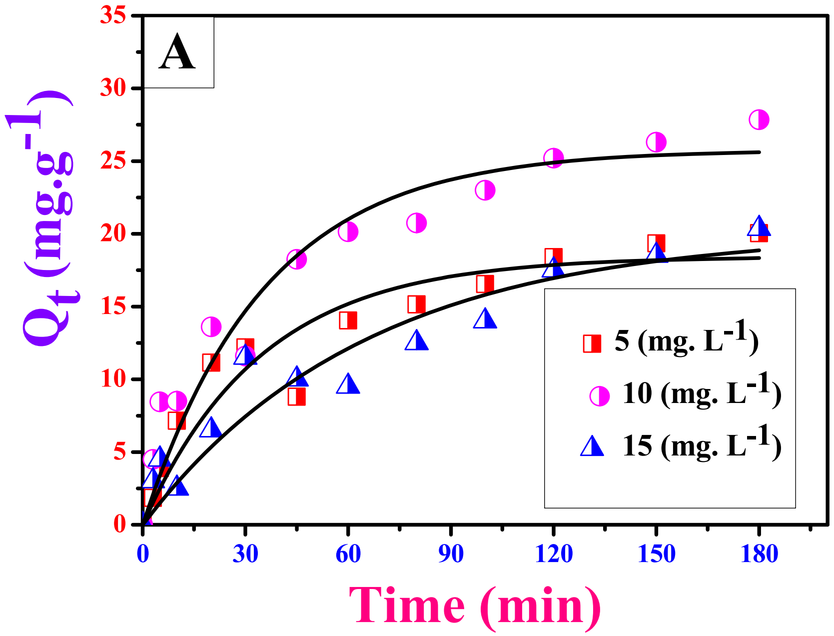

Fig. 3.47 (A): The plots of fluoride adsorption capacity of βC-CIHFO at any time, Q_t (mg.g^{-1}) versus time, t (min) including non-linear pseudo first order (PFO) (—) at three different concentrations (5 mg.L^{-1}, 10 mg.L^{-1} and 15 mg.L^{-1}) at temperature 303K (ionic strength = 1M) at pH 7.0 (±0.2).

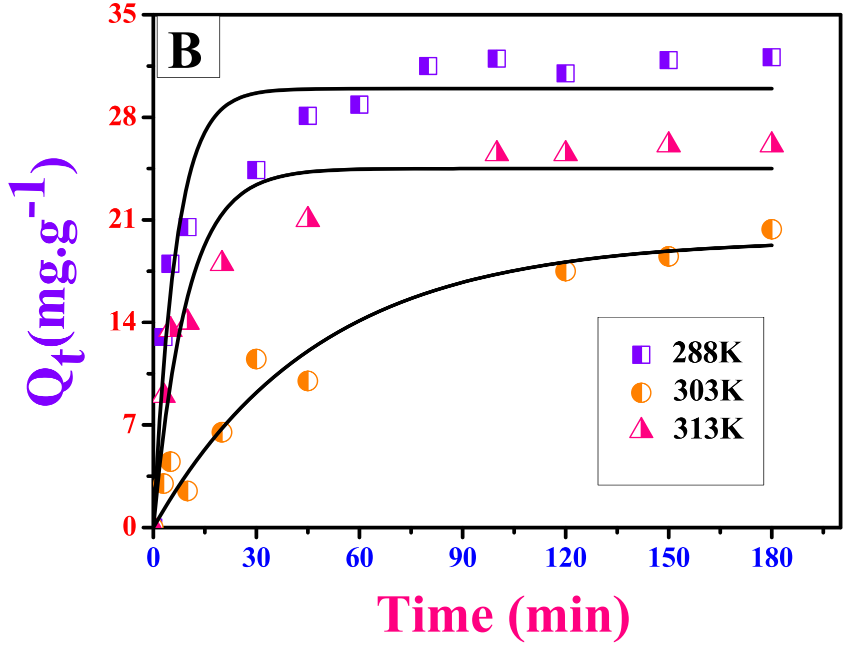

Fig. 3.47 (B): The plots of fluoride adsorption capacity of βC-CIHFO at any time, Q_t (mg.g^{-1}) versus time, t (min) including non-linear pseudo first order (PFO)(—) at three temperature (288K, 303K and 313K) respectively with active fluoride concentration 15 mg.L^{-1} (ionic strength = 1M) at pH 7.0 (±0.2).

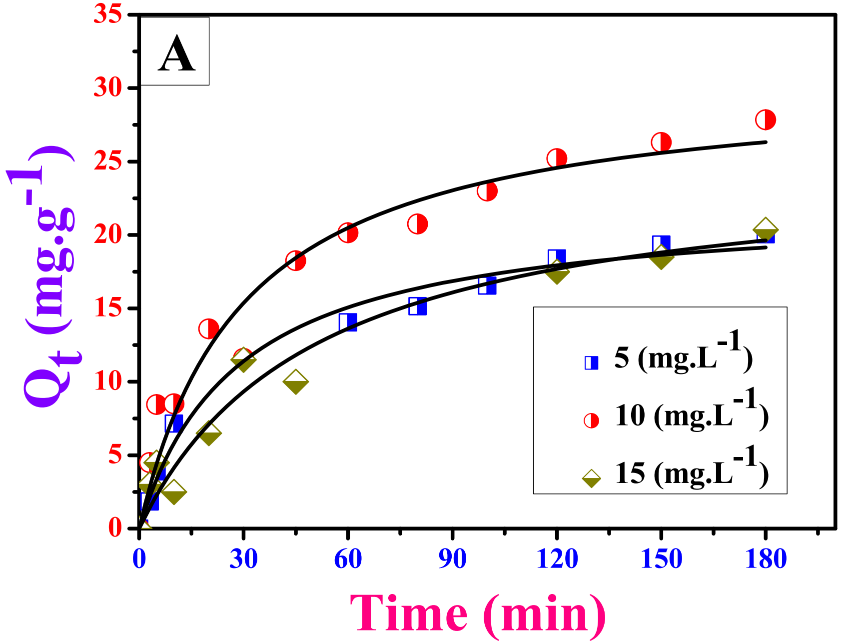

Fig. 3.48 (A): The plots of fluoride adsorption capacity of βC-CIHFO at any time, Q_t (mg. g^{-1}) versus time, t (min) including non-linear pseudo second order (PSO) (—) at three different concentrations (5 mg.L^{-1}, 10 mg.L^{-1} and 15 mg.L^{-1}) at temperature 303K (ionic strength = 1M) at pH 7.0 (±0.2).

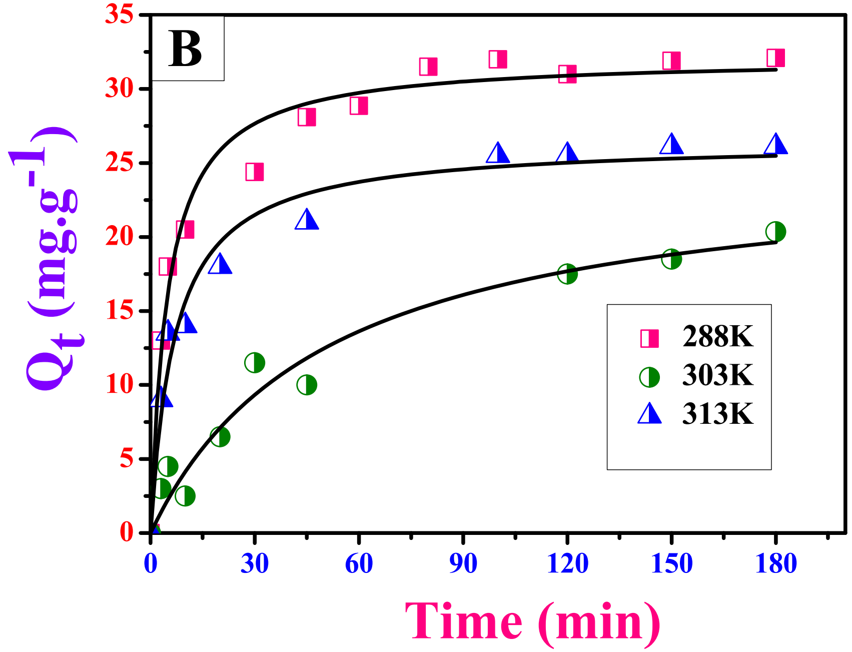

Fig. 3.48 (B): The plots of fluoride adsorption capacity of βC-CIHFO at any time, Q_t (mg. g^{-1}) versus time, t (min) including non-linear pseudo second order (PSO) (—) at three temperature (288K,303K and 313K) respectively with active fluoride concentration 15 mg.L^{-1} (ionic strength = 1M) at pH 7.0 (±0.2).

Table 3.1A: Estimated kinetic parameters of Pseudo-first order (PFO) and Pseudo-second order (PSO) kinetic models for fluoride adsorption reactions with CIHFO, GO-CIHFO and βC-CIHFO at different concentration of Fluoride with solution pH 7.0 and at temperature 303K.

Kinetics Equation	**Parameters**	**βC-CIHFO**			**GO-CIHFO**			**CIHFO**		
		Fluoride concentration (mg. L^{-1})			**Fluoride concentration (mg. L^{-1})**			**Fluoride concentration (mg. L^{-1})**		
		5	**10**	**15**	**5**	**10**	**15**	**10**	**15**	**20**
Pseudo-first order	**k_1 (min^{-1})**	0.028	0.028	0.015	0.10	0.077	0.058	0.06	0.10	0.14
	Q_t (mg g^{-1})	18.43	25.78	20.12	10.38	13.45	16.51	12.34	14.70	16.3
	R^2	0.89	0.92	0.89	0.92	0.98	0.93	0.99	0.99	0.96
	χ^2	4.55	5.971	4.30	0.484	0.270	2.270	0.08	0.27	1.24
Pseudo-second order	**k_2 (g mg^{-1} min^{-1})**	0.001	0.001	0.007	0.013	0.006	0.002	0.005	0.007	0.010
	Q_t(mg g^{-1})	22.15	30.69	25.19	11.29	14.91	18.30	14.40	16.37	17.98
	R^2	0.98	0.95	0.95	0.977	0.99	0.95	0.99	0.99	0.97
	χ^2	0.85	3.83	2.40	0.151	0.161	1.45	0.17	0.31	0.82

Table 3.1B: Estimated kinetic parameters of Pseudo-first order(PFO) and Pseudo-second order (PSO) models for fluoride adsorption reactions with CIHFO (Fluoride concentration -10 mg.L^{-1}), GO-CIHFO and βC-CIHFO at different at different temperature (Fluoride concentration -15mg.L^{-1}) with solution pH 7.0.

Kinetics Equation	**Parameters**	**βC-CIHFO**			**GO-CIHFO**			**CIHFO**		
		Temperature (K)			**Temperature (K)**			**Temperature (K)**		
		288	**303**	**313**	**288**	**303**	**313**	**293**	**303**	**313**
Pseudo-First order	**k_1 (min^{-1})**	0.153	0.015	0.103	0.0311	0.058	0.044	0.05	0.06	0.07
	Q_t (mg g^{-1})	29.95	20.12	24.50	18.35	16.51	12.53	16.28	12.56	11.63
	R^2	0.93	0.89	0.91	0.95	0.93	0.96	0.99	0.99	0.986
	χ^2	6.48	4.30	6.45	2.06	2.27	0.93	0.23	0.11	0.30
Pseudo-second order	**k_2 (g mg^{-1} min^{-1})**	0.006	0.007	0.005	0.001	0.002	0.003	0.003	0.005	0.006
	Q_t(mg g^{-1})	32.14	25.19	26.46	21.71	18.30	14.51	19.20	14.61	13.48
	R^2	0.97	0.95	0.97	0.97	0.95	0.93	0.99	0.99	0.97
	χ^2	2.14	2.40	2.22	1.07	1.45	1.793	0.32	0.17	0.47

3.6.2. Mass Transfer Study

The Mckay *et al.* **(Eq. 2.11**) model plot for the **MT** of fluoride upon CIHFO, GO-CIHFO and βC-CIHFO in neutral pH can be demonstrated well along with **Fig.3.49, Fig.3.50 and Fig.3.51** respectively and values are given in **Table- 3.2B**. Generally few steps such as movement of pollutant from bulk solution to the upper boundary of adsorbent, followed by diffusion of adsorbate from boundary film layer to the surface of adsorbent and finally adhesion of adsorbate into the internal pore and spaces in between of active sites of adsorbent as well as sequential adsorption and desorption of the adsorbate at the active sites of the adsorbent surface are defined the **MT** phenomenon gradually. Good linear fitting of experimental data assume that external **MT** step might be present during the adsorption process. The values determined by the slopes of the plots of ln $[C_t/C_i - 1/(1 + mk)]$ vs. t (min) at different temperature (288K or 293K, 303K and 313K) with fixed fluoride concentration (15 $mg.L^{-1}$ for GO-CIHFO and βC-CIHFO and 10 $mg.L^{-1}$ for CIHFO) with solution pH 7.0 with good linear fitting meant that the **MT** coefficients (β_1) for the diffusion of fluoride from liquid film boundary to the surface of all three adsorbents exist. All the values of **MT** coefficient (**Table- 3.2B**) are act as an indication of sufficiently rapid transfer of adsorbate species from bulk to the surface or interface for in neutral pH.

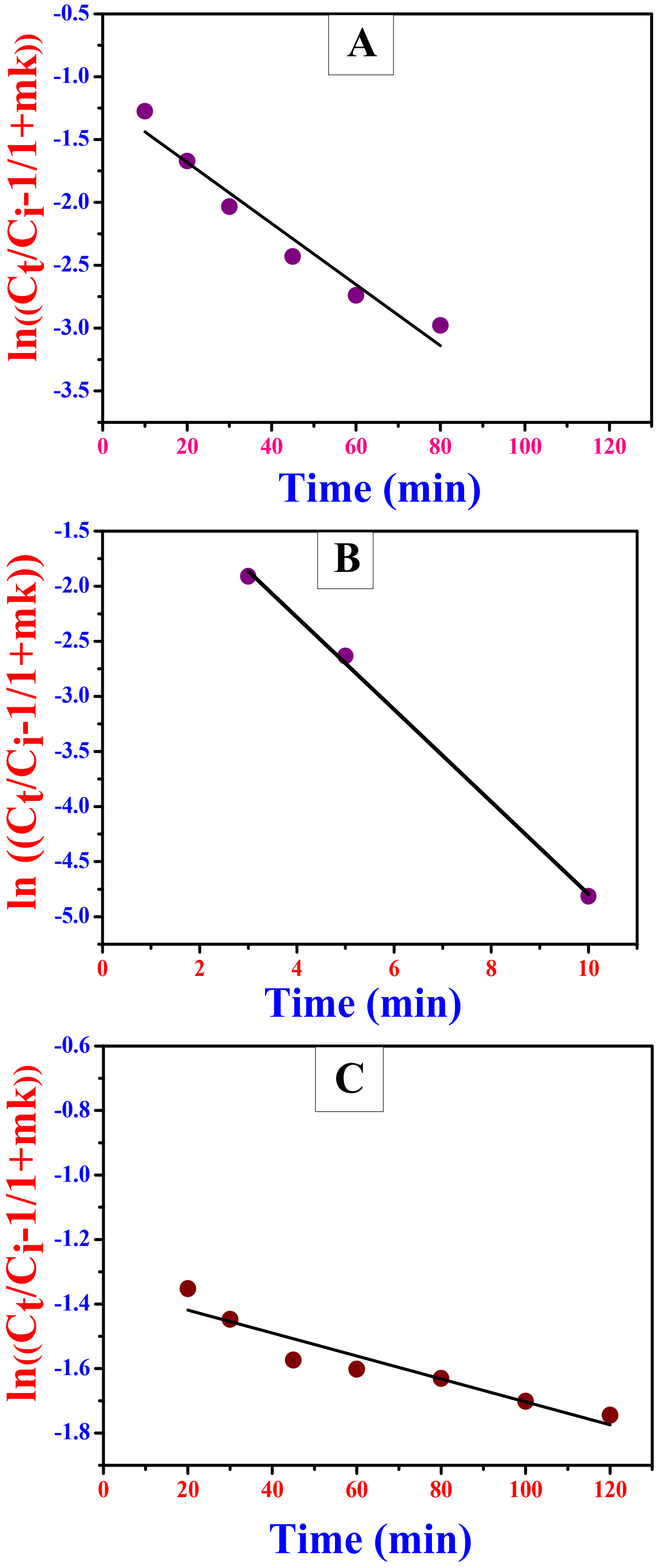

Fig. 3.49: (A)-(C) depicting mass transfer process for adsorbent CIHFO at three different temperature (293 K, 303 K and 313 K) with active fluoride concentration 10 mg.L^{-1} (ionic strength = 1M) and at pH 7.0 (±0.2).

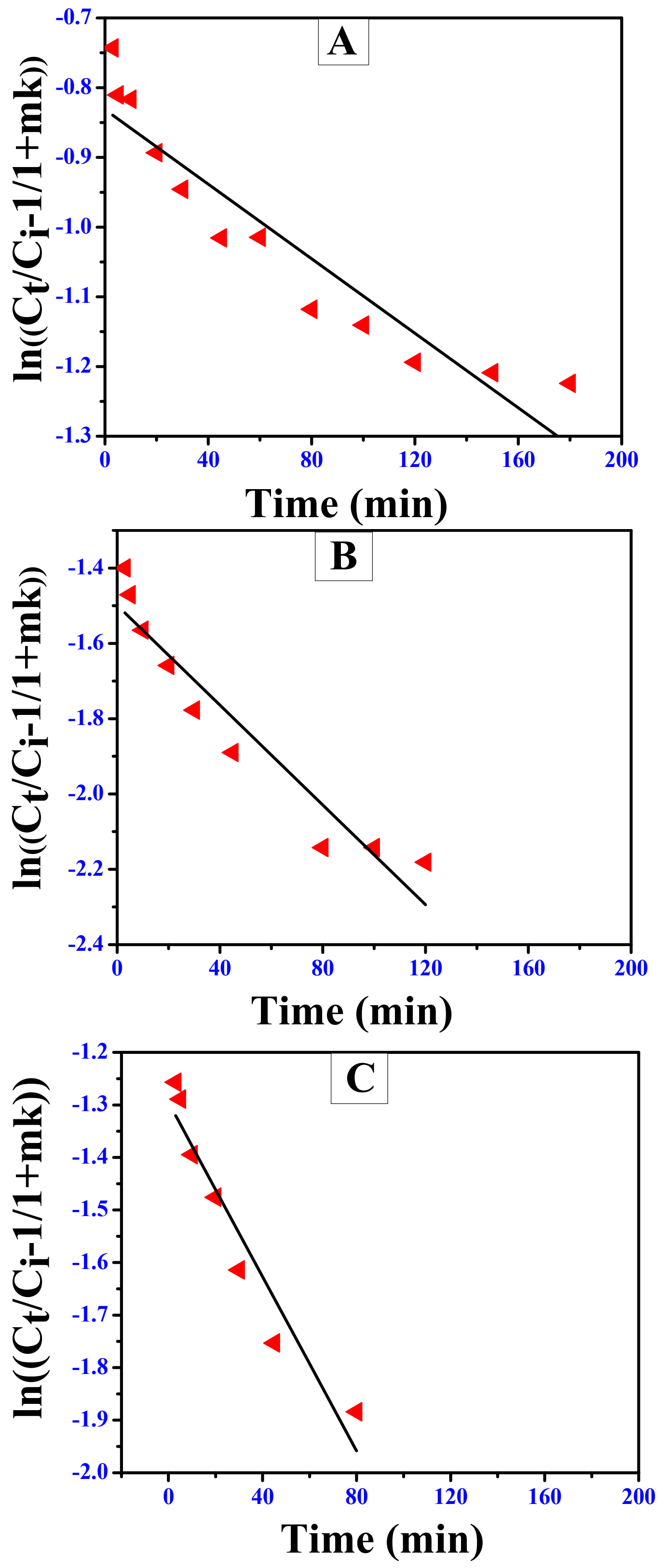

Fig. 3.50: **(A)-(C)** depicting mass transfer process for adsorbent GO-CIHFO at three different temperature (288 K, 303 K and 313 K) with active fluoride concentration 15 mg.L^{-1} (ionic strength = 1M) and at pH 7.0 (±0.2).

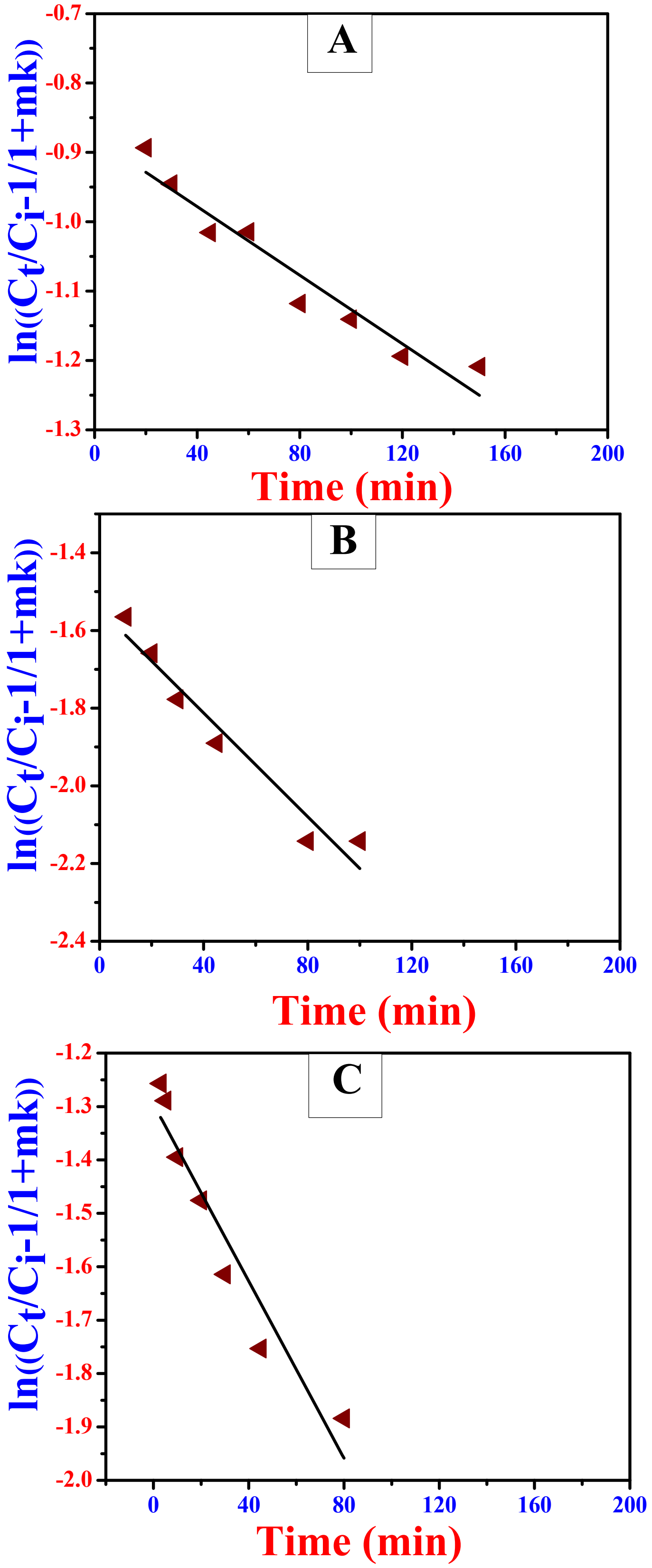

Fig. 3.51: (A)-(C) depicting mass transfer process for adsorbent βC-CIHFO at three different temperature (288 K, 303 K and 313 K) with active fluoride concentration 15 mg.L^{-1} (ionic strength = 1M) and at pH 7. 0 (±0.2).

3.6.3. Intra-particle Diffusion Model

Weber–Morris model **(Eq. 2.12)** is the most widely accepted model to evaluate the prospect of **Intra-particle diffusion** (**IPD)** on any adsorption process. As per this model, if the plot of Q_t vs. $t^{0.5}$ is a straight line and passes through the origin, then the **IPD** is merely the rate controlling step (RCS) but if reverse condition is prevailing when these plots are linear but did not pass through origin meant RCS is not solely the **IPD** (Biswas *et al.*, 2009; Ranjan *et al.*, 2009). The plot of Q_t vs. t $^{0.5}$(min) as shown in **Fig.3.52-3.57** signify the corresponding Weber–Morris model to evaluate the prospect of intraparticle diffusion on the adsorption process of fluoride onto CIHFO, GO-CIHFO and βC-CIHFO. The plots were found to be significantly linear with high value of R^2, and K_{id} values have been determined by their respective slopes at varied experimental conditions **(Table 3.2A and 3.2B)**. It can be assumed that fluoride adsorption over proposed three adsorbents occurred via a complex mechanism involving both external mass transfer and intraparticle diffusion as the rate determining step.

This observation was further strengthened by the value of the intraparticle diffusion coefficient (D), which can be calculated by the equation 2.13.Here, r (cm) represents for the average radius of the adsorbent particle and $t^{0.5}$ (min) is the time required for half of the adsorption. If the D value is in the range of 10^{-11} (cm^2 s^{-1}) then intraparticle diffusion is the only rate determining step. In the present adsorption system, the value of D obtained for CIHFO; GO-CIHFO and βC-CIHFO in range of 3.25×10^{-6} ;7.46×10^{-8} cm^2 s^{-1}; 7.59×10^{-7} cm^2 s^{-1} that was in the order of 10^{-6}-10^{-8}, designating that intraparticle diffusion was not the only rate controlling step.

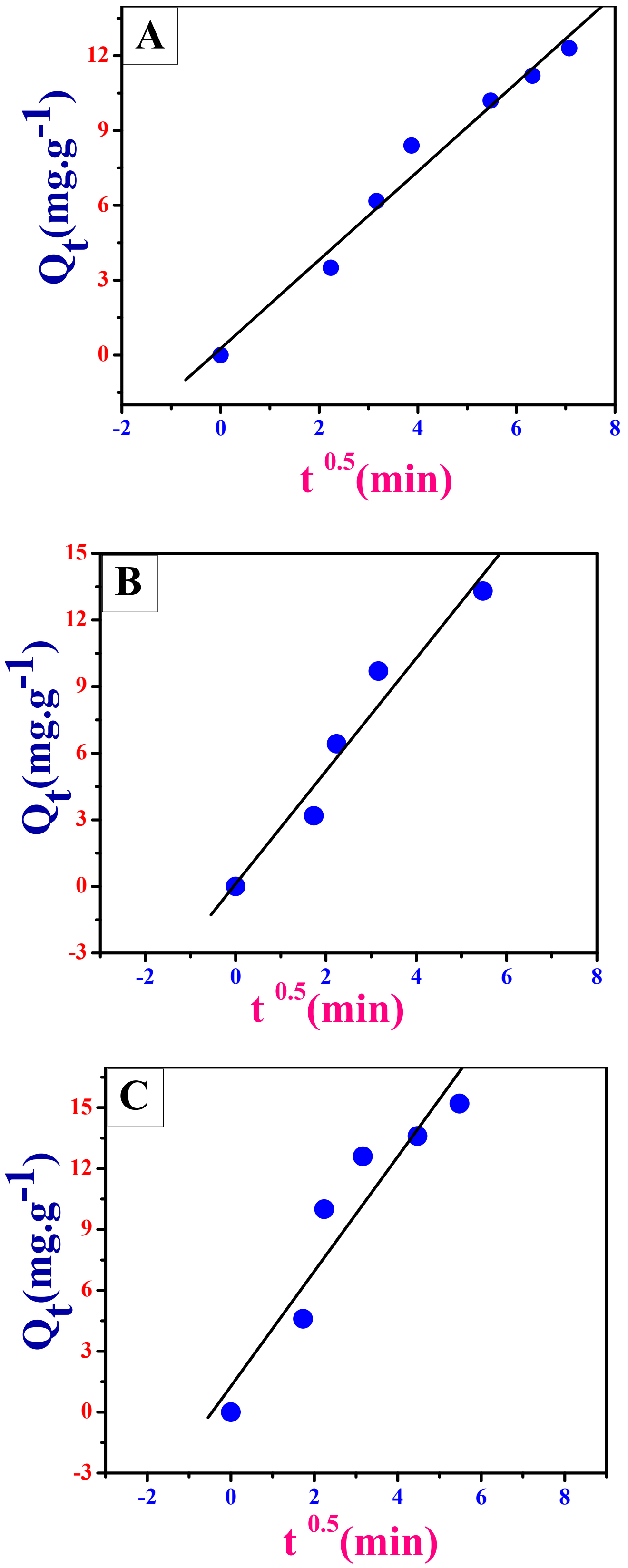

Fig. 3.52: (A)-(C) represent intra particle diffusion model for fluoride adsorption reactions with CIHFO at different concentration of Fluoride (10 mg.L^{-1}, 15 mg.L^{-1} and 20 mg.L^{-1}) at temperature 303K (ionic strength = 1M) at pH 7.0 (±0.2).

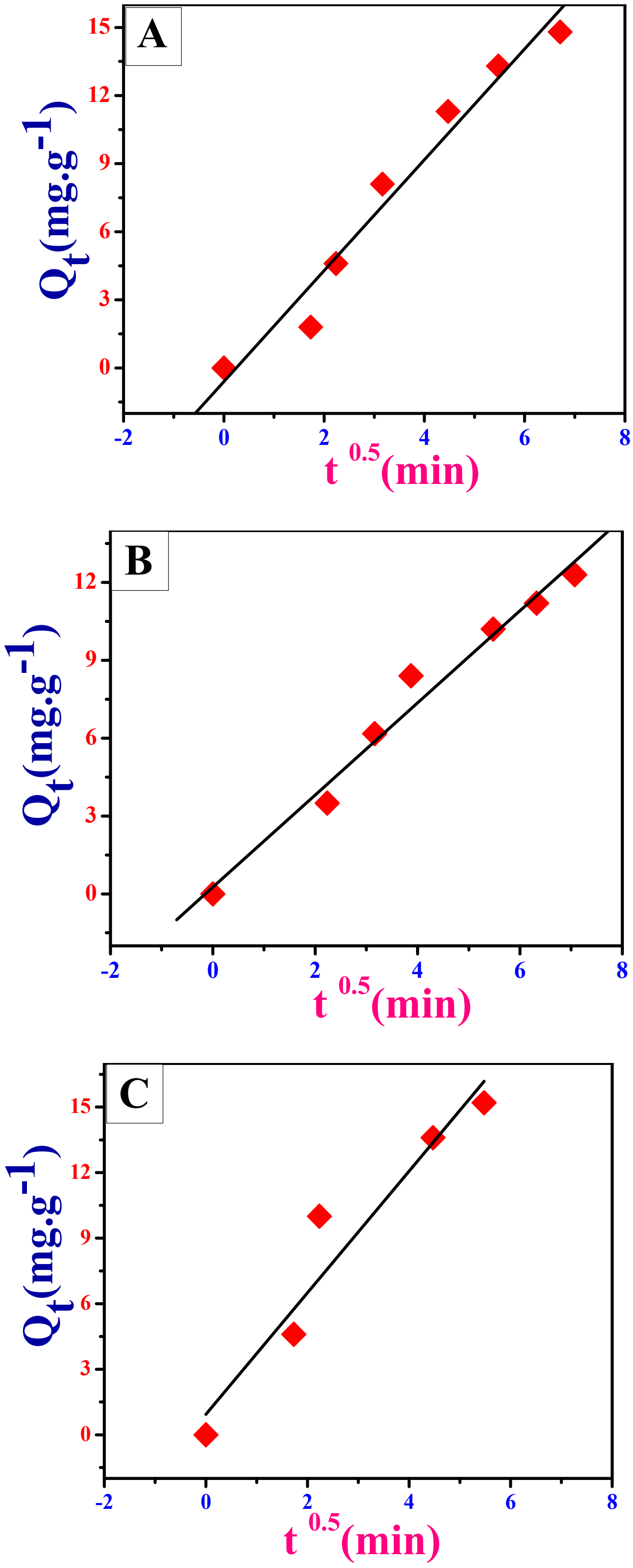

Fig. 3.53:(A)-(C) Represent Intra-particle diffusion model for fluoride adsorption reactions of CIHFO at three temperature (293K, 303 K and 313 K) respectively with active fluoride concentration 10 mg.L^{-1} (ionic strength = 1M) at pH 7.0 (±0.2).

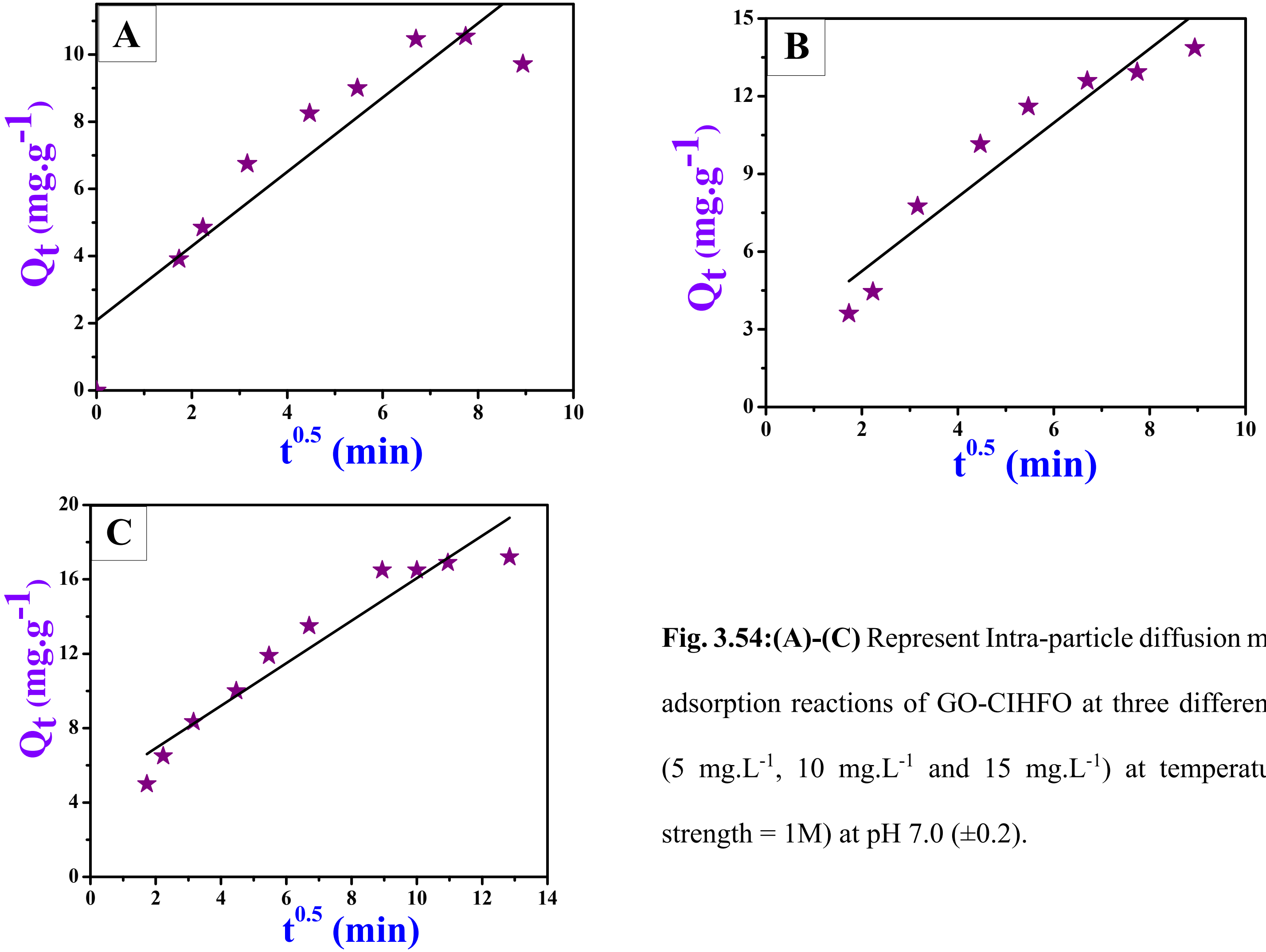

Fig. 3.54:(A)-(C) Represent Intra-particle diffusion model for fluoride adsorption reactions of GO-CIHFO at three different concentrations (5 mg.L^{-1}, 10 mg.L^{-1} and 15 mg.L^{-1}) at temperature 303K (ionic strength = 1M) at pH 7.0 (±0.2).

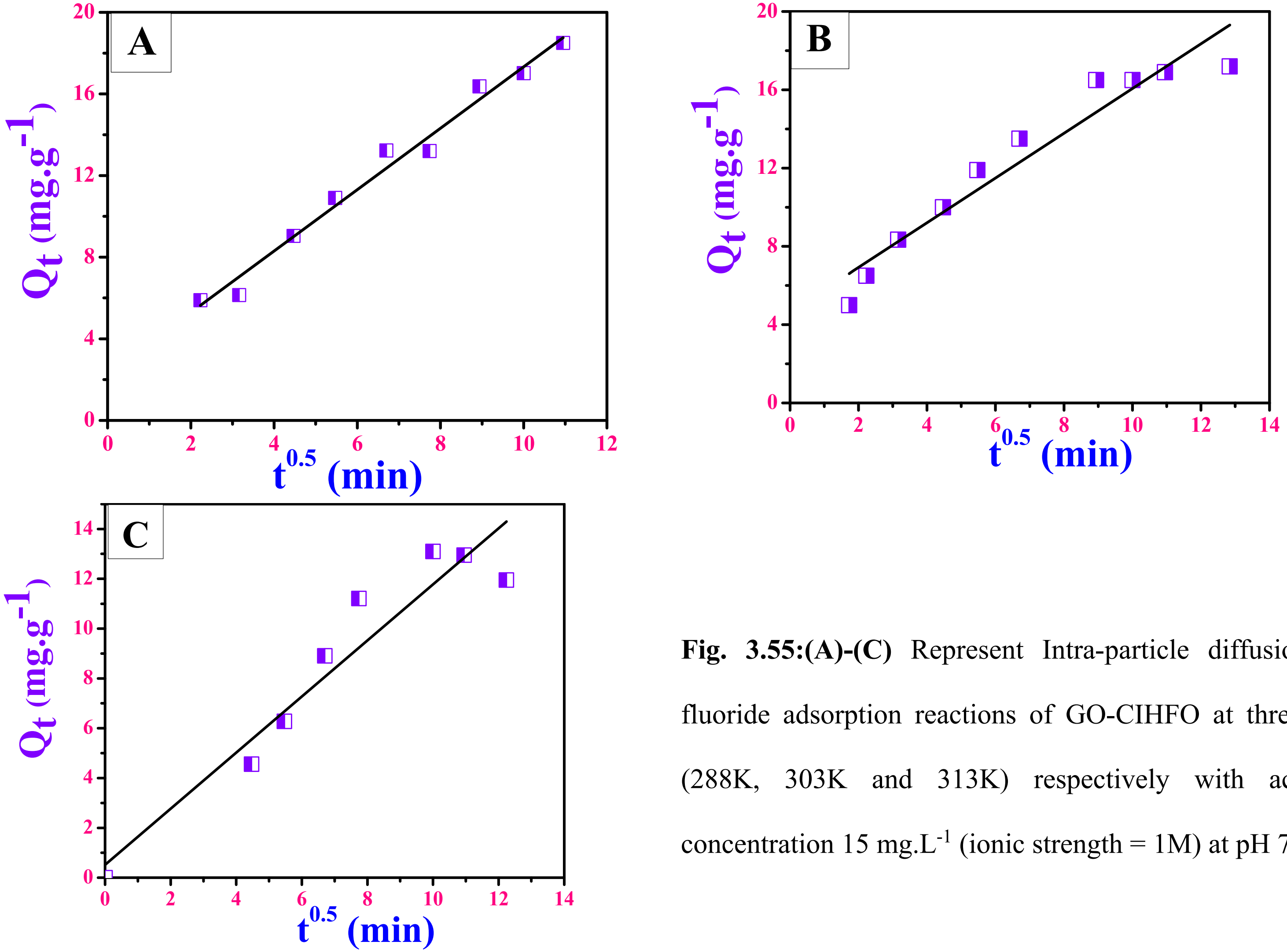

Fig. 3.55:(A)-(C) Represent Intra-particle diffusion model for fluoride adsorption reactions of GO-CIHFO at three temperature (288K, 303K and 313K) respectively with active fluoride concentration 15 mg.L^{-1} (ionic strength = 1M) at pH 7.0 (±0.2).

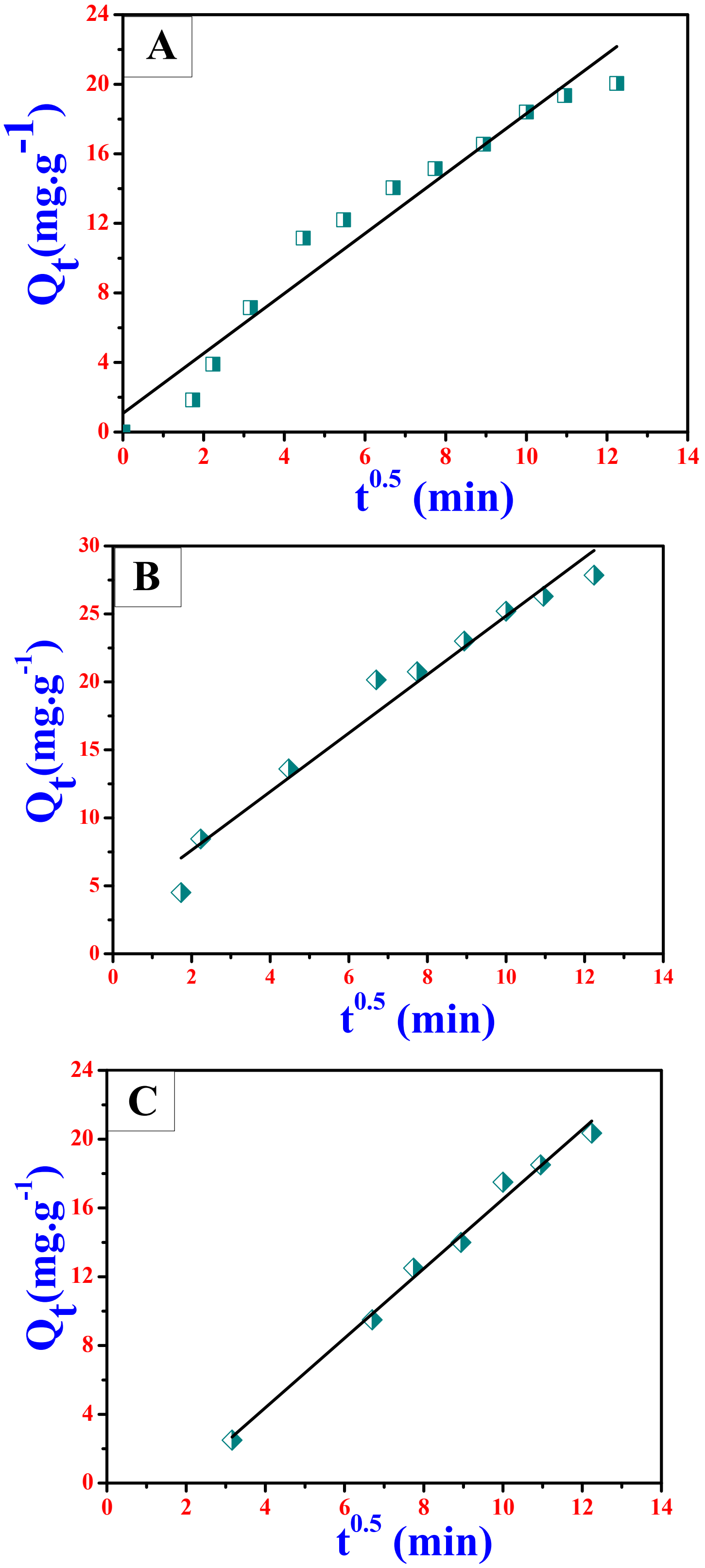

Fig. 3.56: (A)-(C) Represent Intra-particle diffusion model for fluoride adsorption reactions with βC-CIHFO at three different concentrations (5 mg.L^{-1}, 10 mg.L^{-1} and 15 mg.L^{-1}) at temperature 303K (ionic strength = 1M) at pH 7.0 (±0.2).

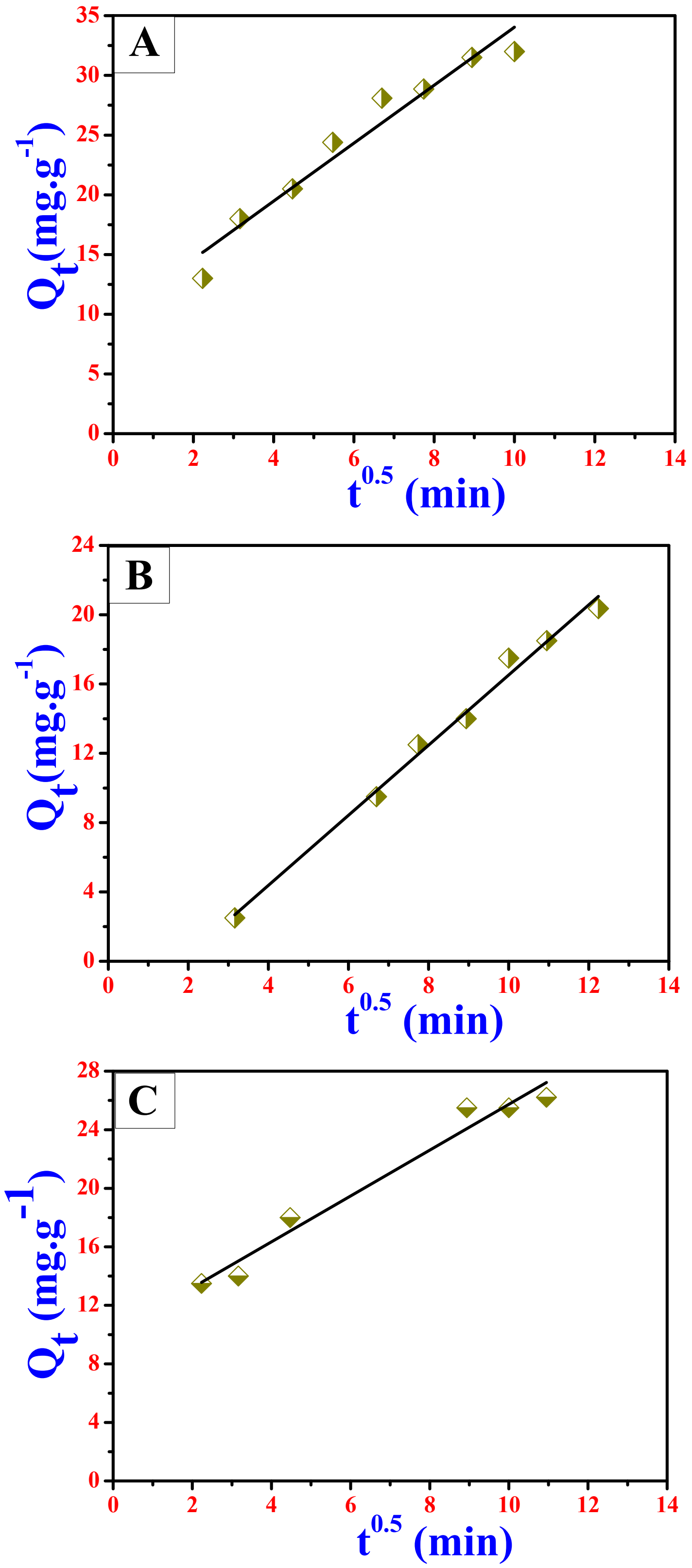

Fig. 3.57: (A)-(C) Represent Intra-particle diffusion model for fluoride adsorption reactions with βC-CIHFO at three temperature (288K, 303K and 313K) respectively with active fluoride concentration 15 mg.L^{-1} (ionic strength = 1M) at pH 7.0 (±0.2).

3.6.4. Elovich Model

Elovich model is another widely accepted kinetic model used successfully to describe second order kinetics with a postulation that solid surface of adsorbent are energetically heterogeneous. It has been broadly accepted that chemisorption process can be elucidated by its linear form of semi-empirical equation (**Eq. 2.16**).The Elovich coefficients have been assumed from the plots Q_t vs. ln(t)(min). The initial adsorption rate, **'a'**, and desorption constant, **'b'**, were calculated from the slope and intercept of the straight-line plots and values obtained from plots have been tabularized in **Table 3.2A and 3.2B**.

It has been observed that applicability of the simple Elovich equation for the present kinetic data indicates that the Elovich equation was able to describe properly the kinetics of fluoride adsorption on CIHFO, GO-CIHFO and βC-CIHFO **(Fig.3.58-3.63)**. In neutral solution pH, the value of **'a'** and **'b'** varied as a function of both solution concentration and solution temperature. Good correlation coefficient (R^2) for both concentration variation and temperature variation implied that adsorption kinetics followed by pseudo-second order kinetic model based on assumption that chemisorption may be the rate determining step involving ion exchange in between adsorbent and adsorbate (Ranjan *et al*., 2009).

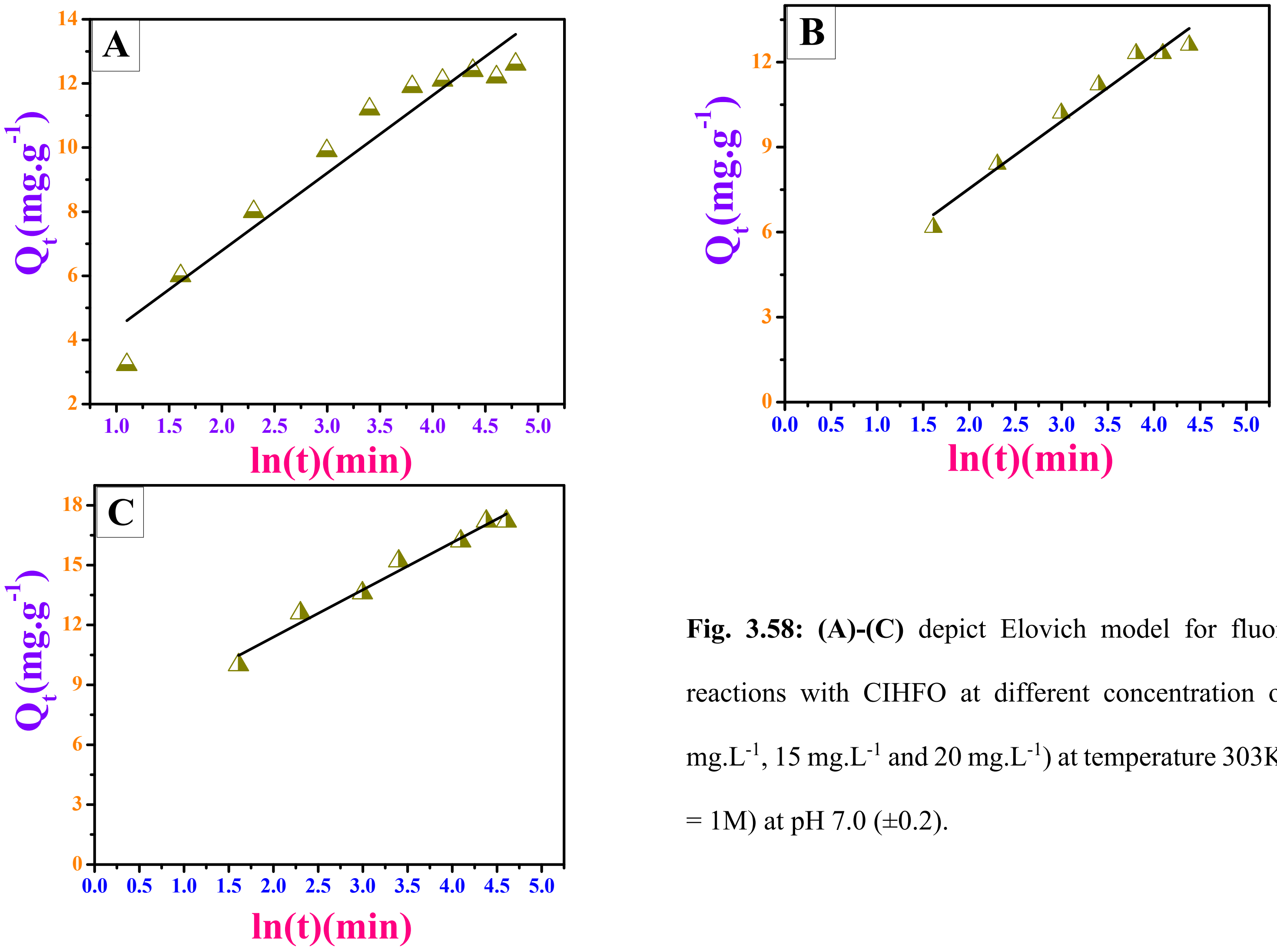

Fig. 3.58: (A)-(C) depict Elovich model for fluoride adsorption reactions with CIHFO at different concentration of Fluoride (10 mg.L^{-1}, 15 mg.L^{-1} and 20 mg.L^{-1}) at temperature 303K (ionic strength = 1M) at pH 7.0 (±0.2).

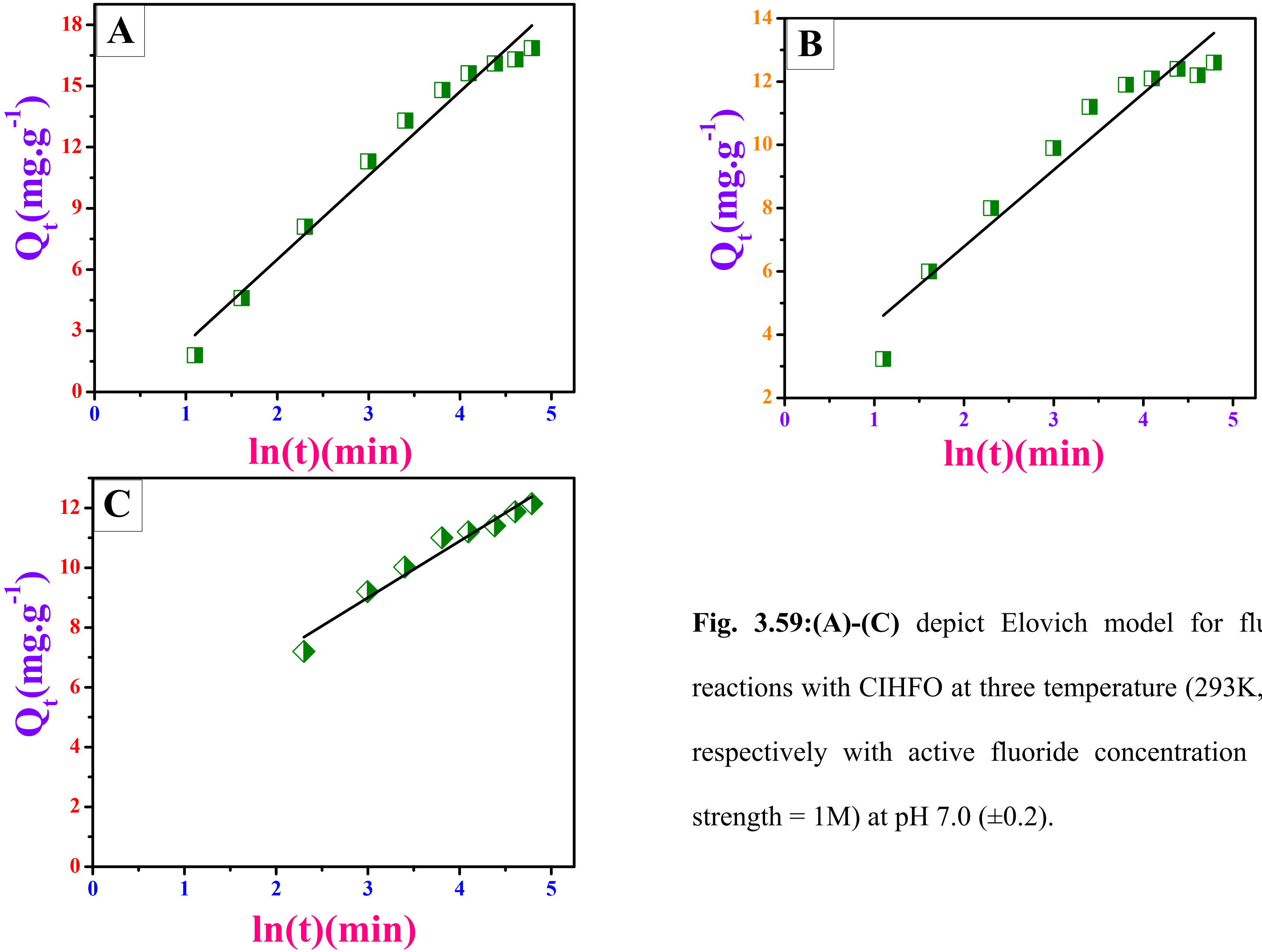

Fig. 3.59:(A)-(C) depict Elovich model for fluoride adsorption reactions with CIHFO at three temperature (293K, 303K and 313K) respectively with active fluoride concentration 10 mg.L^{-1} (ionic strength = 1M) at pH 7.0 (±0.2).

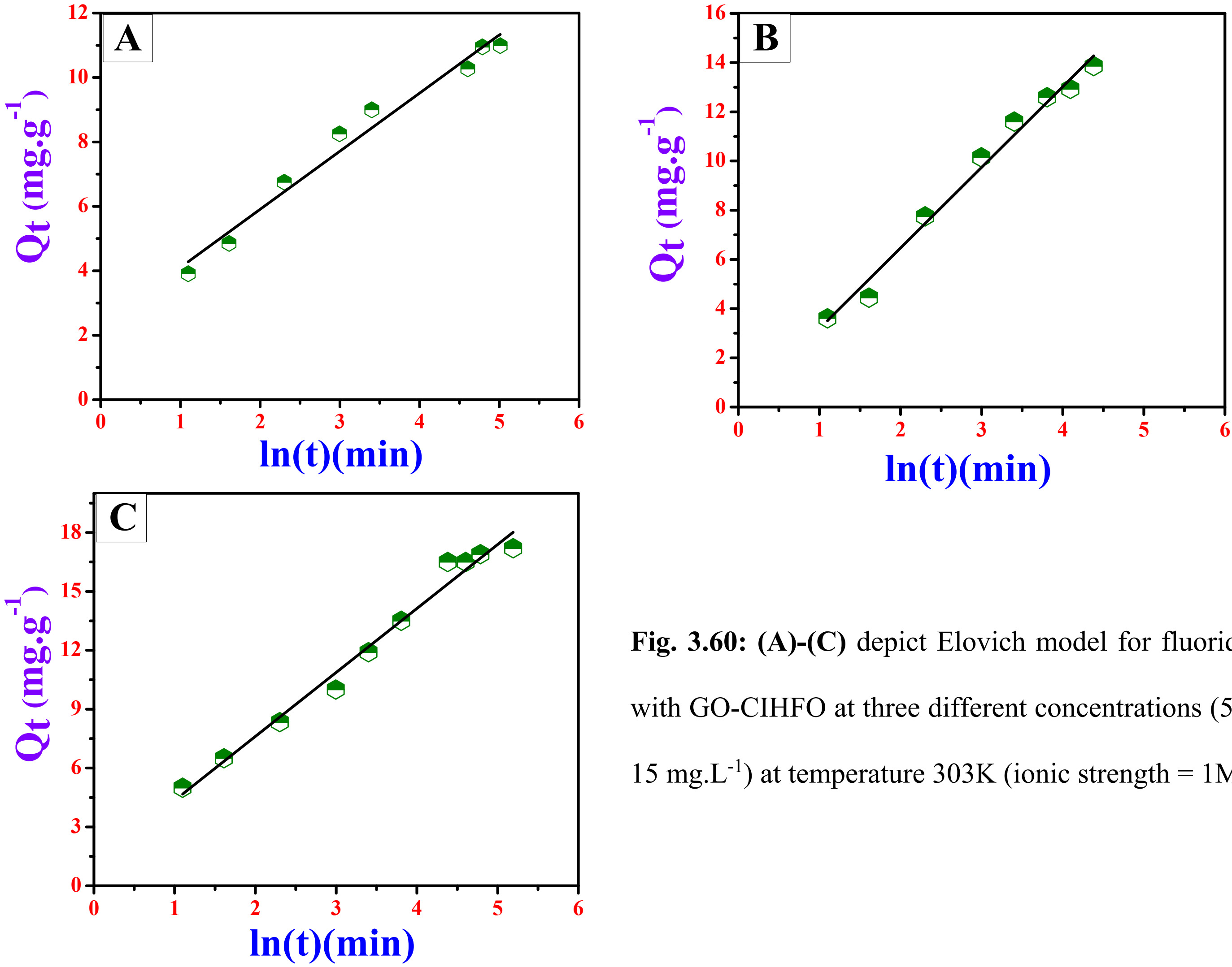

Fig. 3.60: (A)-(C) depict Elovich model for fluoride adsorption reactions with GO-CIHFO at three different concentrations (5 mg.L^{-1}, 10 mg.L^{-1} and 15 mg.L^{-1}) at temperature 303K (ionic strength = 1M) at pH 7.0 (±0.2).

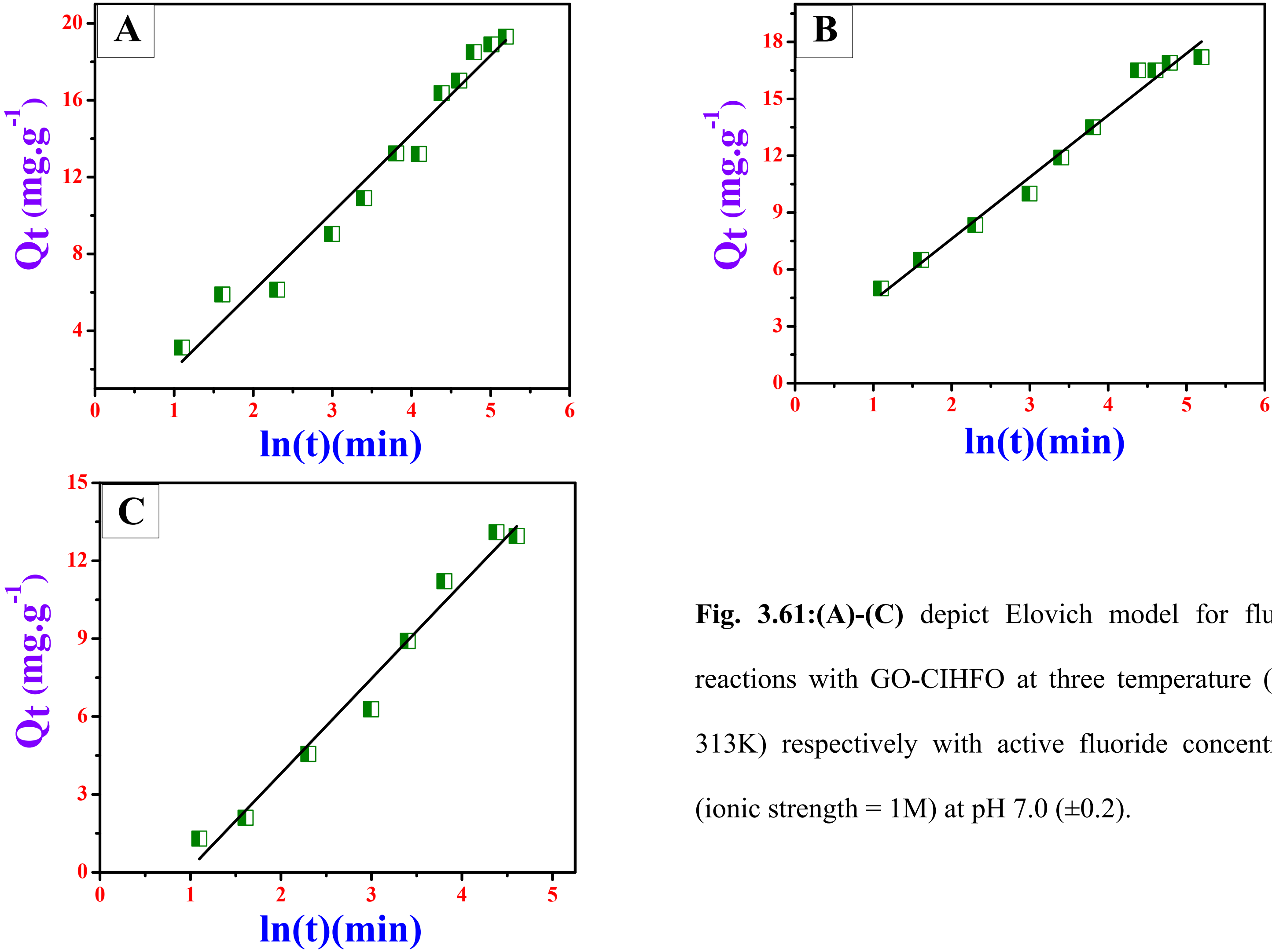

Fig. 3.61:(A)-(C) depict Elovich model for fluoride adsorption reactions with GO-CIHFO at three temperature (288K, 303K and 313K) respectively with active fluoride concentration 15 mg.L^{-1} (ionic strength = 1M) at pH 7.0 (±0.2).

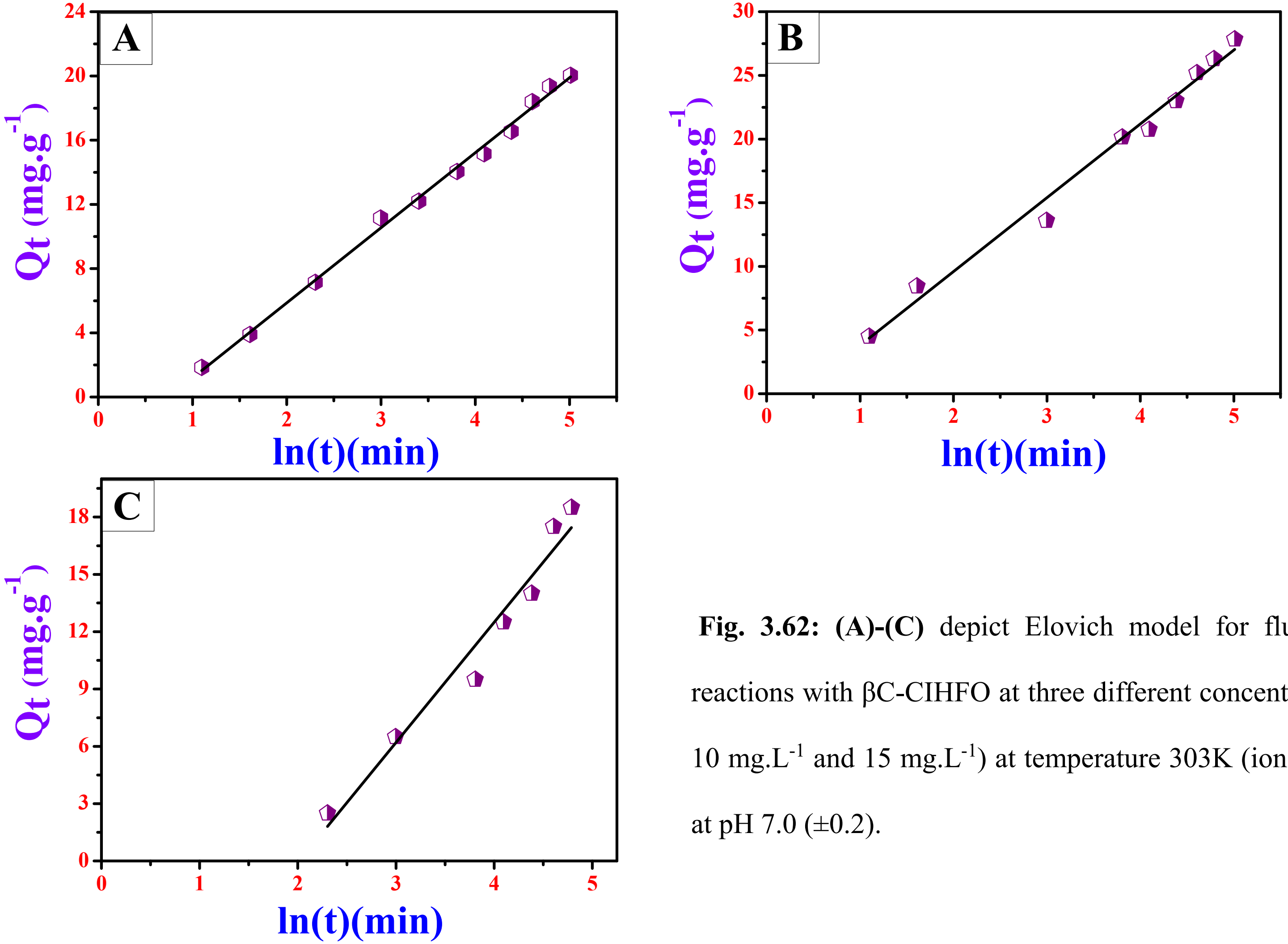

Fig. 3.62: (A)-(C) depict Elovich model for fluoride adsorption reactions with βC-CIHFO at three different concentrations (5 mg.L^{-1}, 10 mg.L^{-1} and 15 mg.L^{-1}) at temperature 303K (ionic strength = 1M) at pH 7.0 (±0.2).

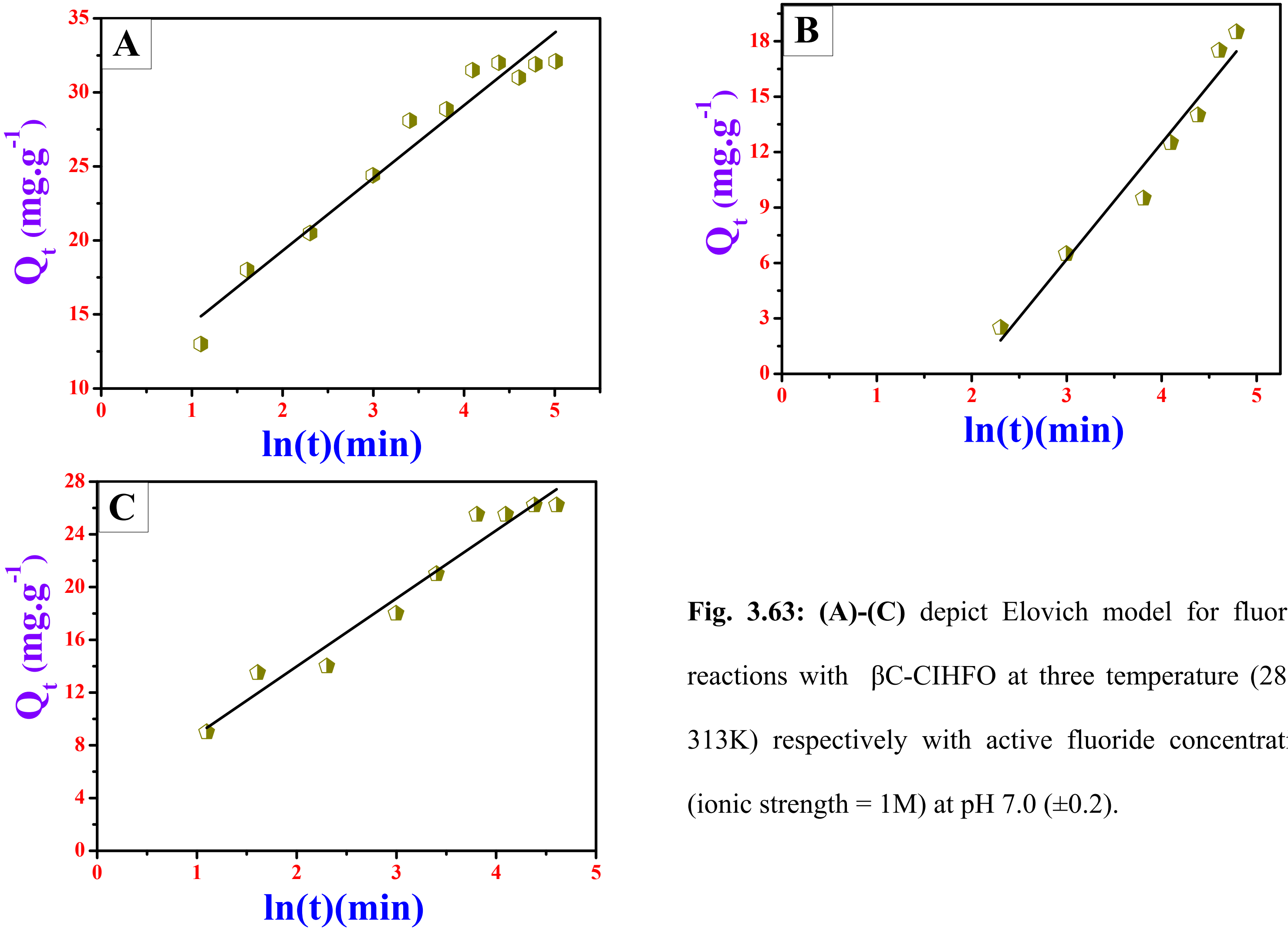

Fig. 3.63: (A)-(C) depict Elovich model for fluoride adsorption reactions with βC-CIHFO at three temperature (288K, 303K and 313K) respectively with active fluoride concentration 15 mg.L^{-1} (ionic strength = 1M) at pH 7.0 (±0.2).

3.6.5. Richenberg Model

Fig.3.64 and Fig.3.65 present the plots of the Richenberg model [βt vs. t (min)] for CIHFO at different fluoride concentration (10 $mg.L^{-1}$, 15 $mg.L^{-1}$, and 20 $mg.L^{-1}$) at temperature 303K and at different temperature (293K, 303Kand 313K) in neutral pH. Whereas **Fig.3.66 - Fig.3.69** denote the plots of the Richenberg model [βt vs. t (min)] for GO-CIHFO and βC-CIHFO respectively with solution concentration (5 $mg.L^{-1}$, 10 $mg.L^{-1}$, and 15 $mg.L^{-1}$) at temperature 303K and different temperatures (288K, 303Kand 313K) in neutral pH. The plots with good linearity accompanied with high correlation coefficient (R^2) values (given in **Table-3.2A and 3.2B**) and did not pass through origin. These results is indicative of the fact that IPD is not the only RSC and this is also support the results obtained from IPD model. The factor βt was calculated from the slope and used to calculate the effective D_i and both are recorded in **Table 3.2A and 3.2B**. If the by values of D_i have been ranged in between of 10^{-6} to 10^{-8} cm^2 s^{-1}, the rate determining step dominated external mass transfer. Whereas the values of Di when obtained in the range of 10^{-11} to 10^{-13} cm^2s^{-1}, intraparticle diffusion is considered as rate controlling step. From the **Table 3A** and Table-3.2B, it has been observed that the values of D_i for the adsorption of fluoride on each adsorbent was in the order of 10^{-6} cm^2 s^{-1},Which is more than 10^{-11} cm^2 s^{-1}, then, intraparticle diffusion was not the only RSC, external mass transfer was also involved in adsorption process. Values of film diffusion (D_1) and pore diffusion (D_2) were assessed and mentioned in **Table 3.2A and Table 3.2B**. Negative exponential values with same order of magnitude assure that both film and pore diffusion process involved in adsorption mechanism.

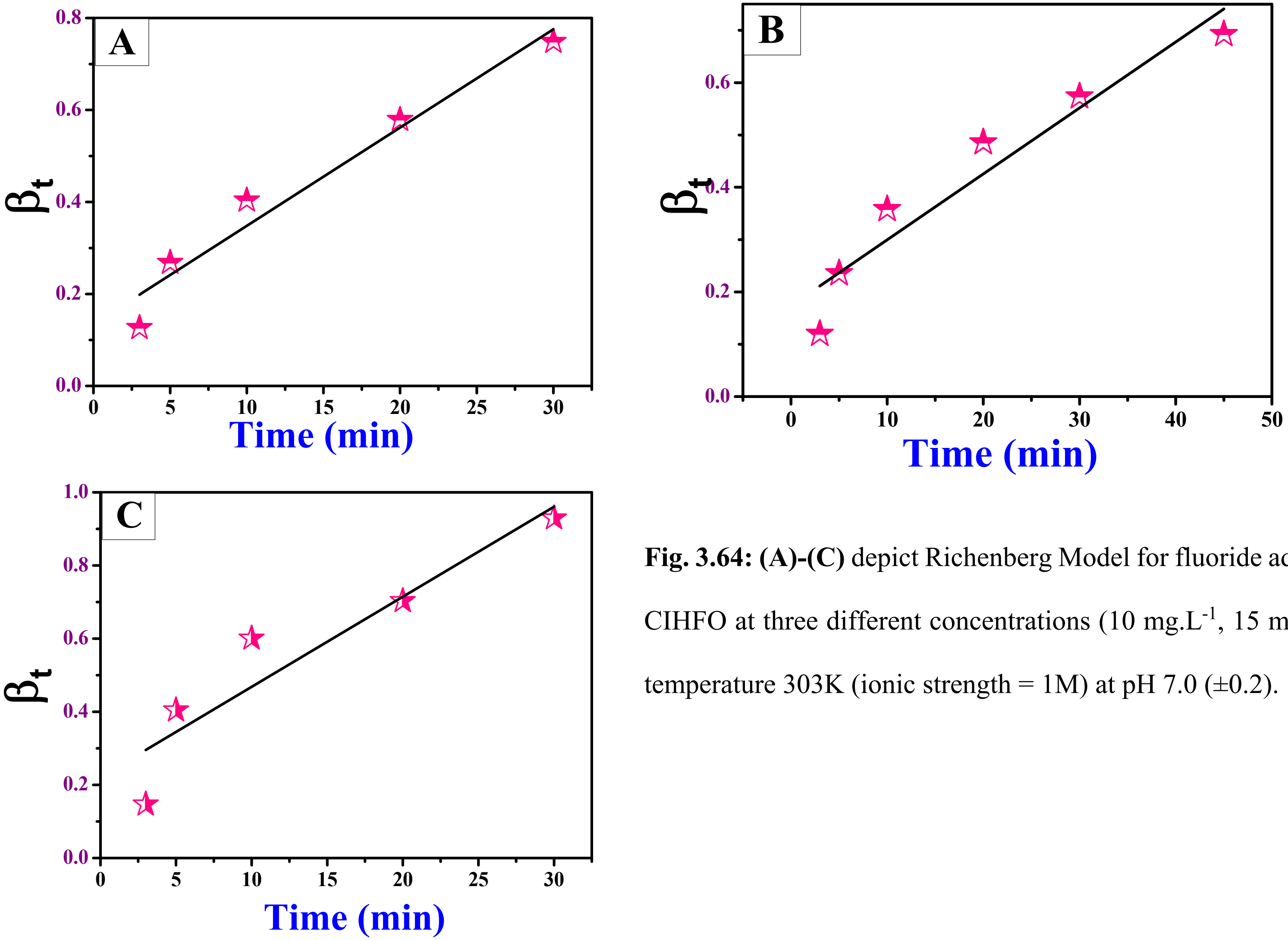

Fig. 3.64: (A)-(C) depict Richenberg Model for fluoride adsorption reactions with CIHFO at three different concentrations (10 mg.L^{-1}, 15 mg.L^{-1} and 20 mg.L^{-1}) at temperature 303K (ionic strength = 1M) at pH 7.0 (±0.2).

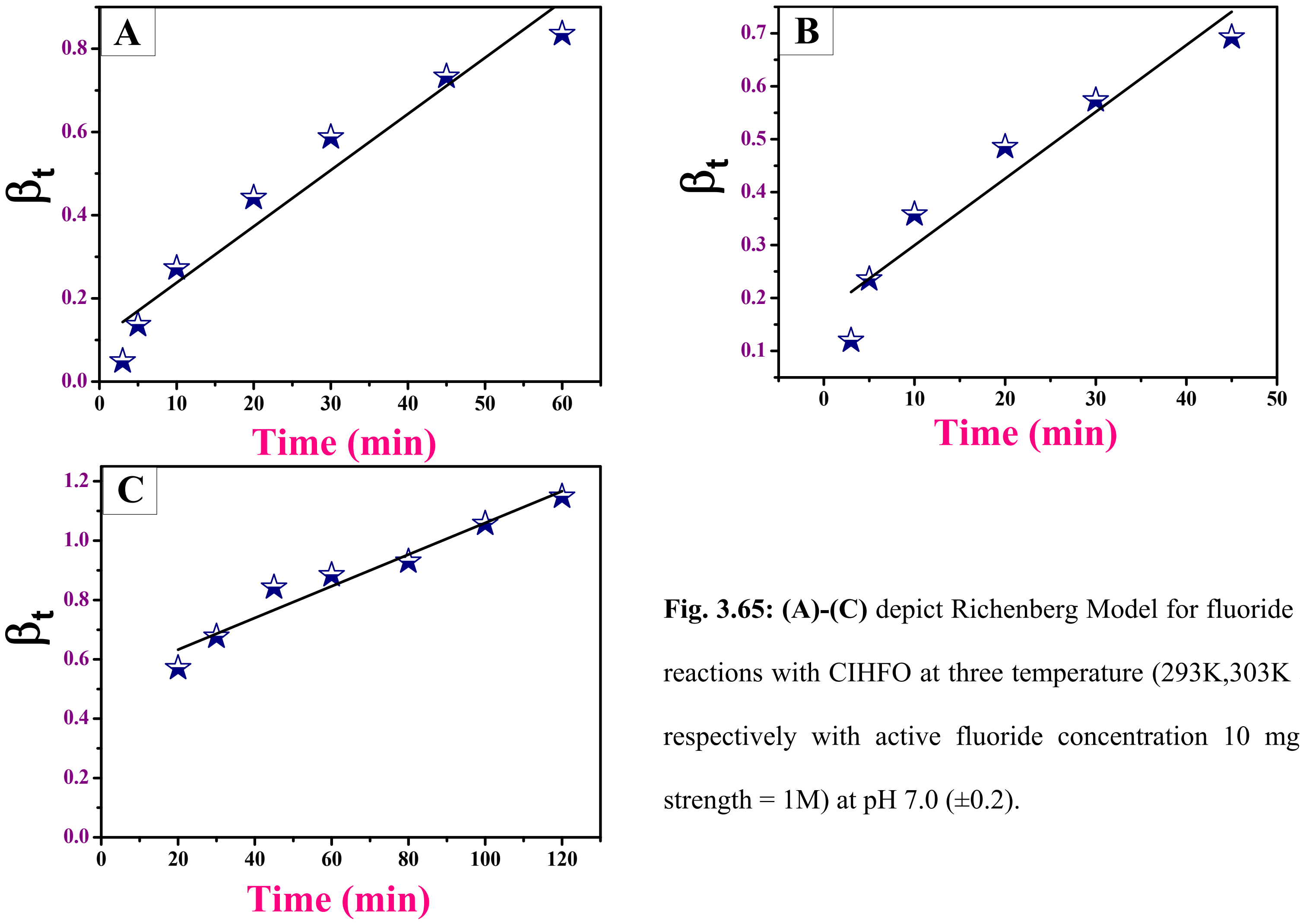

Fig. 3.65: (A)-(C) depict Richenberg Model for fluoride adsorption reactions with CIHFO at three temperature (293K,303K and 313K) respectively with active fluoride concentration 10 mg.L^{-1} (ionic strength = 1M) at pH 7.0 (±0.2).

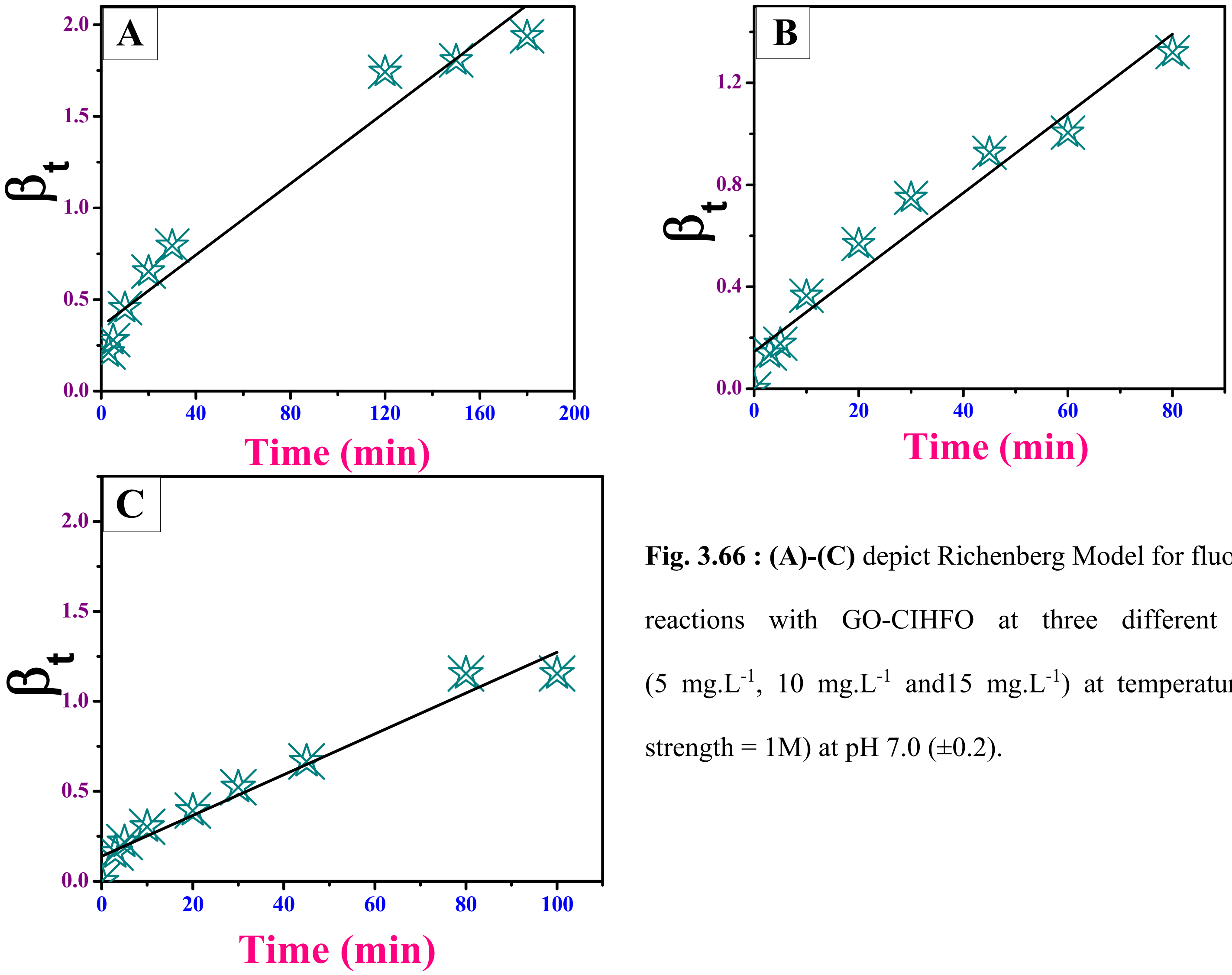

Fig. 3.66 : (A)-(C) depict Richenberg Model for fluoride adsorption reactions with GO-CIHFO at three different concentrations (5 mg.L^{-1}, 10 mg.L^{-1} and15 mg.L^{-1}) at temperature 303K (ionic strength = 1M) at pH 7.0 (±0.2).

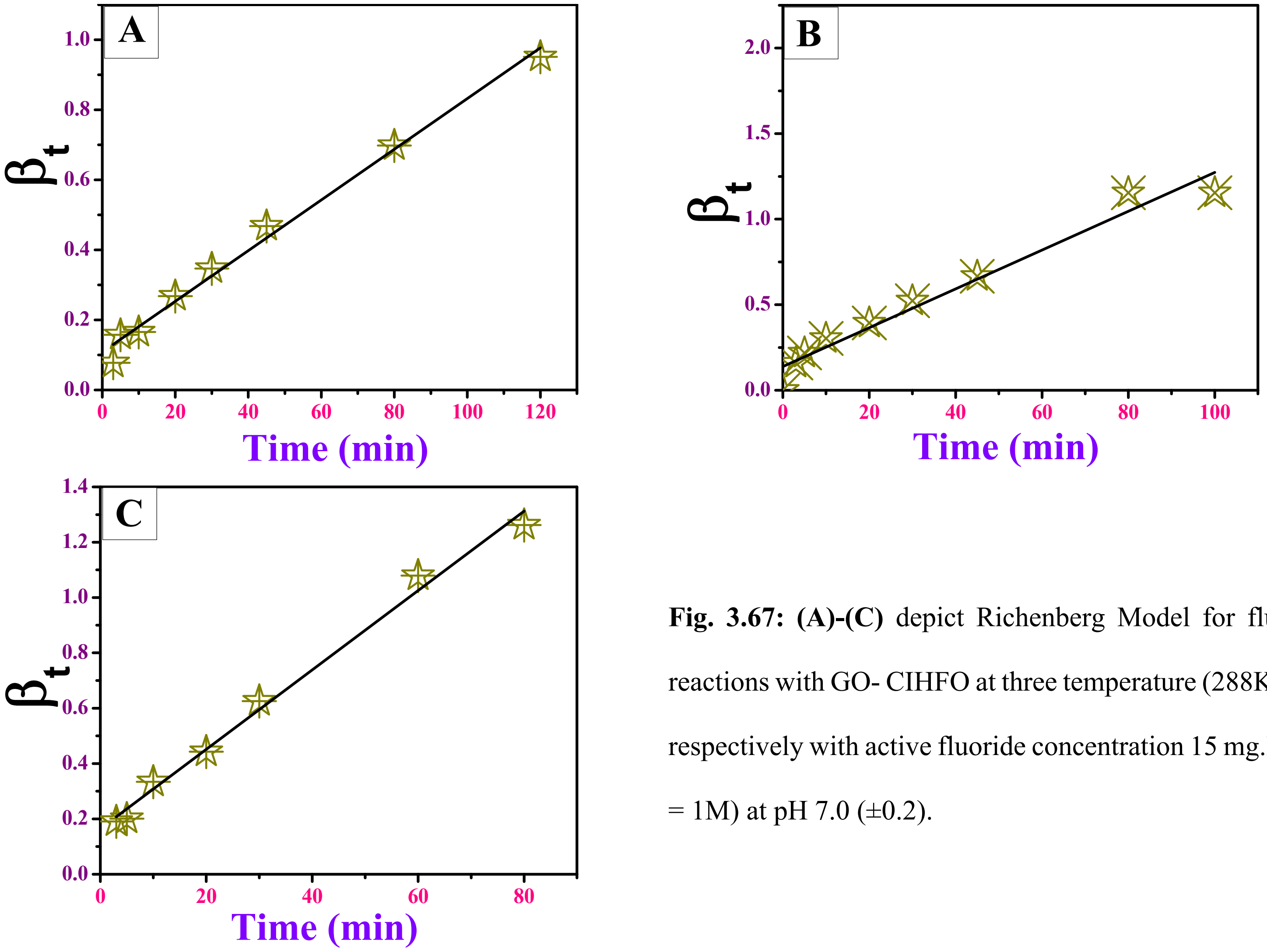

Fig. 3.67: (A)-(C) depict Richenberg Model for fluoride adsorption reactions with GO- CIHFO at three temperature (288K,303K and 313K) respectively with active fluoride concentration 15 mg.L^{-1} (ionic strength = 1M) at pH 7.0 (±0.2).

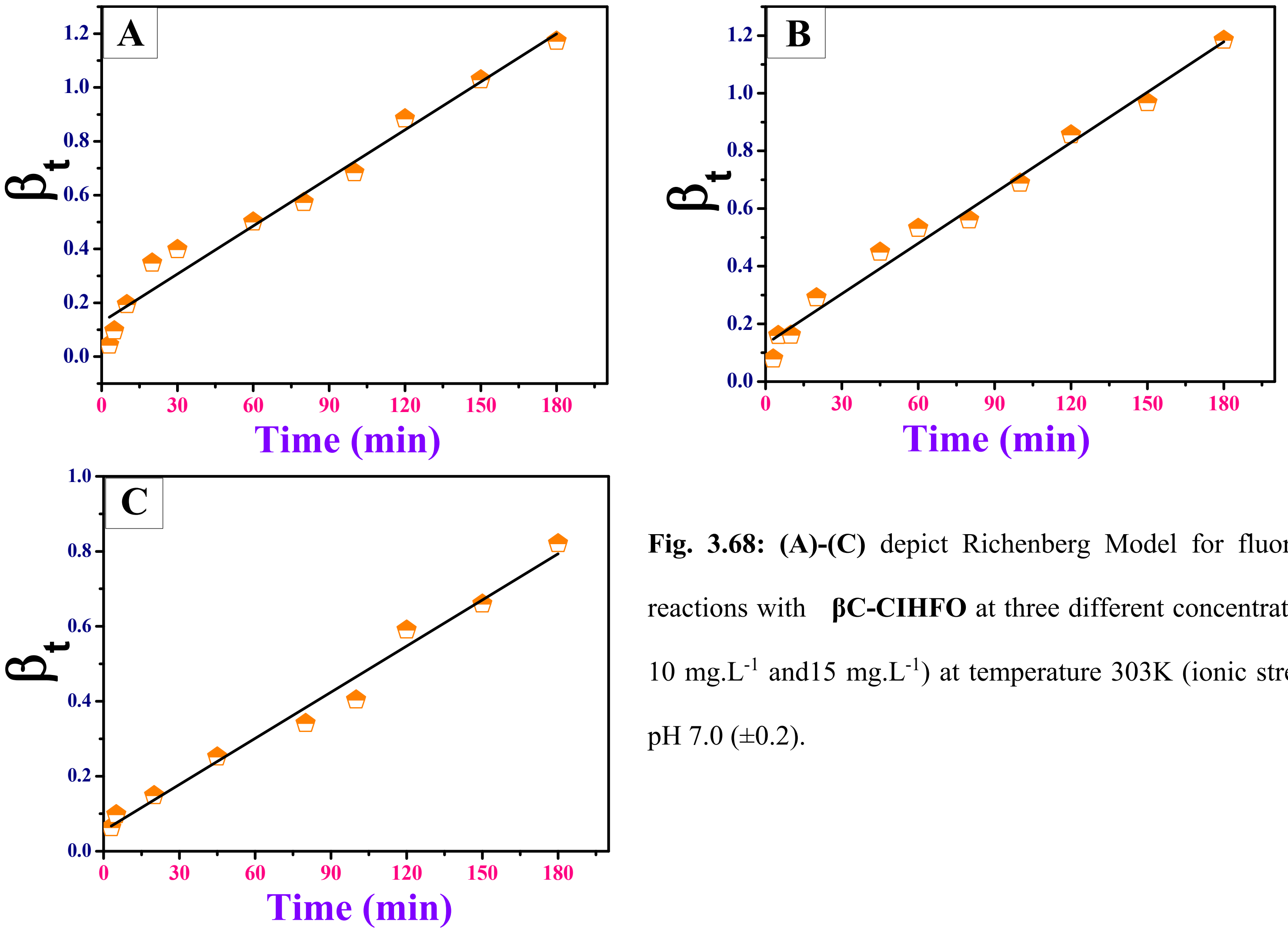

Fig. 3.68: (A)-(C) depict Richenberg Model for fluoride adsorption reactions with **βC-CIHFO** at three different concentrations (5 mg.L^{-1}, 10 mg.L^{-1} and15 mg.L^{-1}) at temperature 303K (ionic strength = 1M) at pH 7.0 (±0.2).

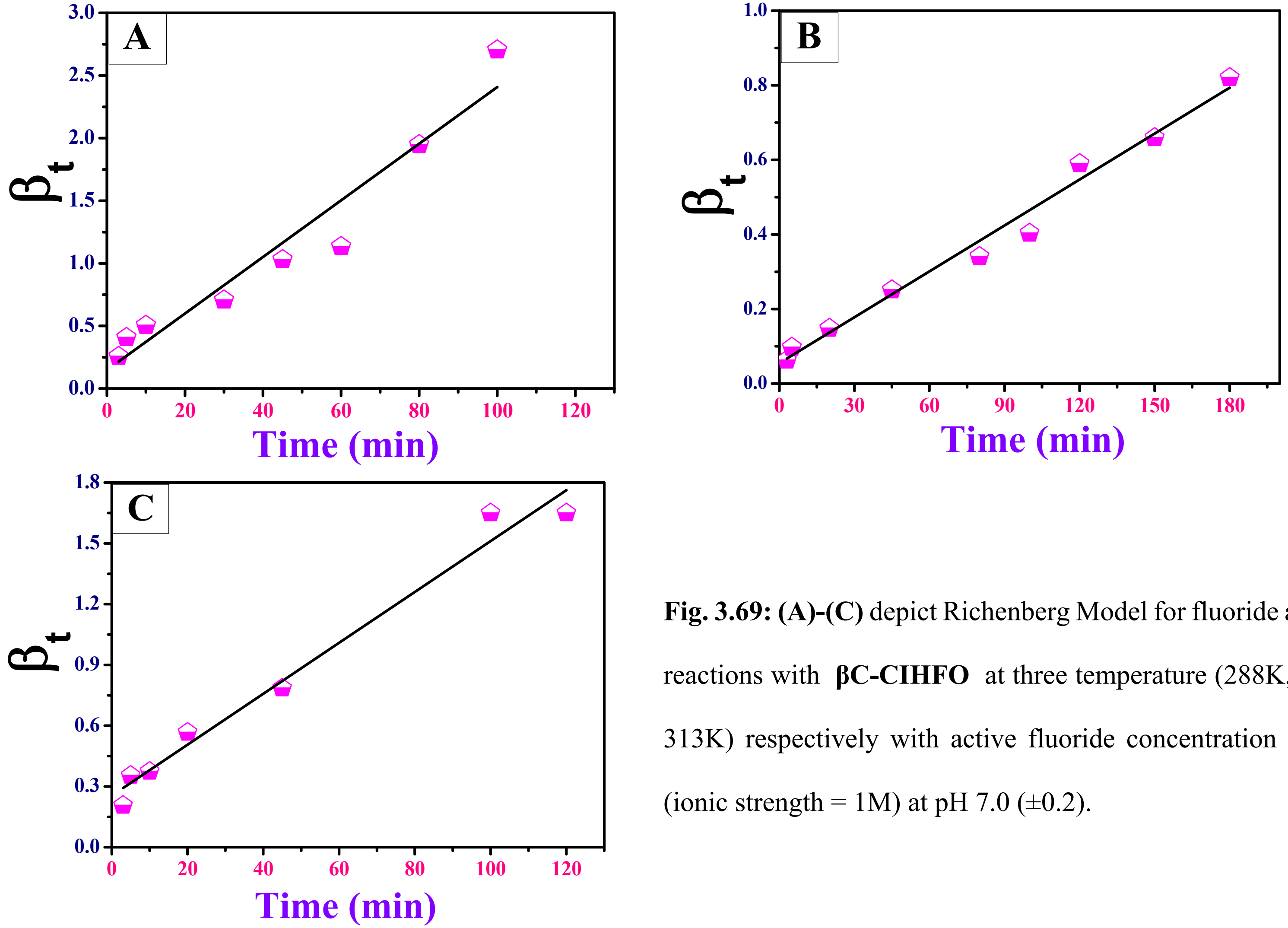

Fig. 3.69: (A)-(C) depict Richenberg Model for fluoride adsorption reactions with **βC-CIHFO** at three temperature (288K,303K and 313K) respectively with active fluoride concentration 15 mg.L^{-1} (ionic strength = 1M) at pH 7.0 (±0.2).

Table 3.2A: Estimated kinetic parameters of Intra-particle diffusion Model, Elovich Model and Richenberg Model for fluoride adsorption reactions with CIHFO, GO-CIHFO and βC-CIHFO at different concentration of Fluoride with solution pH 7.0 and at temperature 303K.

Kinetics Equation	**Parameters**	**βC-CIHFO**			**GO-CIHFO**			**CIHFO**		
		Fluoride concentration (mg. L^{-1})			**Fluoride concentration (mg. L^{-1})**			**Fluoride concentration (mg. L^{-1})**		
		5	**10**	**15**	**5**	**10**	**15**	**10**	**15**	**20**
Intra-particle diffusion Model	**K_{id}(gmg^{-1}min$^{0.5}$)**	1.72	3.31	2.02	1.105	1.43	1.14	1.77	2.54	2.82
	C	1.073	2.153	-3.711	2.086	2.38	4.63	0.258	0.113	1.27
	R^2	0.95	0.96	0.98	0.84	0.89	0.92	0.96	0.94	0.88
Elovich Model	**a(mg/g min)**	4.67	2.42	6.29	1.80	3.27	3.25	2.42	2.37	2.365
	b (g/mg)	-3.48	1.94	-12.67	2.30	-0.089	1.09	1.94	2.80	6.66
	R^2	0.99	0.92	0.95	0.97	0.98	0.98	0.92	0.96	0.97
Richenberg Model	**$\beta_t \times 10^{-2}$ (cm^2 s^{-1})**	0.59	0.58	0.41	0.97	1.55	1.13	2.13	1.26	2.46
	R^2	0.96	0.98	0.98	0.95	0.94	0.95	0.94	0.90	0.83
	$D_i \times 10^{-6}$(cm^2 s^{-1})	1.59	1.56	1.09	2.59	4.15	3.02	5.72	3.37	0.659
	D_1 (cm^2 s^{-1})	0.067	0.064	0.059	0.0548	0.0631	0.0644	0.0602	0.0412	0.041
	D_2 (cm^2 s^{-1})	-0.183	-0.179	-0.121	-0.040	-0.052	-0.030	-0.189	-0.131	-0.264

Table 3.2B: Estimated kinetic parameters of Intra-particle diffusion Model, Elovich Model, Mass Transfer and Richenberg Model for fluoride adsorption reactions with CIHFO (Fluoride concentration -10 mg.L^{-1}), GO-CIHFO and βC-CIHFO at different at different temperature (Fluoride concentration -15mg.L^{-1}) with solution pH 7.0.

Kinetics Equation	**Parameters**	**βC-CIHFO**			**GO-CIHFO**			**CIHFO**		
		Temperature (K)			**Temperature (K)**			**Temperature (K)**		
		288	**303**	**313**	**288**	**303**	**313**	**293**	**303**	**313**
Intra-particle diffusion Model	**K_{id}(gmg^{-1} min$^{0.5}$)**	2.427	2.022	1.565	1.50	1.14	1.126	2.441	1.77	2.782
	C	9.765	-3.711	10.07	2.27	4.63	0.516	-0.595	0.258	0.934
	R^2	0.94	0.98	0.96	0.98	0.92	0.89	0.95	0.96	0.90
Elovich Model	**a(mg/g min)**	4.911	6.293	5.160	4.08	3.25	3.65	4.112	2.421	1.89
	b (g/mg)	9.479	-12.67	3.654	-2.09	1.09	-3.50	-1.728	1.941	3.326
	R^2	0.95	0.95	0.95	0.96	0.98	0.97	0.97	0.92	0.95
Mass Transfer	**$\beta_1 \times 10^{-2}$ (cm^2 s^{-1})**	0.247	0.667	1.17	0.267	0.667	0.829	2.43	4.18	0.35
	R^2	0.92	0.93	0.98	0.87	0.90	0.91	0.94	0.99	0.90
Richenberg Model	**$\beta_t \times 10^{-2}$ (cm^2 s^{-1})**	2.26	0.41	1.257	0.724	1.13	1.46	1.352	2.137	0.534
	R^2	0.93	0.98	0.97	0.98	0.95	0.99	0.93	0.94	0.94
	$D_i \times 10^{-6}$(cm^2 s^{-1})	0.60	1.098	3.36	0.193	3.02	3.91	3.62	5.72	1.43
	D_1 (cm^2 s^{-1})	0.053	0.059	0.048	0.077	0.064	0.163	0.078	0.060	0.076
	D_2 (cm^2 s^{-1})	-0.48	-0.121	-0.354	0.024	0.030	0.109	-0.215	-0.189	-0.226

3.7. Equilibrium Analysis

To recognise the adsorption feasibility of a newly developed adsorbent, different adsorption isotherm models were applied for better understanding of the adsorption process. Langmuir and Freundlich and D-R isotherm are most convenient fundamental isotherm models that can be applied to illustrating the surface properties and adsorption mechanism. For adsorption isotherm study, experiments were carried out at four different temperatures 288K, 303K, 313K and 323 K (293K, 303K, 313K for CIHFO) with initial fluoride concentration in a range of 5 to 60 $mg.L^{-1}$, with solution pH 7.0 and with adsorbent dose 0.2 $g.L^{-1}$ for GO-CIHFO and βC-CIHFO and 0.5 $g.L^{-1}$ for CIHFO respectively.

3.7.1. Langmuir Isotherm

The Langmuir isotherm constants; Q_m (the maximum monolayer adsorption capacity,$mg.g^{-1}$) and K_L (the equilibrium constant related to net enthalpy change of the reaction, $L.mg^{-1}$) respectively were obtained from the plot of non-linear form of Langmuir equation (Eq.2.22) with the help of origin software spread sheet are presented in **Table 3.3** and in **Fig.3.70-3.72**. The Langmuir uptake capacity of CIHFO, GO-CIHFO and βC-CIHFO were found 22.55 $mg.g^{-1}$, 80.42 $mg.g^{-1}$ and 52.32 $mg.g^{-1}$ at neutral pH and at 303 K (30°C). The increasing trend of Q_m value for both adsorbent GO-CIHFO and βC-CIHFO with higher temperature range indicated the endothermic nature of adsorption process while decreasing Q_m value of CIHFO with increasing temperature support exothermic nature of adsorption process.

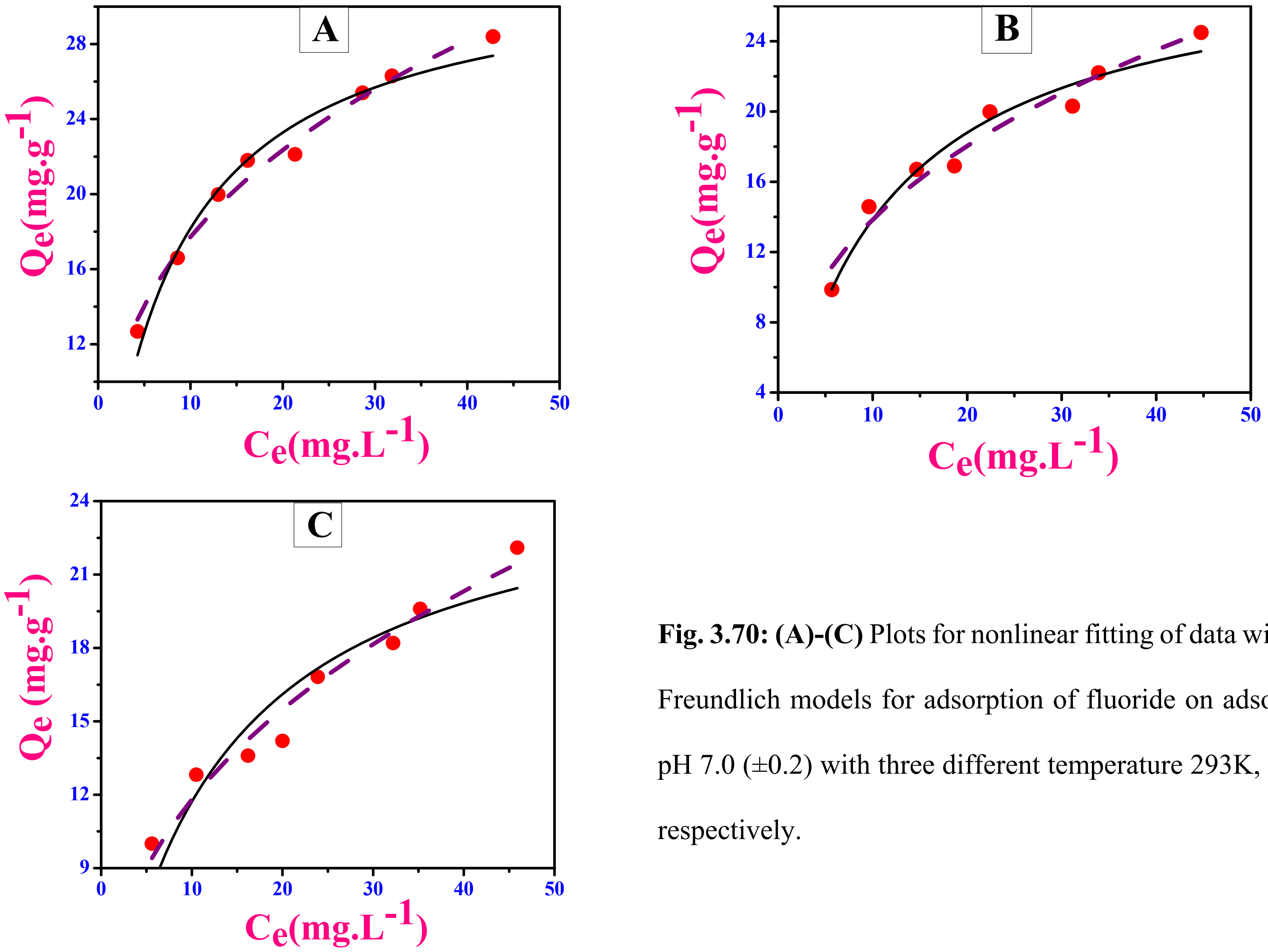

Fig. 3.70: (A)-(C) Plots for nonlinear fitting of data with Langmuir and Freundlich models for adsorption of fluoride on adsorbent CIHFO at pH 7.0 (±0.2) with three different temperature 293K, 303K, and 313K respectively.

3.7.2. Freundlich Isotherm

The values of regression coefficient (R^2), and Freundlich constant (n and K_F) obtained from non-linear Freundlich isotherm equation (Eq. 2.23) analysis are given in **Table 3.3** and in **Fig.3.70-3.72**. Based on values of regression coefficient (R^2), it can be easily concluded that the fitting of equilibrium data were much better with the Freundlich model rather than the Langmuir model. From the assessed values of n, it was perceived that degree of Freundlich coefficient (1/n) is laid in between 0 and 1 that is assuring favourable adsorption of fluoride upon all three prepared proposed adsorbents.

Values of K_F (Freundlich adsorption capacity) was obtained at temperature 303K for solution pH 7.0 for CIHFO, GO-CIHFO and βC-CIHFO were 10.88, 4.71 and 8.30 (mg.g^{-1}) respectively. There was no such brisk enhancement in KF (Freundlich adsorption capacity) values in higher temperature zone in neutral pH. Therefore, 303K and solution pH 7.0 can be considered as optimised temperature and pH for adsorption of fluoride for all three adsorbents.

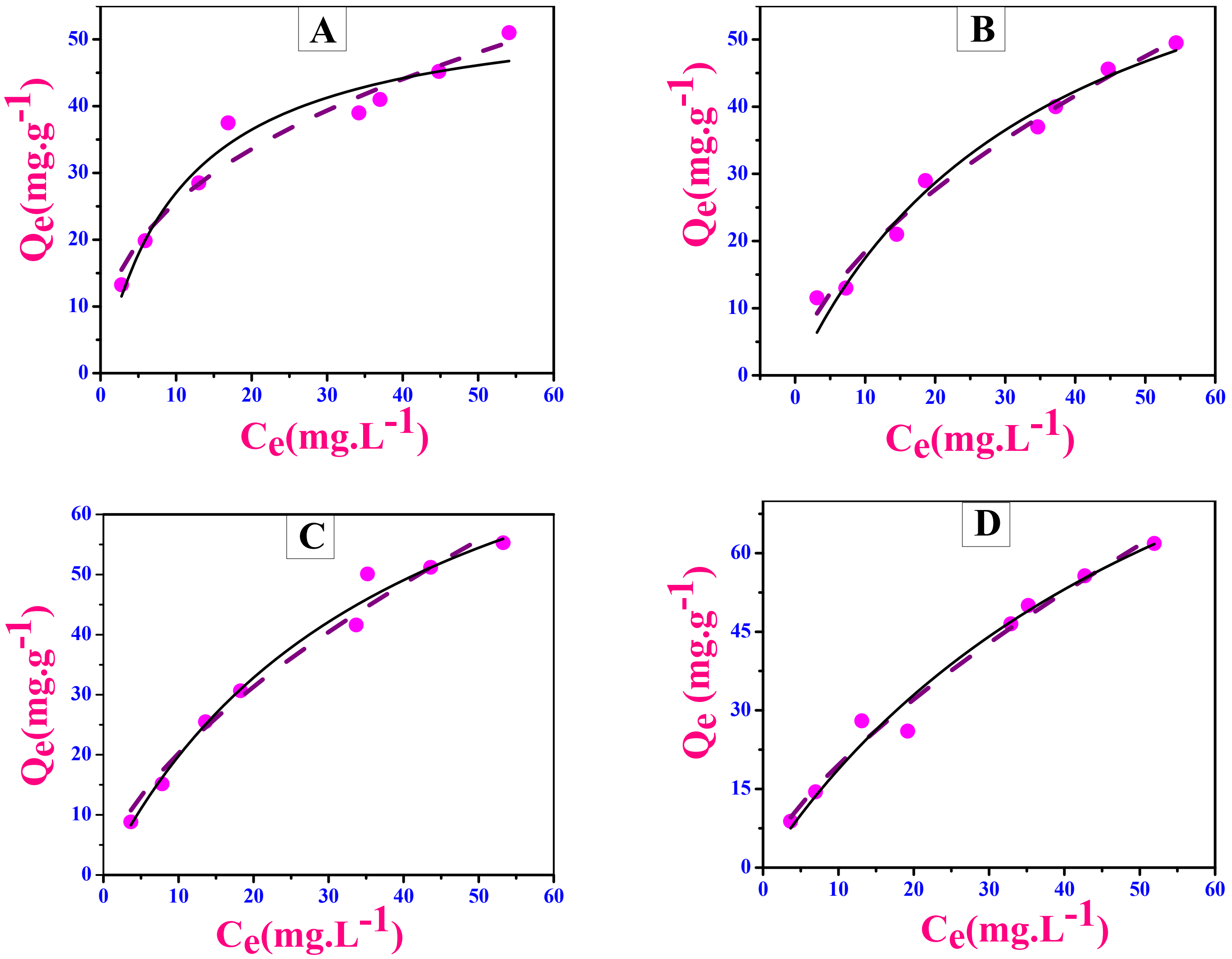

Fig. 3.71:(A)-(D) Plots for nonlinear fitting of data with Langmuir and Freundlich models for adsorption of fluoride on adsorbent GO-CIHFO at **pH 7.0** with four different temperature 288K, 303K, 313K and 323K respectively.

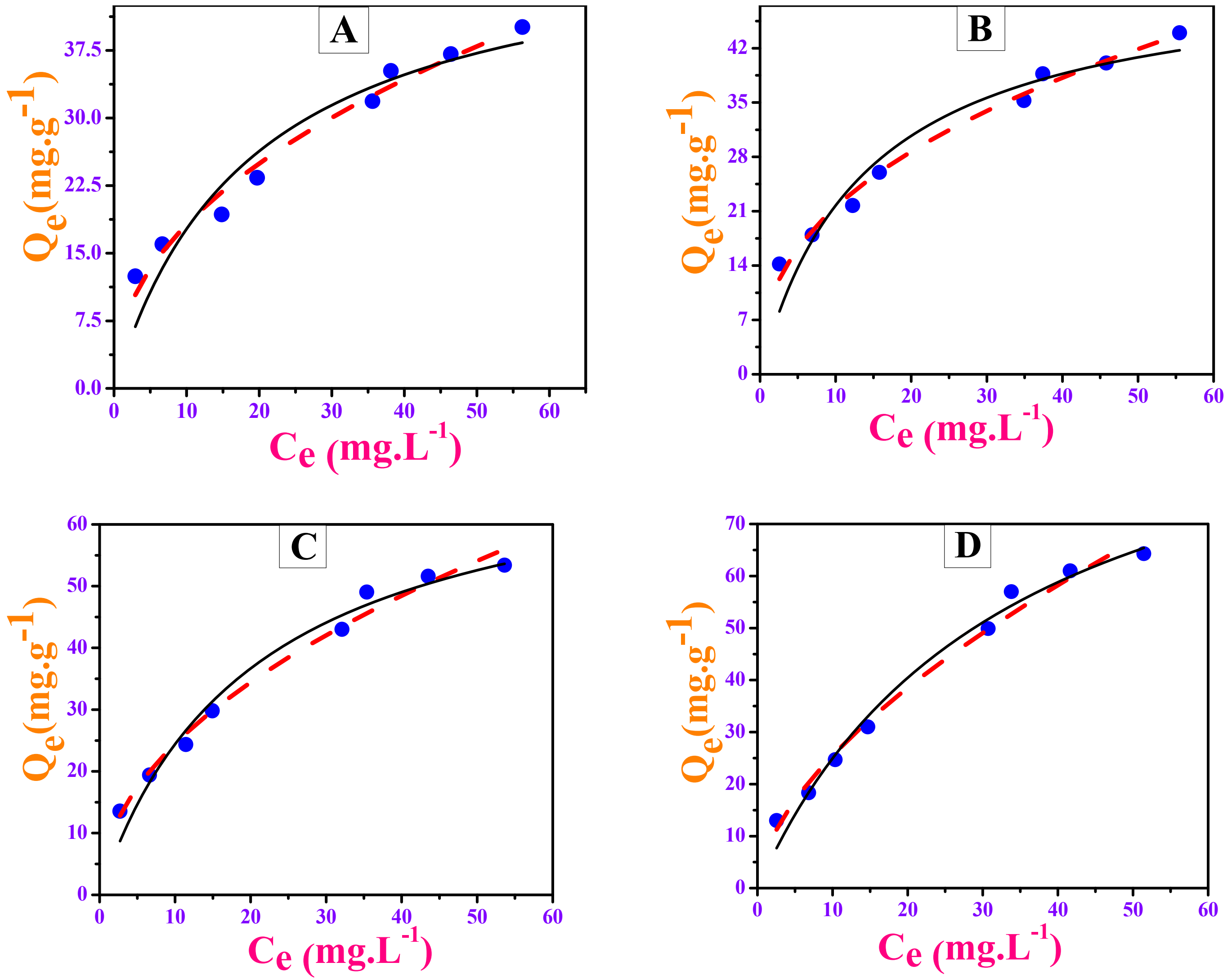

Fig. 3.72:(A)-(D) Plots for nonlinear fitting of data with Langmuir and Freundlich models for adsorption of fluoride on adsorbent βC-CIHFO at **pH 7.0** with four different temperature 288K, 303K, 313K and 323K respectively

3.7.3. D-R Isotherm

Evaluation of the free energy of reaction of any adsorption process and to envisage the nature of adsorption, whether physical, ion-exchange or chemical, D-R isotherm is most widely accepted model in this field. To obtain D–R isotherm parameters, ln Q_e vs. ε^2 were plotted and found to be significantly linear at all the temperatures **(Fig.3.73-3.75)**. The parameters of this isotherm, such as energy of adsorption E_{DR} (kJ mol^{-1}), β (mol^2 kJ^{-2}) and R^2, are mentioned in **Table 3.3**. The substantially high value of R^2 associated with applied temperatures suggested the applicability of the D–R isotherm. D-R equation and according to value of E_{DR}, an adsorption process can be categorised in three types such as (i) physisorption if E_{DR} = 8.0 kJ mol^{-1}, (ii) ion-exchange if E_{DR} = 8.0–16.0 kJ mol^{-1} and (iii) chemisorption if ED–R > 16.0 kJ mol^{-1} (Ghosh *et al.*, 2014; Mukhopadhyay *et al.*, 2017). For CIHFO, gradual increase of the E_{DR} value noticed with rise of temperature from 12.61 to 20.32 kJ mol^{-1} indicates the adsorption of fluoride occurring via ion-exchange to chemisorption phenomena. At 303K the E_{DR} obtained for present case is 15.50 kJ mol^{-1} indicated to be at borderline of ion-exchange and chemisorption.

ε_{DR} values of GO-CIHFO established from D-R isotherm were ranged in between 8.32-9.87 with fluoride solution pH 7.0 indicates the adsorption of fluoride shows predominant trait of physisorption inclined to ion-Exchange phenomena. At temperature 303K temperature, D-R value obtained 9.13 kJ mol^{-1} strongly emphasize the ion-exchange phenomenon.

ε_{DR} values of βC-CIHFO obtained from D-R isotherm were ranged in between 8.77-10.17 with fluoride solution pH was 7.0 specifies that the adsorption of fluoride over βC-CIHFO strongly follow ion-Exchange phenomena. At 303K temperature, 9.95 kJ mol^{-1} ideal example of D-R value that supports ion-exchange phenomenon.

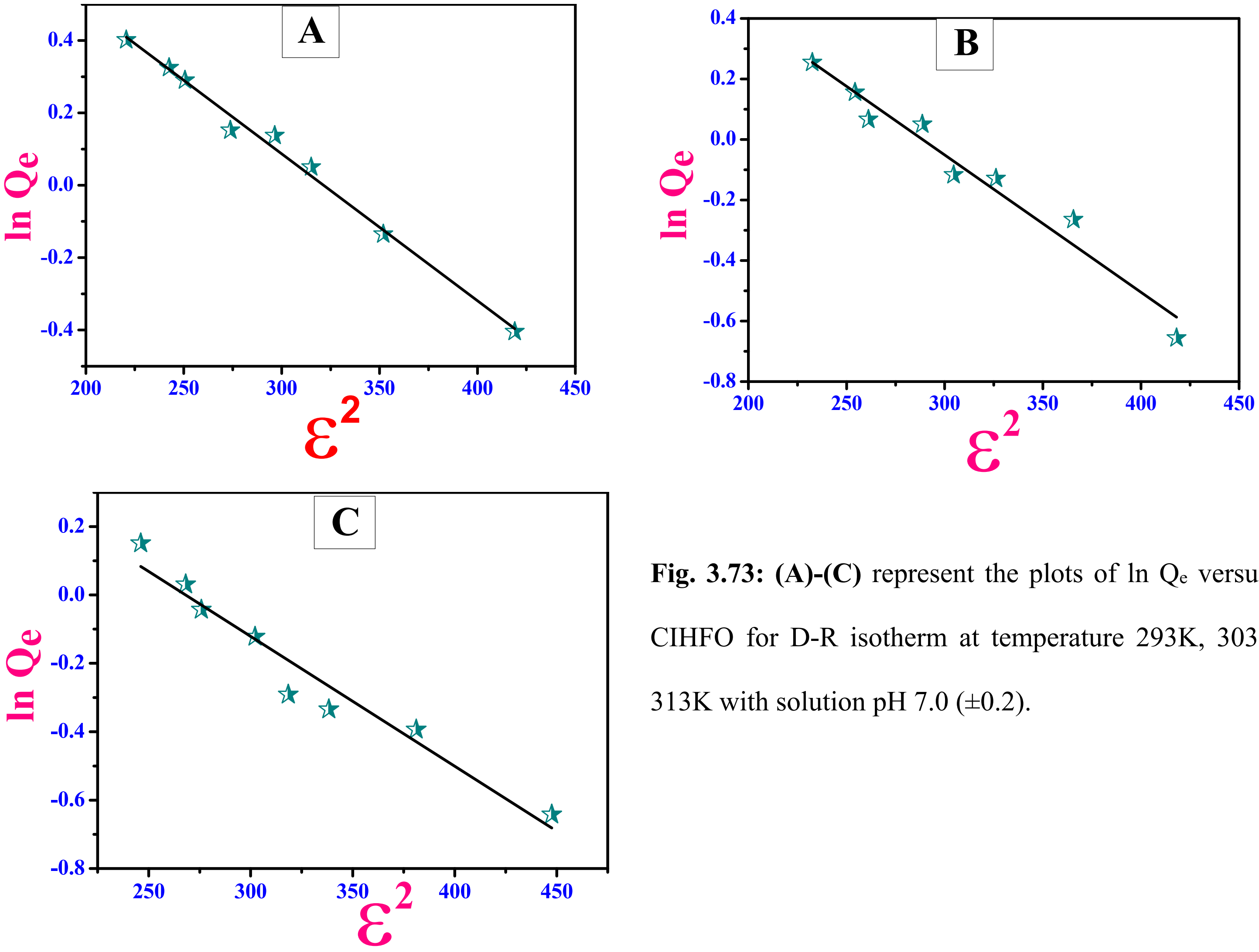

Fig. 3.73: (A)-(C) represent the plots of ln Q_e versus ε^2 of CIHFO for D-R isotherm at temperature 293K, 303K and 313K with solution pH 7.0 (±0.2).

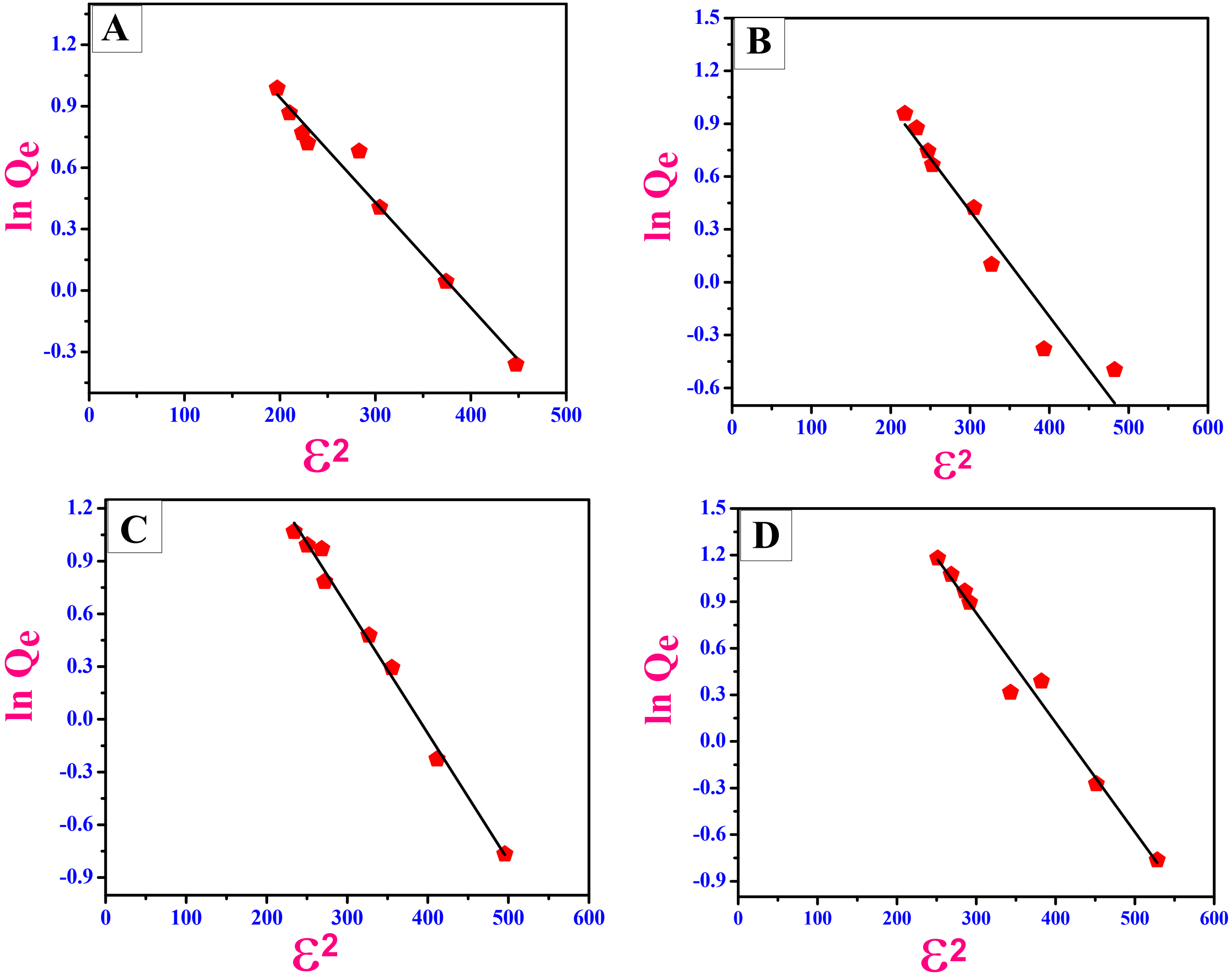

Fig. 3.74: (A)-(D) represent the plots of ln Q_e versus $\boldsymbol{\varepsilon}^2$ GO-CIHFO for D-R isotherm at temperature 288K, 303K, 313K and 323K with solution pH 7.0 (±0.2).

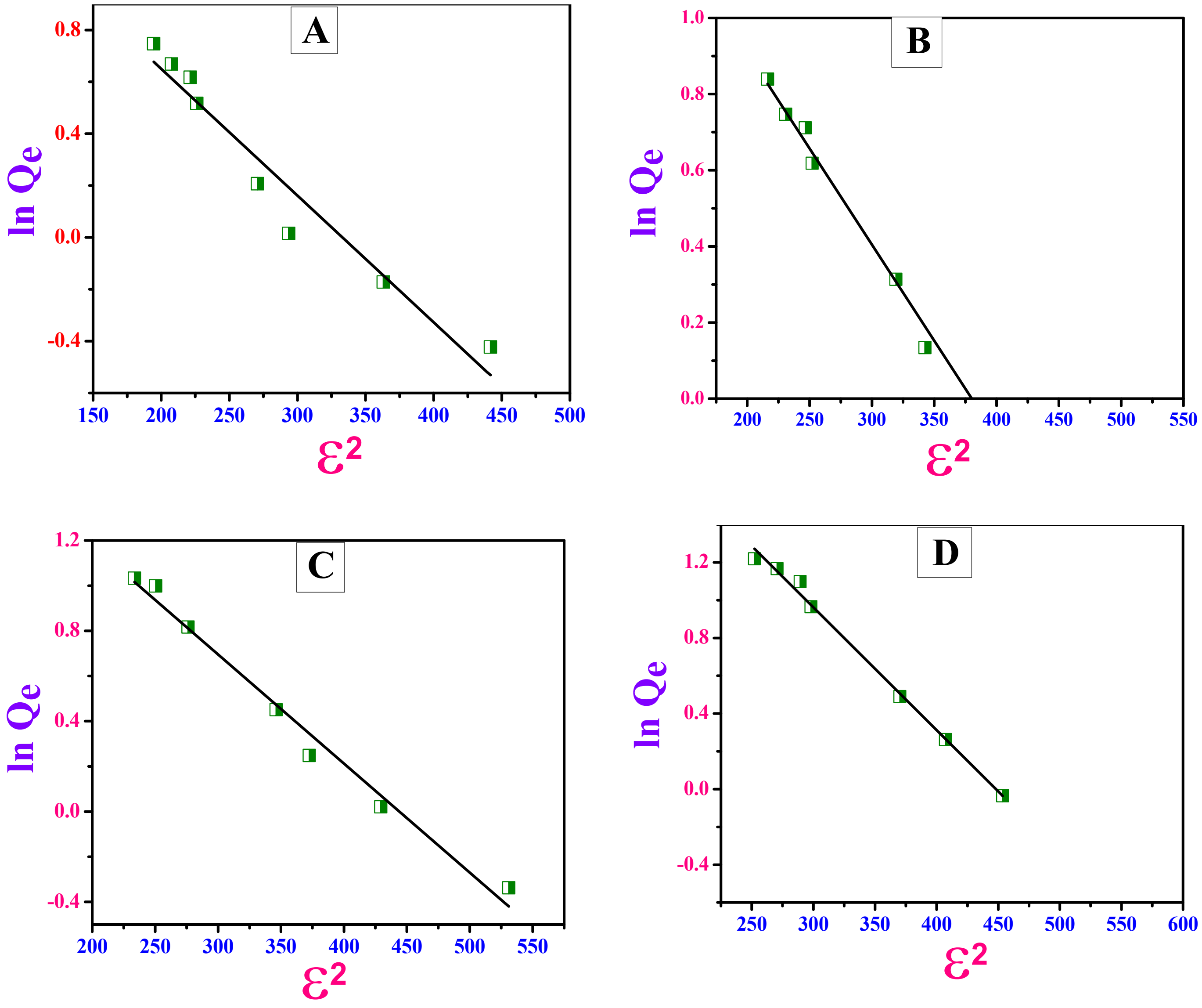

Fig. 3.75: (A)-(D) represent the plots of ln Q_e versus $\boldsymbol{\varepsilon}^2$ βC-CIHFO for D-R isotherm at temperature 288K, 303K, 313K and 323K with solution pH 7.0 (±0.2).

Table 3.3: Isotherm parameters of fluoride adsorption reactions with CIHFO, GO-CIHFO and βC-CIHFO at pH 7.0 (±0.2) at different temperatures.

Isotherm Model	**Parameters**	**βC-CIHFO**				**GO-CIHFO**				**CIHFO**		
		Temperature (K)				**Temperature (K)**				**Temperature (K)**		
		288	**303**	**313**	**323**	**288**	**303**	**313**	**323**	**293**	**303**	**313**
Langmuir	**Q_m (mg g^{-1})**	51.3	52.32	73.949	107.62	56.02	80.42	97.02	136.24	32.62	22.55	16.91
	K_L (L mg^{-1})	0.05	0.071	0.0492	0.030	0.093	0.027	0.022	0.015	0.13	0.66	2.18
	R^2	0.91	0.93	0.97	0.98	0.95	0.97	0.98	0.97	0.96	0.88	0.84
Freundlich	**n**	2.18	2.41	2.02	1.67	2.55	1.69	1.58	1.40	3.10	4.47	7.57
	1/n	0.45	0.41	0.49	0.59	0.39	0.59	0.63	0.71	0.322	0.22	0.132
	K_F (mg g^{-1})	6.34	8.307	7.853	6.439	10.38	4.71	4.75	3.81	8.58	10.88	11.25
	R^2	0.97	0.98	0.98	0.98	0.95	0.98	0.97	0.99	0.99	0.99	0.98
Dubinin–Radushkevich	**Q_m (mol kg^{-1})**	5.09	6.808	8.536	18.35	7.158	9.02	16.60	19.01	3.05	2.07	1.29
	β (mol^2 kJ^{-1}) × 10^{-3}	-4.89	-5.05	-4.83	-6.49	-5.13	-5.99	-7.22	-7.06	3.14	2.08	1.21
	E_{DR} (kJ mol^{-1})	10.11	9.95	10.17	8.77	9.87	9.13	8.32	8.41	12.61	15.50	20.32
	R^2	0.94	0.98	0.98	0.99	0.97	0.93	0.99	0.97	0.99	0.96	0.98

3.8. Thermodynamics Studies

The plots of ln K_C vs. 1/T (van't Hoff Plot) for fluoride adsorption for all three adsorbents in solution pH 7.0 are shown in **Fig.3.76**.The thermodynamic parameters (ΔG°, ΔH°, ΔS°) thus calculated are updated in **Table 3.4**.

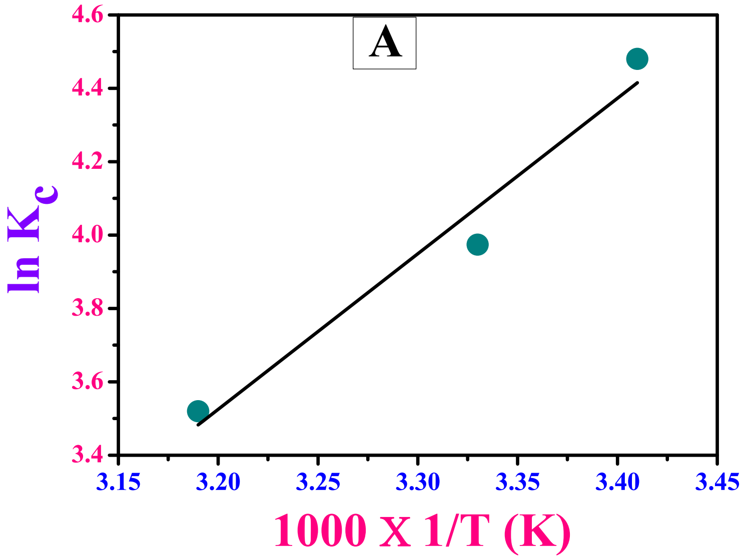

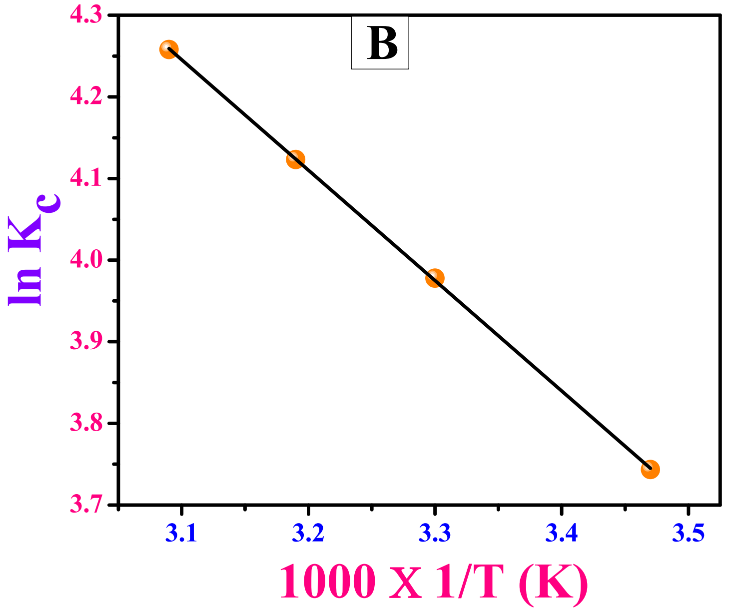

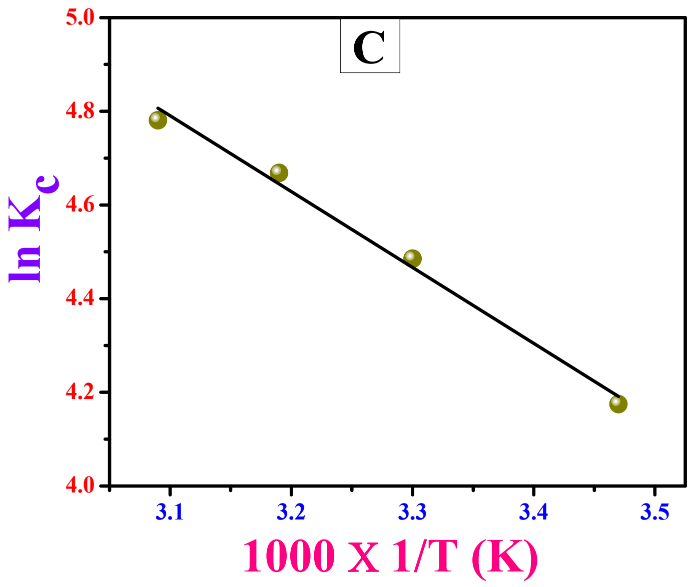

Fig. 3.76: (A)-(C) represent van't Hoff plot for the adsorption of fluoride with CIHFO, GO-CIHFO and βC- CIHFO with solution pH 7.0 (±0.2).

The negative values of ΔG° specified the spontaneous nature of adsorption process. Hence adsorptive forces required for reaction are fairly strong enough to overcome the potential barrier and greater negative values of ΔG° associated with rise of temperature indicated that higher temperature favours adsorption process. The high negative value of ΔH° (-36.279 kJ mol^{-1}) associated with CIHFO indicates that the adsorption process is also exothermic in nature. This was in agreement with the results obtained from the isotherm analysis. The entropy change (ΔS°) was found to be (-86.537 J mol^{-1} K^{-1}), indicating the irreversibility and stability of the adsorption process.

Positive values of enthalpy (ΔH°) for both GO-CIHFO and βC-CIHFO suggested the endothermic nature of adsorption process. The positive values of ΔS° for both GO-CIHFO and βC-CIHFO conditions of whole adsorption experiment system, recommended high degree of freedom of solute molecules owing to adsorption, thus randomness was increased during the adsorption process. This was presumably due to desorption process that simultaneously took place during adsorption, increased the entropy (ΔS°) at the solid–liquid interface (Saha *et al*., 2016).

Table 3.4: Thermodynamic parameters for fluoride adsorption reaction with of all three adsorbents (CIHFO, GO-CIHFO and βC-CIHFO)at pH = 7.0 (±0.2)

Material Name	**Fluoride concentration (mg L^{-1})**	**ΔG° (kJ mol^{-1}) at different Temperatures (K)**				**ΔH° (kJmol^{-1})**	**ΔS° (Jmol^{-1}K^{-1})**
		288	**303**	**313**	**323**		
βC-CIHFO	35	-9.100	-9.880	-10.940	-18.08	13.34	77.47
	60	-8.555	-9.268	-10.169	-11.104	12.26	71.80
GO-CIHFO	35	-9.68	-10.02	-10.72	-11.43	11.22	70.16
	60	-9.22	-9.61	-10.27	-10.97	13.76	76.74

Material Name	**Fluoride concentration (mg L^{-1})**	**ΔG° (kJ mol^{-1}) at different Temperatures (K)**				**ΔH° (kJmol^{-1})**	**ΔS° (Jmol^{-1}K^{-1})**
		293	**303**	**313**	**323**		
CIHFO	25	-11.941	-11.698	-10.971	--------	-25.924	-47.411
	35	-10.913	-10.011	-9.160	---------	-36.279	-86.537

3.9. Activation Energy

The plot of ln k_2 against 1/T, a straight-line with slope ($-E_a/R$) was obtained (**Fig.3.77**). The magnitude of activation energy (E_a) for adsorption of fluoride on the surface of adsorbent has been evaluated from slope of the plot. It was found 26.07 KJ mol^{-1}, 22.61 KJ mol^{-1} and 27.10 KJ mol^{-1} for adsorbent CIHFO, GO-CIHFO and βC-CIHFO respectively. Magnitude of E_a is lesser than 42 KJ mol^{-1},then diffusion control process is thought to be accompanying the adsorption process (Podder and Majumder, 2016). E_a value higher than 42 KJ mol^{-1} is envisaged chemically controlled reaction process also occurred. Here, high magnitude of activation energy for this adsorption study implies that fluoride has high combining affinity with proposed adsorbent surface as diffusion process prefers the movement of solute to the external surface of adsorbent. Considering the value of E_a, it can be assumed fluoride adsorption upon the surface of proposed material is supposed to be associated with ion-exchange that is also significantly support the adsorption pattern obtained from D-R isotherm study.

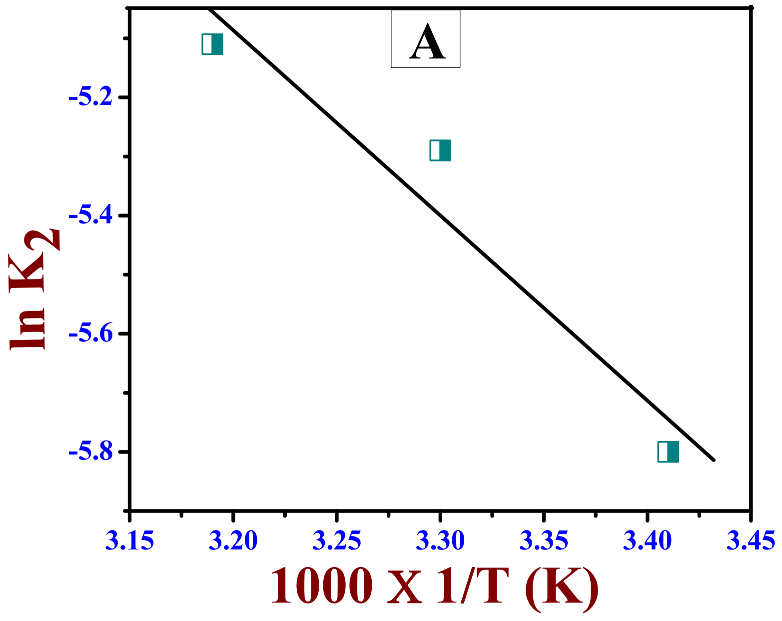

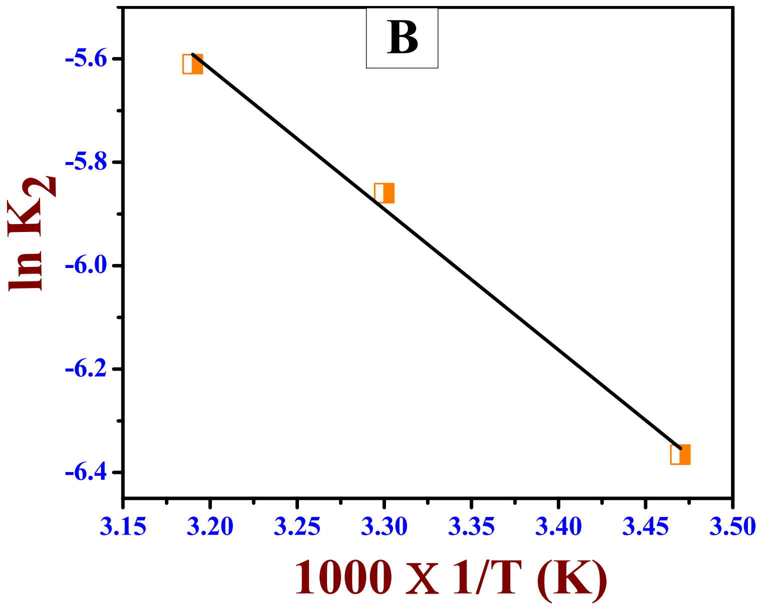

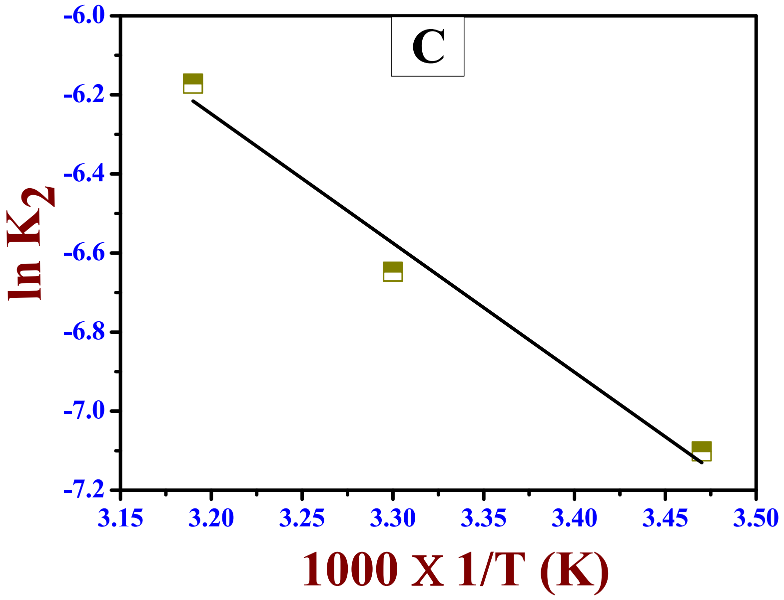

Fig. 3.77: (A)-(C) Represent the plot of ln k_2 versus 1/T (K) for the activation energy for CIHFO, GO-CIHFO and βC-CIHFO respectively

3.10. Effect of Co-occurring Ions on Fluoride Adsorption

Groundwater resource contains a wide range of anions such as SO_4^{2-}, HCO_3^-, HPO_4^{2-} etc. in addition with F^- which may have affinity towards same active sites on adsorbent as reported earlier(Biswas *et al*., 2010; Mukhopadhyay *et al*., 2017; Wen *et al*., 2015).A series of experiments were carried out in presence of these anions with different concentration to explore their influence upon fluoride uptake capacity. In adsorbent CIHFO, sulphate ions hinder fluoride adsorption effectively. It was observed that when the sulphate concentration increased from 10.0 to 150 mg.L^{-1}, the fluoride adsorption amount (9.5 mg.g^{-1}) decreased to 3.3 (mg.g^{-1}), which is only ~30% of the initial value (**Fig.3.78**).

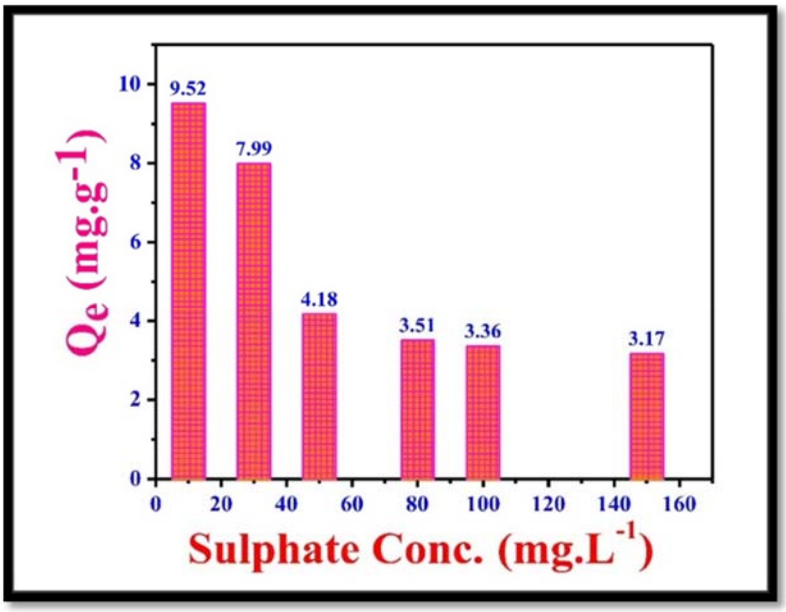

Fig.3.78: Effect of coexisting ions (sulphate ions) upon fluoride adsorption capacity of CIHFO.

However in presence of other ions there was no such change occurred in fluoride adsorption capacity. Hence, the sequence of the adverse influence of the tested ions on fluoride adsorption over CIHFO can be given as $SO_4^{2-} > HCO_3^- > HPO_4^{2-} > NO_3^- >$Cl.

In case of GO-CIHFO, It was observed that these anions at altered concentrations impose no such adverse effects upon fluoride removal even at high concentration. It presumably occurs due to weak or lack of interaction in between adsorbent active sites and said anions.

In case of βC-CIHFO, It was observed that as the sulphate concentration increased from 10.0 to 150 (mg.L^{-1}), the fluoride adsorption capacity 18.21 (mg.g^{-1}) decreased to 11.14 (mg.g^{-1}) and increase of phosphate concentration from 0.1 to 10 (mg.L^{-1})resulted significant change in fluoride adsorption from 18.94 (mg.L^{-1})to 13.87 (mg.L^{-1}).Categorisation of co-occurring ions on fluoride adsorption can be sequenced as $SO_4^{2-} > HPO_4^{2-} > HCO_3^- > NO_3^- > Cl^-$. Other ions produced so such adverse impact upon fluoride adsorption (**Fig.3.79**).

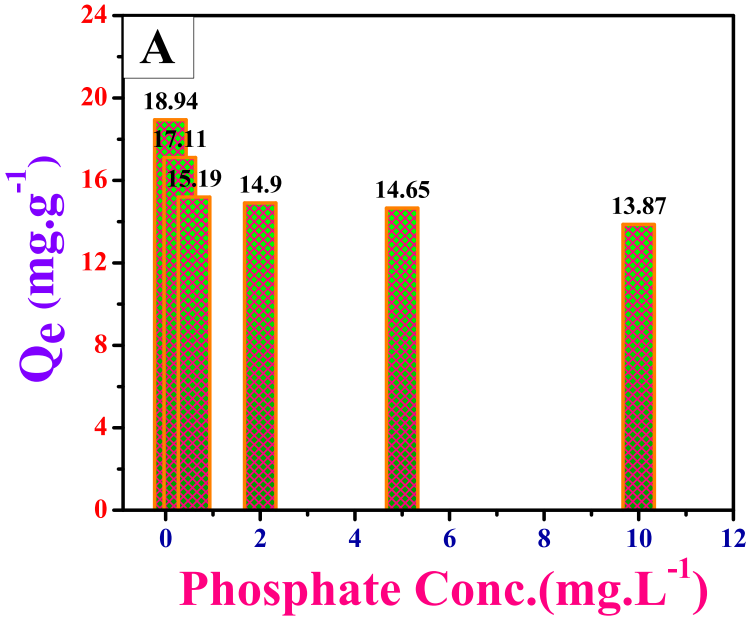

Fig.3.79A: Effect of coexisting and phosphate ions upon fluoride adsorption capacity of βC-CIHFO

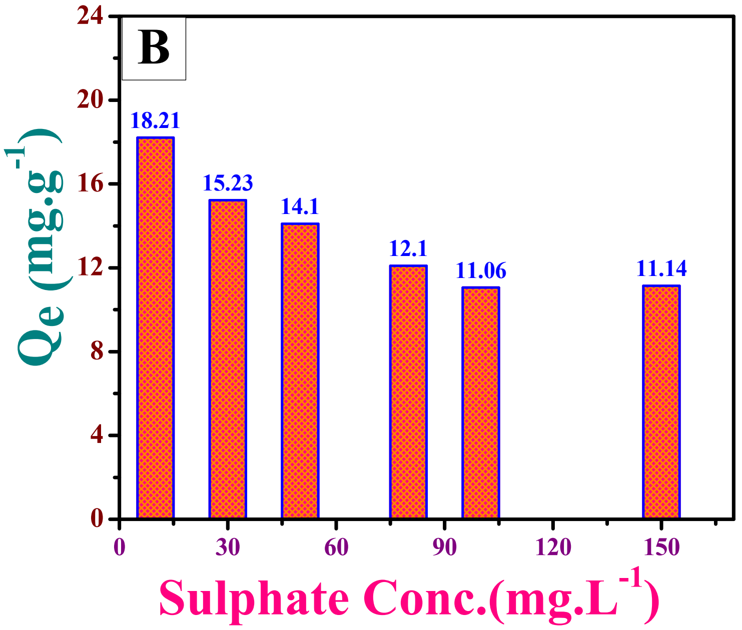

Fig.3.79B: Effect of coexisting and sulphate ions upon fluoride adsorption capacity of βC-CIHFO.

3.11. Desorption and Re-usability of Proposed Adsorbent

Regeneration is a useful tool to regain the adsorptive capacity of any adsorbent. Development of a cost-effective adsorbent and commercialisation of it, is highly dependent on the recycling nature of the adsorbent. To establish the reusability of proposed material desorption study was carried out. For fulfilling the experimental study purpose, fluoride adsorbed GO-CIHFO and βC-CIHFO are generated by adsorbing 60 mg.L^{-1} fluoride solution in 10 g.L^{-1} of GO-CIHFO and βC-CIHFO respectively at pH 7.0.Then Fluoride adsorbed materials were subjected to desorption study by maintaining pH values (8-13) by addition of 0.1 M NaOH or 0.1 M HCl solution as per requirement. The fluoride free material then air dried and collected for repeating the aforesaid adsorption-desorption study (Barathi *et al*., 2014; Mohan *et al*., 2016). The adsorbents were reused for five cycles in this study.

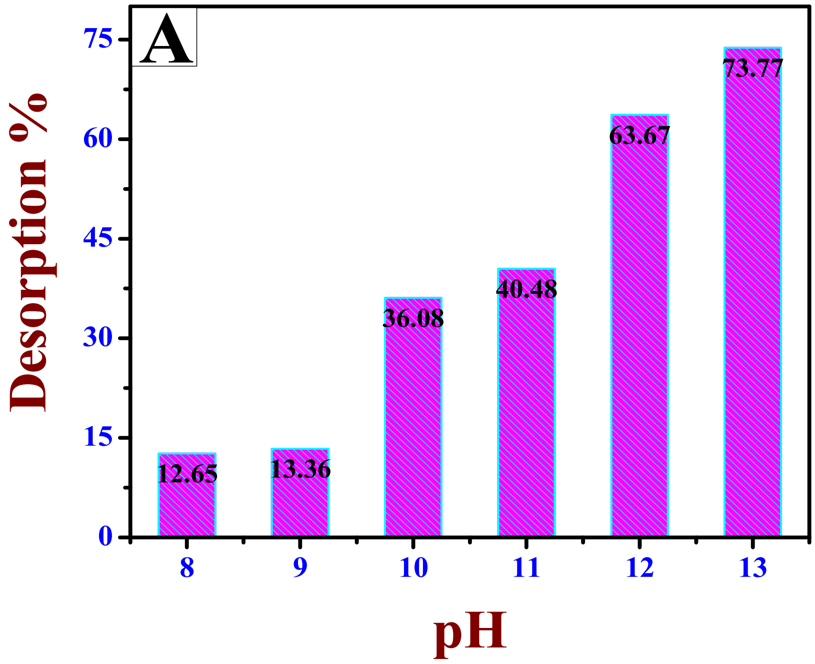

Fig.3.80A: Desorption study of fluoride loaded adsorbent GO-CIHFO at various pH values

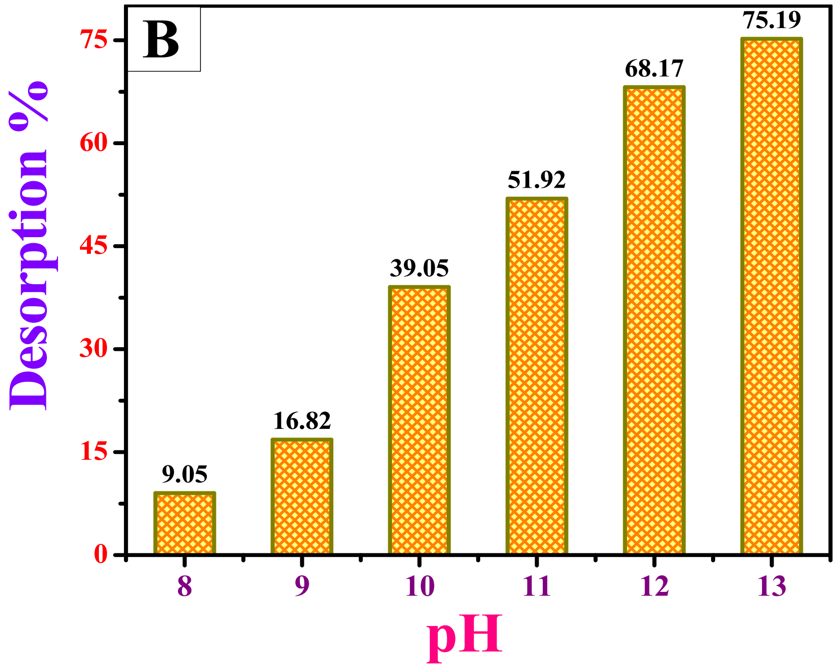

Fig.3.80B: Desorption study of fluoride loaded adsorbent βC-CIHFO at various pH values

It was experimentally approved that no such rise in fluoride concentration was noticed in solution up to pH 9 for both adsorbent GO-CIHFO and βC-CIHFO, afterward desorption efficiency of fluoride sequentially increased to 73.77 % for GO-CIHFO and 75.19 % for βC-CIHFO at pH 13(**Fig.3.80**). During recycling, in case of GO-CIHFO, the percentage of adsorption of fluoride was found to be 69.19%, and 16.66% respectively for the 1st and 5th cycles of reuse. For βC-CIHFO, the percentage of adsorption of fluoride was found to be 71.11%, and 21.02% respectively for the 1st and 5th cycles of reuse (**Fig.3.81**) (Mohan *et al.*, 2016).

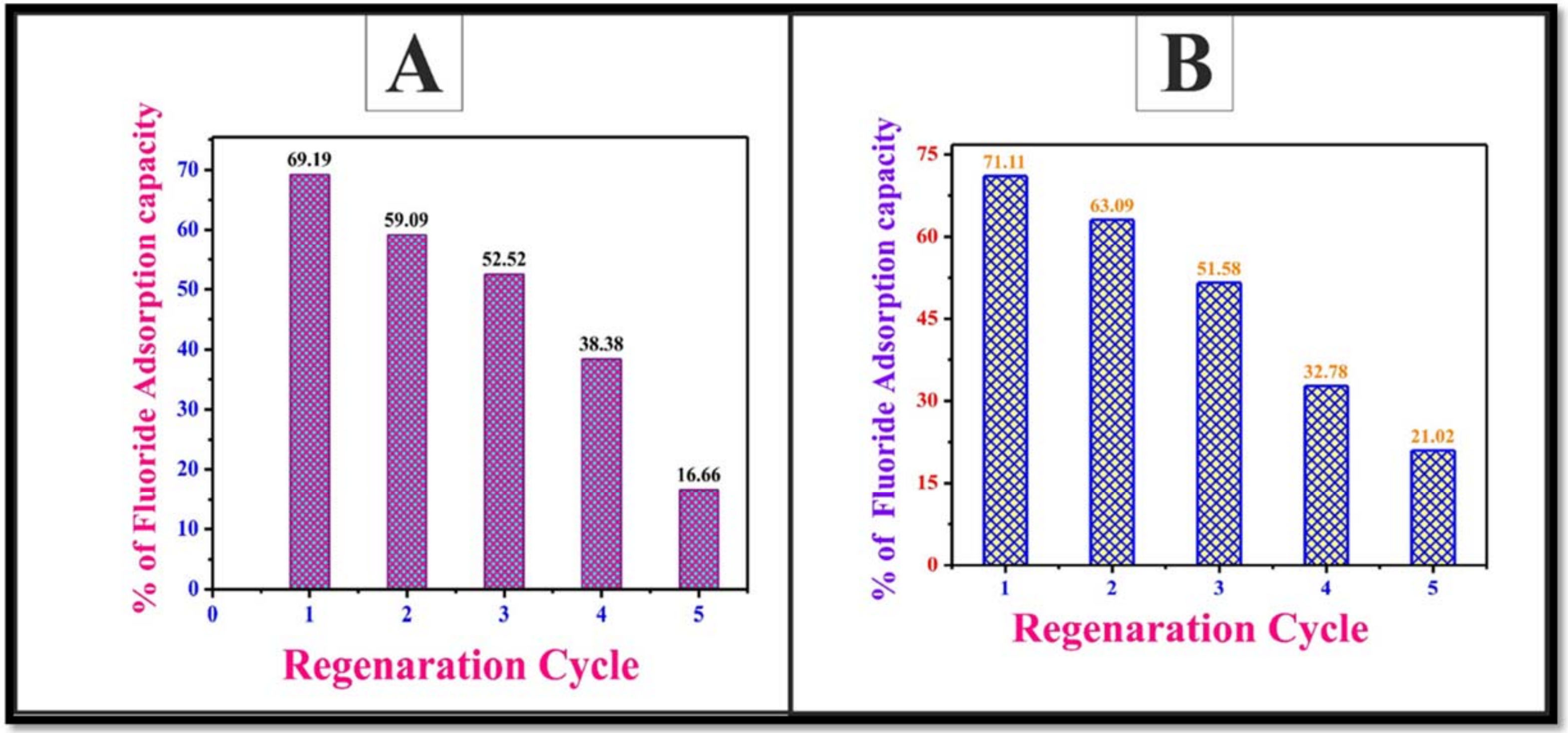

Fig.3.81: Regeneration outcome of proposed adsorbent GO-CIHFO and βC-CIHFO over five cycles.

The Desorption percentage for CIHFO improved with increasing basicity and maximum ~61% desorption occurred (**Fig.3.82**). As the process is predicted as borderline chemisorption and exothermic in nature so it is quite obvious the product is gaining more stability than the reactant. And as the desorption tendency is moderate so the leaching tendency of fluoride to the environment also less.

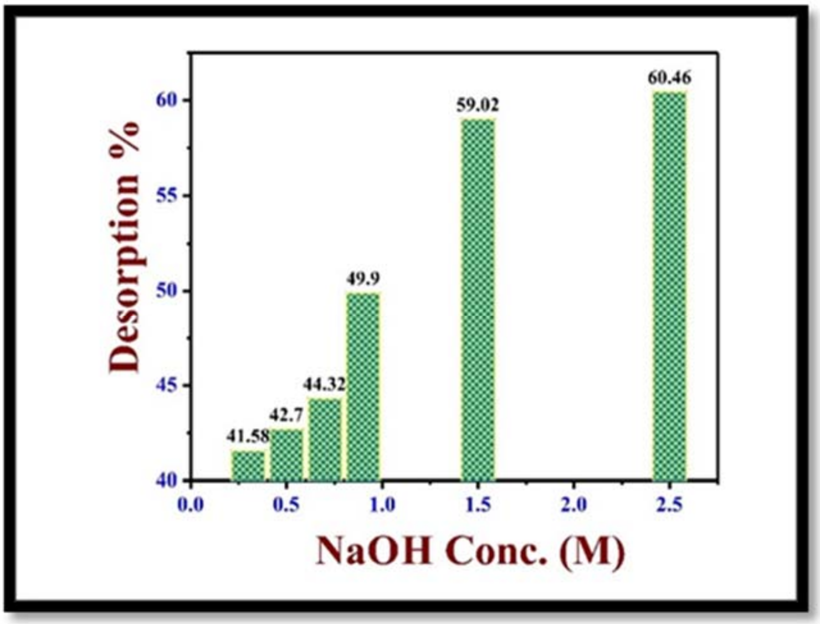

Fig.3.82: Represents molar concentration of NaOH on desorption of fluoride from CIHFO surface.

3.12. Removal of Fluoride from a Natural Groundwater Sample

Purulia District situated in the eastern fringe of State of West Bengal, India, is now in limelight for high concentration of Fluoride in Groundwater and situation is get worse day to day. Considering such adverse situation of this region, water samples have been collected from few selective hand pump attached tube-wells of Kashipur block of Raghunathpur Subdivision of Purulia District. Water sample collected from (Latitude - 23°28’303" N; Longitude- 86°

40’027" E, Elevation-161m) Kharai village of Kashipur block of Purulia district, West Bengal, was reported with high fluoride concentration (9.05 mg.L^{-1}), among all collected samples. Some physic-chemical parameters of water sample from Kharai village were specially also carried out to evaluate overall water quality before experiments are given in parenthesis (mg.L^{-1}, excepting pH) are pH (7.36), fluoride (9.05), iron (total) (0.77), calcium (18.05), magnesium (3.69), hardness (21.74), TDS (679), salinity (473), conductivity (959 µS) and turbidity (18 NTU). One litre of this water sample was stirred (500 rpm) with the help of magnetic stirrer for 2 hours with changing dosage for each adsorbent namely, CIHFO, GO-CIHFO and βC-CIHFO from 0.1 g to 1.5 g. After completion of the experiment time, treated water was filtered and analysed for the fluoride level. It was found that fluoride level reduced from9.05 mg.L^{-1} to below 1.0 mg.L^{-1} when the dosage of CIHFO-2.4 g.L^{-1}; dosage of GO-CIHFO - 1.2 g.L^{-1} and dosage of βC-CIHFO- 1.8 g.L^{-1} respectively employed. Thus, it can be experimentally approved that 2.4 g of CIHFO, 1.2 g of GO-CIHFO and 1.8 g of βC-CIHFO can efficiently reduce fluoride level to desired concentration (1.0 mg.L^{-1}) which is well below the WHO recommended guide line for maximum fluoride concentration level (Mukhopadhyay *et al.*, 2017).

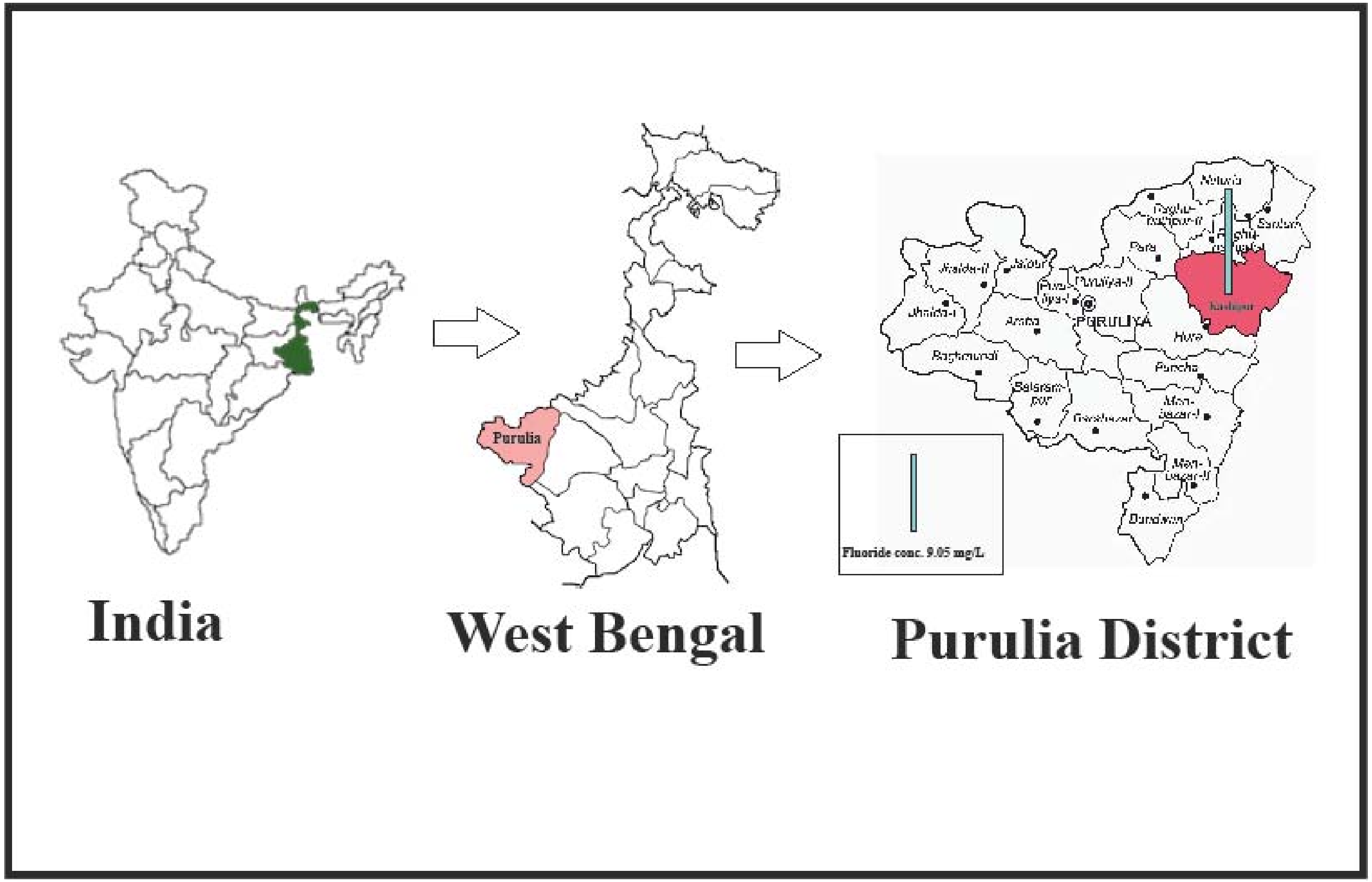

Scheme 3.1: Geographical position of Maximum fluoride contaminated Kashipur block of Raghunathpur Subdivision of Purulia District, West Bengal, India.

3.13. Proposed Mechanism of Fluoride Adsorption over CIHFO, GO-CIHFO and βC-CIHFO

3.13.1. Proposed Mechanism for CIHFO

Based on the measured pH_{zpc} of CIHFO and pH effect on fluoride adsorption, it can be assumed that under acidic pH condition fluoride ions are more involved with the adsorbent surfaces due to electrostatic attraction between negatively charged adsorbate and positively charged adsorbent surfaces. As the energy of activation is low, fluoride might be dispersed very rapidly over the CIHFO surfaces using the minimum energy. The E_{DR} values (12.61, 15.50 and 20.32 kJ. mol^{-1}, respectively, at 293, 303 and 313 K) obtained from the modeling of equilibrium data with D-R isotherm predict that the adsorption process is ion-exchange to borderline chemisorption. During adsorption process, as per the experimental results, the univalent surface hydroxyl ions might be exchanged by fluoride ions leading to the formation of stable complex with potential energy lower than the reactants (Scheme 3.2). Large negative value of ΔH^0 and lesser tendency of fluoride desorption support the said observation. Moreover, the FTIR spectrum of adsorbed CIHFO when compared with that of CHIFO (Fig.3.1A &B) shows the significant reduction of O-H stretching and bending band intensities, and near disappearance of bands at 1400 cm^{-1} and 750 cm^{-1}, validates the proposed mechanism.

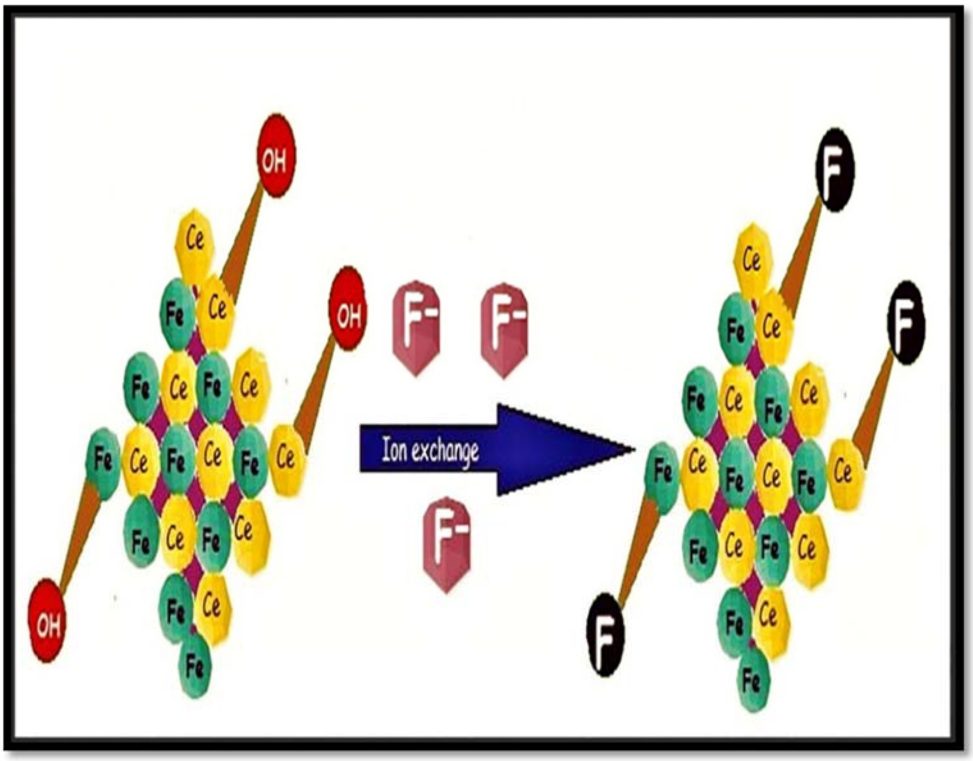

Scheme 3.2: Graphical presentation of proposed reactions mechanism of fluoride adsorption process involved over **CIHFO**

3.13.2. Proposed Mechanism for GO-CIHFO

Probable mechanism of fluoride adsorption over GO-CIHFO has been assumed based on data obtained from pH effect and FTIR spectra analysis and explained schematically in Scheme 3.3. Results of measured pH_{ZPC} and pH effect upon fluoride adsorption suggested that as per HSAB principle, in prepared adsorbent, Fe^{3+} and Ce^{4+} are prevailing as hard acid and can easily form ionic complexes with fluoride ions by electrostatic attraction. To ascertain insight on mechanism, FTIR spectra of fluoride enriched adsorbent were analysed and compared with those of unabsorbed material. Crucial shifting of peak intensity has been observed after fluoride adsorption. Shifting of bands from 3417.13 cm^{-1} to 3243.04 cm^{-1} and from 1633.59 cm^{-1} to

1625.88 cm^{-1} ensure the interaction in between fluoride ions with surface hydroxyl groups of the adsorbent. Partial disappearance of epoxy C-O and alkoxy C-O stretching vibration band peaks in fluoride rich adsorbent confirm chemical interaction of fluoride with these surface active sites of adsorbent. The E_{DR} value obtained at room temperature and in pH 7.0 is 9.13 kJ mol^{-1} envisage that the adsorption process is predominantly ion-exchange in nature. Greater negative value of ΔH^0 and moderate tendency of fluoride desorption and the magnitude of activation energy (22.61 KJ mol^{-1} for the solution pH 7.0) support the said observation.

3.13.3. Proposed Mechanism for βC-CIHFO

The presence of a condensed β-CD moiety along with its unique structural properties instantaneously increase available hydroxyl groups on the surface of CIHFO itself. In as-prepared βC-CIHFO, Fe^{3+} and Ce^{4+} are usually act as hard acid (as per HSAB principle) that attribute strong affinity towards fluoride ions to form ionic complexes either by electrostatic attraction or by formation of hydrogen bonds with the surface active hydroxyl groups largely. On the other hand, a driving force is also elicited on small fluoride ions to move and trapped into the cylindrical complex of β-CD moiety where negatively charged fluoride ions strongly adhere to the hydroxyl groups of β-CD through mostly H-bonding (Scheme-3.4). FTIR spectra of fluoride enriched βC-CIHFO and fluoride free βC-CIHFO were analysed and compared to explore the exact mechanism behind the fluoride adsorption over βC-CIHFO. Significant alteration of peak intensity has been observed after fluoride adsorption occurred. Shifting of bands from 3269.39-3216.89 cm^{-1} to 3302.25 cm^{-1} and from 1608.90-1573.95 cm^{-1} to 1575.76-1559.43cm^{-1}

attributed that ion-exchange might happened as a result of interaction of fluoride ions with surface hydroxyl groups of βC-CIHFO. No such changes in other peak intensity confirmed that hydroxyl groups are mostly involved in adsorption reaction process.The E_{DR} value at room temperature (9.95kJ mol^{-1}) envisaged that the adsorption process is predominantly ion-exchange in nature. Large negative value of ΔH^0, moderate rate of fluoride desorption and the magnitude of activation energy (E_a: 27.16 KJ mol^{-1}) also strongly support the said observation.

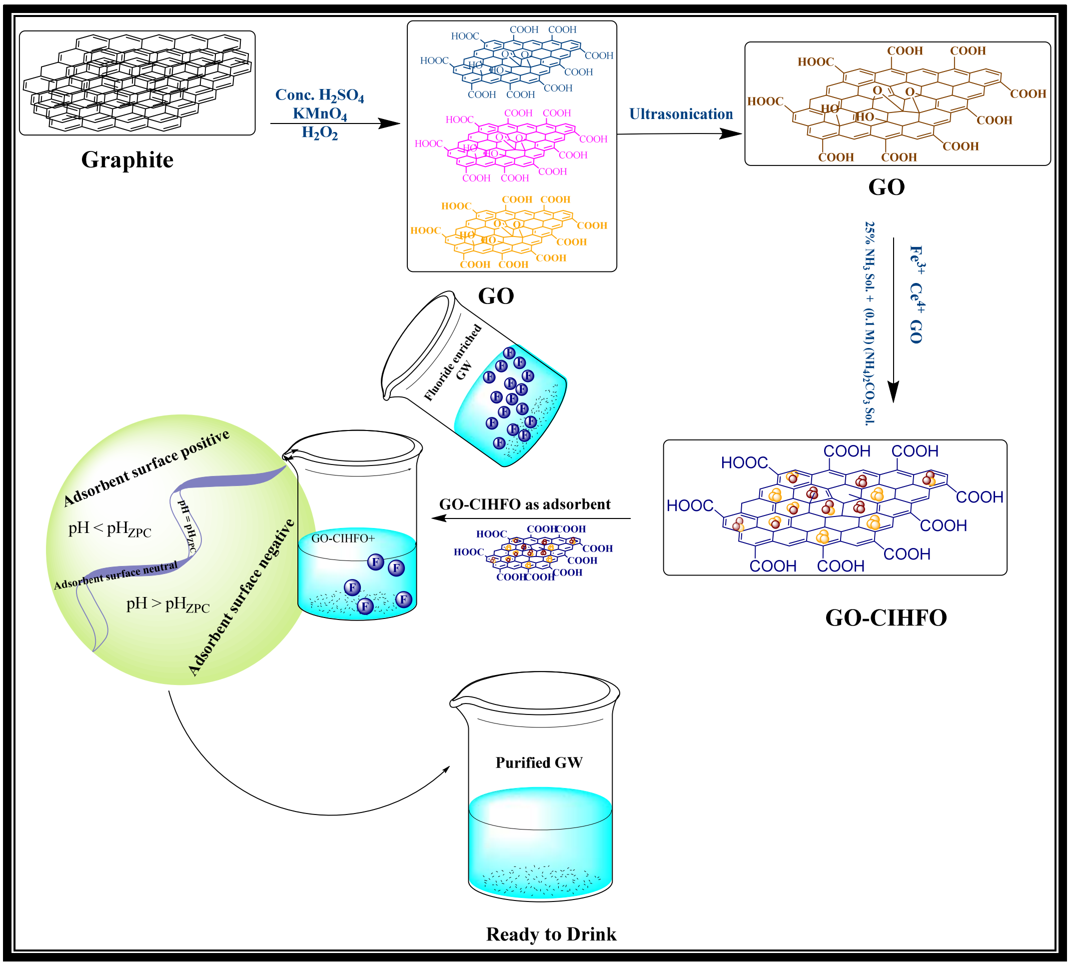

Scheme 3.3: Graphical presentation of proposed reactions mechanism of fluoride adsorption process involved over **GO-CIHFO.**

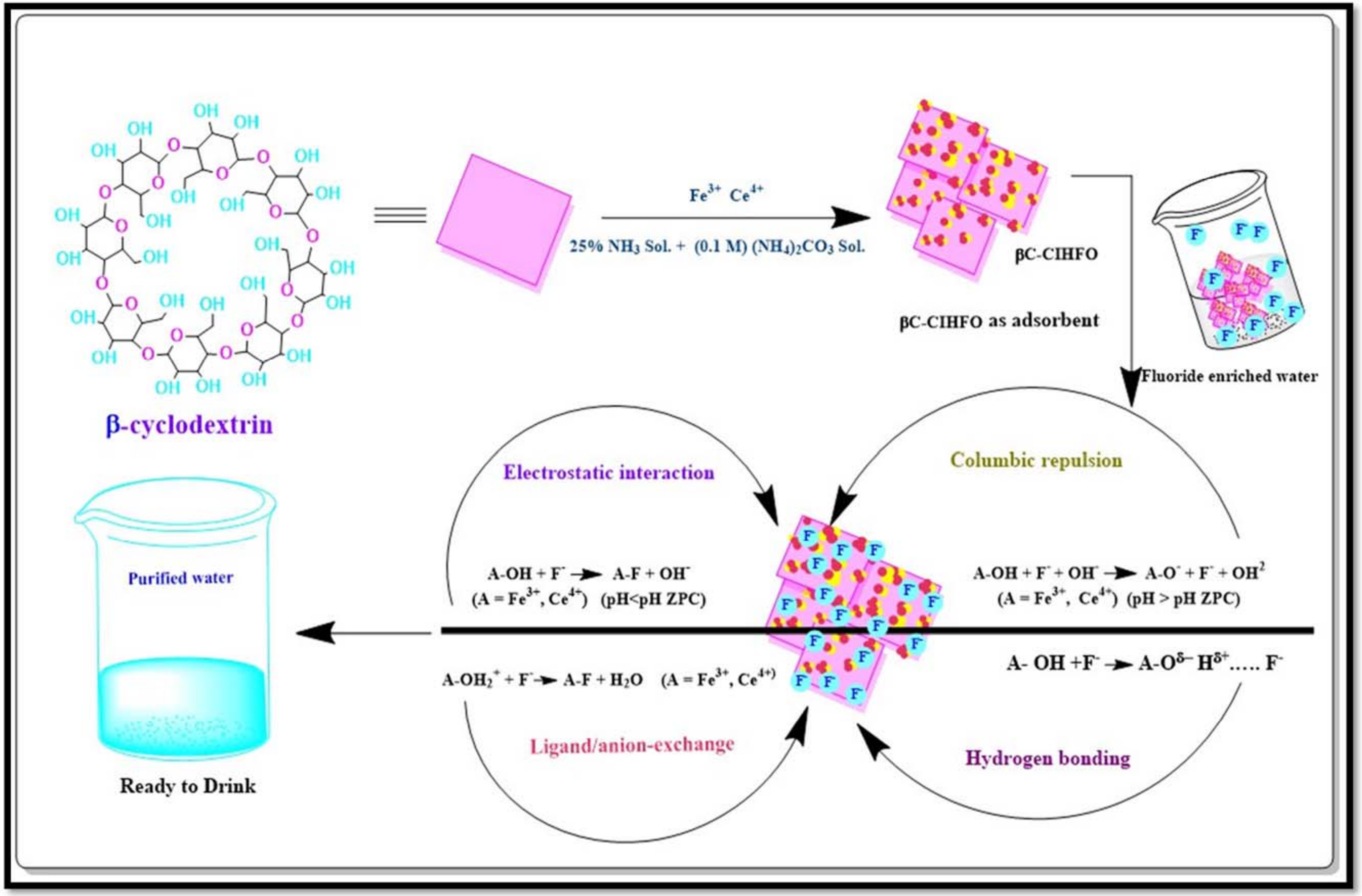

Scheme 3.4: Graphical presentation of proposed reactions mechanism of fluoride adsorption process involved over βC-CIHFO.

Conclusion

- ⇔ Ce(IV)-incorporated hydrous Fe(III) oxide (CIHFO) is microcrystalline and amorphous in nature with high surface area relative to the iron(III) oxide. Microscopic images not only confirmed the presence of micro crystalline particles of nano-dimension, but also irregular in surface morphology.
- ⇔ This thermally stable CIHFO (473K) for fluoride adsorption shows that the surface reaction occurs according to the pseudo-first as well as PSO kinetics with boundary layer (film) diffusion process. Nature of the adsorption reaction is reasonably spontaneous but exothermic in nature. Very low Arrhenius energy of activation inclines to the high affinity of CIHFO for fluoride.
- ⇔ The better adherence of the equilibrium data with the Freundlich isotherm suggests the surface heterogeneity of CIHFO multilayer adsorption and FTIR analysis and other experimental results revealed that fluoride adsorption occurs through ion-exchange which ultimately converted to chemisorption.
- ⇔ Effect of the tested ions on reaction of fluoride adsorption shows no notable adverse influence excepting sulphate. Encouraging results obtain when 2.4 $g.L^{-1}$ of CIHFO employed for high fluoride (9.05 $mg.L^{-1}$) groundwater treatment for field validation.
- ⇔ Surface modification of Ce(IV)-incorporated hydrous Fe(III) oxide (CIHFO) with hydrophilic graphene precursor (GO) successfully achieved by in-situ wet chemical deposition method. The surface area of as-prepared composite (GO-CIHFO) has finely tuned (189.57 $m^2.g^{-1}$) compared to that of pristine CIHFO (140.711 $m^2.g^{-1}$), reported with irregular surface morphology consisting of microcrystals (~2-3 nm) and mesoporous (3.5486 nm).

- ⇔ The GO-CIHFO composite exhibits enhanced fluoride scavenging capacity (80.42 mg $F.g^{-1}$) than GO (35.59 mg $F.g^{-1}$) and pristine CIHFO (32.62 mg $F.g^{-1}$) at pH 7.0. Surface reaction involved in overall fluoride adsorption process from solutions by GO-CIHFO obeying PSO kinetics and multilayer adsorption process, respectively. The film/boundary layer diffusion process is also the rate-determining step.
- ⇔ Nature of the adsorption reaction is reasonably spontaneous and endothermic in thermodynamic sense. The change of Entropy (ΔS°) has been estimated to be lower than 80 kJ mol^{-1} in neutral pH, suggested adsorption process happened mostly by ion-exchange at neutral pH.Calculated E_{DR} value and magnitude of activation energy also favoured these results.
- ⇔ No such adverse effect of interfering ions upon fluoride adsorption occurred. It was observed that 1.2 $g.L^{-1}$ of GO-CIHFO can effectively optimised fluoride level of natural groundwater samples (9.05 $mg.L^{-1}$) to the desirable permissible limit successfully. The adsorbent was successfully regenerated up to 73.77% with alkaline pH range. Reusability of proposed NCs ensures sustainability of proposed adsorbent as fluoride scavenger in future.
- ⇔ Surface modification of Ce(IV)-incorporated hydrous Fe(III) oxide (CIHFO) with β-CD moiety also successfully achieved by in-situ wet chemical deposition method. Both XRD study and microscopic interpretation confirm the microcrystalline nature (~6.022nm) of proposed NCs.
- ⇔ Fluoride adsorption capacity of newly formed adsorbent βC-CIHFO significantly high at neutral pH. Surface reaction appropriately described by the PSO kinetics, whereas, in addition, boundary layer (film) diffusion and external

mass transfer also involved in adsorption reaction. Maximum Langmuir fluoride adsorption capacity of this novel βC-CIHFO is 107.62 mg $F.g^{-1}$ at 323 K and 52.32 mg $F.g^{-1}$ at 303 K in nearly neutral solution pH, respectively that was noticeable higher than individual CIHFO (32.62 $mgF.g^{-1}$) ensuring successful implementation of β-CD as surface modifier over CIHFO.

⇔ Entropy change ($\Delta S°$) is lesser than 80 KJ mol^{-1} in nearly neutral pH range, supports ion-exchange phenomena strongly. Calculated E_{DR} value and magnitude of activation energy also favoured such outputs. Application of $1.8g.L^{-1}$ of βC-CIHFO fruitfully treat high level fluoride (9.05 $mg.L^{-1}$) in groundwater and achieve desirable limit successfully. Regeneration of proposed adsorbent and reusability of it also made the adsorbent useful in this field.